博士論文

Theoretical studies on Doppler laser cooling of an ion beam in a storage ring and an emittance growth mechanism of intense hadron beams

蓄積リングにおけるドップラーレーザー冷却および高強度ハドロンビームのエミッタンス増大機構に関する理論的研究

大　崎　一　哉

広島大学大学院先端物質科学研究科

2016 年 3 月

目次

1. 主論文

Theoretical studies on Doppler laser cooling of an ion beam in a storage ring and an emittance growth mechanism of intense hadron beams
(蓄積リングにおけるドップラーレーザー冷却および高強度ハドロンビームのエミッタンス増大機構に関する理論的研究)
大﨑一哉

2. 公表論文

(1) Free-energy formula for emittance-growth estimation in intense mismatched beams
K. Osaki and H. Okamoto
Progress of Theoretical and Experimental Physics, **2015**, 093G01 (2015). (12 pages)

(2) Parameter optimization for Doppler laser cooling of a low-energy heavy ion beam at the storage ring S-LSR
K. Osaki and H. Okamoto
Progress of Theoretical and Experimental Physics, **2014**, 053G01 (2014). (16 pages)

3. 参考論文

(1) Efficiency Enhancement of Indirect Transverse Laser Cooling with Synchro-Betatron Resonant Coupling by Suppression of Beam Intensity
Hikaru Souda, Masao Nakao, Hiromu Tongu, Kouichi Jimbo, Kazuya Osaki, Hiromi Okamoto,Yousuke Yuri, He Zhengqi, Manfread Grieser and Akira
Japanese Journal of Applied Physics. 52, 030202, (2013). (4 pages)

(2) Beam dynamics studies with non-neutral plasma traps

H. Okamoto, K. Fukushima, H. Higaki, D. Ishikawa, K. Ito, T. Iwai, K. Moriya, T. Okano, K. Osaki, and M. Yamaguchi

Proceedings of 5th International Particle Accelerator Conference, pp. 4052 – 4056 (2014).

(3) Ultralow emittance beam production based on Doppler laser cooling and coupling resonance

A. Noda, M. Nakao, H. Okamoto, K. Osaki, Y. Yuri, H. Souda, H. Tonguu, K. Jimbo, M. Grieser, Z. He, and A. Smirnov

Proceedings of 5th International Particle Accelerator Conference, pp. 28 – 33 (2014).

(4) Parameter optimization for multi-dimensional laser cooling of an ion beam in the storage ring S-LSR

Z. He, J. Wei, K. Osaki, H. Okamoto, A. Noda, M. Nakao, H. Souda, Y. Yuri, and K. Jimbo

Proceedings of Particle Accelerator Conference, pp. 1298 – 1300 (2013).

(5) Latest results of experimental approach to ultra-cold beam at S-LSR

A. Noda, M. Nakao, H. Souda, H. Tongu, H. Okamoto, K. Osaki, Y. Yuri, K. Jimbo, and M. Grieser

Proceedings of International Workshop on Beam Cooling and Related Topics, (COOL 13), pp. 157 – 161 (2013).

(6) Simulation study on transverse laser cooling and crystallization of heavy-ion beams at the cooler storage ring S-LSR

Y. Yuri, K. Osaki, H. Okamoto, Z. He, H. Souda, A. Noda, M. Nakao, H. Tongu, and K. Jimbo

Proceedings of International Workshop on Beam Cooling and Related Topics (COOL 13), pp. 162 – 165 (2013).

(7) Approach to the low temperature state oriented for crystalline beam

A. Noda, M. Nakao, H. Souda, H. Tongu, K. Jimbo, H. Okamoto, K. Osaki, Y. Yuri, I. N. Meshkov, A. V. Smirnov, M. Grieser, K. Noda, T. Shirai, and Z. He

Proceedings of XXIII Russian Particle Accelerator Conference, (RuPAC2012), pp. 48 – 52 (2012).

(8) Challenge for more efficient transverse laser cooling for beam crystallization

A. Noda, M. Nakao, H. Souda, H. Tongu, K. Ito, H. Okamoto, K. Osaki, Y. Yuri, K.

Jimbo, M. Grieser, and Z. He

Proceedings of 3rd International Particle Accelerator Conference, pp. 394 – 396 (2012).

(9) Controlled beam scraping oriented for efficient indirect transverse laser cooling

A. Noda, M. Nakao, H. Souda, H. Tongu, K. Jimbo, H. Okamoto, K. Osaki, Y. Yuri, M. Grieser, and Z. He

Proceedings of 9th Meeting of Particle Accelerator Society of Japan, pp. 72 – 74 (2012).

(10) Measurement of transverse laser cooling effect using scrapers

H. Souda, M. Nakao, H. Tongu, A. Noda, K. Jimbo, K. Osaki, H. Okamoto, Y. Yuri, M. Grieser, and Z. He

Proceedings of 9th Meeting of Particle Accelerator Society of Japan, pp. 388 – 390 (2012).

(11) Present status of ion accumulation and cooler ring S-LSR

A. Noda, H. Souda, H. Tongu, M. Nakao, Y. Nasu, K. Jimbo, H. Okamoto, K. Osaki, K. Noda, S. Shibuya, T. Fujimoto, S. Iwata, M. Grieser, and H. Zhengqi

Proceedings of 8th Meeting of Particle Accelerator Society of Japan, pp. 261 – 263 (2011).

主論文

Contents

Outline

The first artificial acceleration of charged particles to a high kinetic energy was performed nearly a century ago [1]. Since then, a variety of machines that enable one to accelerate electrons, protons, heavy ions, and even anti-particles, have been invented for diverse experimental purposes [2]. We now have linear accelerators of various kinds such as DTL (Drift Tube Linac), DAW (Disk-And-Washer structure), RFQ (Radio-Frequency Quadrupole linac), etc., and circular accelerators such as cyclotrons [3], synchrotrons [4], storage-ring colliders, etc. [5]. In the early 20th century, particle accelerators were mostly employed for fundamental physics purposes. The usefulness of charged-particle beams for other fields were, however, realized soon and, as a result, many accelerators began to be constructed all over world. For instance, both hadron and lepton machines have widely been used for radiation therapy [6,7]. The so-called *photon factories* are also available in many countries now. To explore high-energy frontier, extremely large colliders have been built in Europe, the United States, and Asia.

The physical property of a charged-particle beam is characterized by “energy”, “intensity”, and “emittance”. Among them, the emittance is particularly important in almost all kinds of applications. This concept is defined as the volume occupied by the beam in six-dimensional phase space. To put it briefly, the emittance corresponds to the beam temperature. A beam of lower emittance is certainly more preferable because we can focus it thinner or generate a nearly parallel beam. The emittance is, however, an approximate invariant in regular accelerators that can be regarded as a sort of conservative dynamical system. Main components of an accelerator, i.e. multipole magnets, radio-frequency cavities, etc. yield conservative forces, which means that the phase-space volume of a beam is unchanged due to the Liouville’s theorem [8]. We thus need to introduce some dissipative interaction in the machine to control the emittance artificially.

The process of improving the beam quality or, in other words, reducing the emittance is called “cooling” because the temperature becomes lower as the beam is compressed in phase space. There are only few cooling methods technically well-established and applicable to hadron beams; namely, electron cooling [9],

stochastic cooling [10], and laser cooling [11,12]. Electron cooling and stochastic cooling are very popular in the community. On the other hand, Doppler laser cooling has been employed only at three laboratories so far, despite the fact that this relatively new cooling technique can produce an ultracold ion beam in principle. The TSR group of Max Planck Institute in Germany carried out the first proof-of-principle experiment [13], immediately followed by another attempt at the ASTRID ring in Denmark [14]. These two teams succeeded in cooling the longitudinal beam motion, but unfortunately, it turned out that efficient cooling of the transverse betatron motion is very difficult to achieve in practice.

More than 10 years after the European attempts, a Japanese group constructed a compact cooler storage ring equipped with a Doppler cooling system [15,16]. The ring is named "S-LSR" (Small Laser-equipped Storage Ring). The lattice design of S-LSR has been designed carefully to minimize possible beam heating due to collective resonance. Most importantly, the so-called "resonant coupling method" [17,18] can be applied in this ring for indirect transverse laser cooling. The ultimate goal of this experiment is to crystallize an ion beam by reducing the beam temperature near the absolute zero. The cooling system, however, has some technical limitations. Careful optimization of the lattice and laser parameters is thus crucial for the best cooling performance. For this purpose, I carried out a number of systematic multi-particle simulations using the molecular dynamics (MD) code "CRYSTAL" developed at Hiroshima University [19]. As demonstrated below, a one-dimensional quasi-crystalline state could be reached in S-LSR only by adjusting several parameters to optimum values [20].

There exist various sources of instabilities that seriously deteriorate the beam quality. As is well-known, the periodic nature of alternating gradient beam focusing gives rise to resonance under specific conditions. Even if the machine operating point is chosen sufficiently away from resonance lines, we may still need to care about wake fields, residual gases, electron clouds, colliding beams, etc. [21] In a high-intensity hadron accelerator, serious beam heating can occur spontaneously even without all these external origins of instability. The strong Coulomb potential of an intense beam can be a source of root-mean-squared (rms) emittance growth when the beam is deviated from the perfect stationary state. Since it is practically impossible to provide an ideal matched beam at injection, such self-field-induced instability is an important issue that has to be

studied in detail. The latter part of the present thesis is devoted to this issue.

In what follows, I start from a brief overview of the standard beam orbit theory in Chapter 1 for later convenience. I then go to systematic MD simulations of laser cooling in Chapter 2 and search for the best set of fundamental parameters assuming the experimental condition of S-LSR. It is shown that a unique ultracold state of beam could be established by means of the resonant coupling method with optimum laser-cooling parameters. As mentioned above, Chapter 3 is devoted to the derivation of simple analytic formulas that allow us to make a quick estimate of rms emittance growth in an initially mismatched beam. The two-dimensional *free-energy model* developed by Martin Reiser [22] is generalized to treat an ellipsoidal bunches of arbitrary aspect ratio. Theoretical predictions are compared with Particle-In-Cell (PIC) simulations.

Acknowledgements

I would like to express my sincere gratitude to my supervisor Prof. Hiromi Okamoto for his continuous support and guidance during the course of the present study. I am also indebted to Prof. Steve Lund of Michigan State University for valuable discussion on beam physics issues.

1. Beam orbit theory

1.1 Hamiltonian formalism for beam dynamics

The basic structures of particle accelerators can be classified roughly to two types; namely, *linear* and *circular* accelerators. In both types, electromagnetic fields are used to focus, guide, and accelerate a group of charged particles in the machines. Considering that the beam motion is usually relativistic, the starting point of single-particle dynamics is the classical Hamiltonian

$$H = q\phi + \sqrt{(\boldsymbol{P} - q\boldsymbol{A})^2 + m^2c^2}, \tag{1.1}$$

where q and m are the charge state and rest mass of the particle, ϕ and $\boldsymbol{A}$ are the scalar and vector potentials of the electromagnetic fields generated by multipole magnats, radio-frequency (rf) cavities, and other components in the machine, $\boldsymbol{P}$ is the canonical momentum, and c is the speed of light in vacuum.

In general, we take the path length *s* along the beam orbit, instead of time *t*, as the independent variable because the external potentials ϕ and $\boldsymbol{A}$ cannot be well defined in time; in other words, electromagnetic components that create ϕ and $\boldsymbol{A}$ are *spatially* fixed. It is thus much more convenient to redefine the Hamiltonian (1.1) in a new coordinate system as illustrated in Fig. 1.1. This system is referred to as "Frenet-Serret coordinates". The Hamiltonian canonically transformed to this coordinate system can be written as

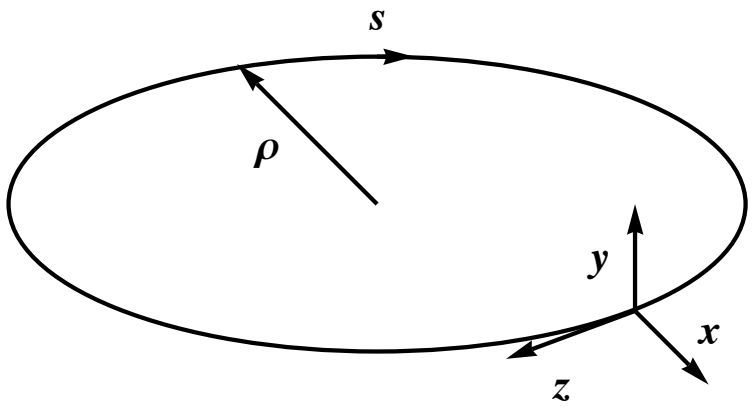

Fig. 1.1 The Frenet-Serret system in circular accelerators

$$H(x, P_x, y, P_y, t, -E; s)$$
$$= -\left(1 + \frac{x}{\rho(s)}\right)\sqrt{P^2 - (P_x - qA_x)^2 - \left(P_y - qA_y\right)^2} \quad (1.2)$$
$$- qA_s\left(1 + \frac{x}{\rho(s)}\right).$$

where $\rho(s)$ is the local curvature of the beam orbit, and P is the total kinetic momentum defined as $P = \sqrt{(E - q\phi)^2/c^2 - m^2c^2}$. Note that the longitudinal canonical variables are no longer the spatial coordinate z and the conjugate momentum but changed to (t, -E) where E represents the total energy of the particle. Assuming $|P_x/P| \ll 1$ and $|P_y/P| \ll 1$, we can expand the square root in Eq. (1.2) and keep only low-order terms to obtain

$$H \approx -\left(1 + \frac{x}{\rho(s)}\right)\left[qA_s + P - \frac{(P_x - qA_x)^2 + \left(P_y - qA_y\right)^2}{2P}\right]. \quad (1.3)$$

Ideally, only the longitudinal component of the vector potential is necessary to describe the effects of acceleration by rf cavities and transverse Lorentz forces from multipole magnets; namely, $A_x = A_y = 0$ In addition if we use the following relation between momentum deviation $\delta P = P - P_0$ and $\delta E = E - E_0$,

$$\delta P \approx \frac{\delta E}{\beta_0 c} - \frac{1}{2P_0}\left(\frac{\delta E}{\beta_0\gamma_0 c}\right)^2. \quad (1.4)$$

β_0 and γ_0 are Lorentz factor of a reference particle, P_0 is the design momentum, and E_0 is the design energy. The following generating function $G_1(t, -\delta E)$ gives us a canonical transformation from $(t, -E)$ to $(\tau, -\delta E)$.

$$G_1(t, -\delta E) = -(E_0 + \delta E)t \quad (1.5)$$

As a result Hamiltonian can be rewritten as

$$H(x, P_x, y, P_x, \tau, -\delta E; s) \quad (1.6)$$
$$\approx -\left(1 + \frac{x}{\rho(s)}\right)\left[qA_s + P_0 + \frac{\delta E}{\beta_0 c} - \frac{1}{2P_0}\left(\frac{\delta E}{\beta_0\gamma_0 c}\right)^2\right.$$
$$\left. - \frac{{P_x}^2 + {P_y}^2}{2P}\right].$$

Another canonical transformation to verify the variables from $(\tau, -\delta E)$ to (z, P_z) is carried out with Eq. (1.7).

$$G_2(\tau, P_z) = \beta_0\gamma_0 c \cdot (\tau - \tau_0)P_z. \tag{1.7}$$

z and p_z are defined as $z = \beta_0\gamma_0 c(\tau - \tau_0)$ and $p_z = -\delta E/\beta_0\gamma_0 c$ respectively, τ_0 is the reference time of a design particle injected to an accelerator.

$$\begin{aligned} H(x, p_x, y, p_y, z, p_z; s) \\ &\approx \left(1 + \frac{x}{\rho(s)}\right)\gamma_0 p_z \\ &+ \left(1 + \frac{x}{\rho(s)}\right)\left(\frac{{p_x}^2 + {p_y}^2 + {p_z}^2}{2} - 1 - \frac{qA_s}{P_0}\right). \end{aligned} \tag{1.8}$$

The transformation and the scaling of canonical variables shown in Eq. (1.9) is the well-known analytical technic of the beam-dynamics theory.

$$H \to H/P_0, p_x \to P_x/P_0, p_y \to P_y/P_0, p_z \to P_z/P_0. \tag{1.9}$$

Quadrupole magnets, drift space, Bending magnets, and rf cavities of TM_{010} mode is the basic components of circler accelerators. The vector potentials of them are shown in Eq. (1.10).

$$\begin{aligned} A_s = -\frac{P_o}{q}\left(1 + \frac{x}{\rho(s)} - \frac{K_1(s)}{2}x^2 + \frac{K_1(s)}{2}y^2\right) \\ &+ \frac{E_0}{h_{rf}\omega_0}\left[\cos\left(\frac{h_{rf}\omega_0}{\beta_0\gamma_0 c}z + \varphi_0\right) - \cos(\varphi_0)\right. \\ &+ \left.\left(\frac{h_{rf}\omega_0}{\beta_0\gamma_0 c}z + \varphi_0\right)\sin(\varphi_0)\right]\delta_p(s - s_{rf}). \end{aligned} \tag{1.10}$$

Substituting Eq. (1.10) into Eq. (1.8), then the Hamiltonian of the basic storage ring is written by

$$\begin{aligned} H \approx \left(1 + \frac{x}{\rho(s)}\right)\gamma_0 p_z + \frac{1}{2}\left({p_x}^2 + {p_y}^2 + {p_z}^2\right) + \frac{1}{2}\left(K_x(s)x^2 + K_y(s)y^2\right) \\ &+ \frac{qE_0}{P_0 h_{rf}\omega_0}\left[\cos\left(\frac{h_{rf}\omega_0}{\beta_0\gamma_0 c}z + \varphi_0\right) - \cos(\varphi_0)\right. \\ &+ \left.\left(\frac{h_{rf}\omega_0}{\beta_0\gamma_0 c}z + \varphi_0\right)\sin(\varphi_0)\right]\delta_p(s - s_{rf}), \end{aligned} \tag{1.11}$$

where $K_x(s) = 1/\rho(s)^2 - K_1(s)/2$ and $K_y(s) = K_1(s)/2$. $K_1(s)$ is the gradient of the magnetic field expressed as $K_1(s) = \frac{q}{p_0}\frac{\partial B_y^{ext}}{\partial x}$, E_0 is the electric field of a rf cavity, h_{rf} is the harmonic number of a storage ring, φ_0 is a rf phase of a design particle, and

ω_0 is the circulating frequency of a beam.

1.1.1 Transverse dynamics

Considering the orbit dynamics of a charged particle in accelerators, we usually separate a motion of the transverse and longitudinal directions for the convenience of the theoretical treatment. Let us explain the transverse dynamics at first. The basic linear theory of the transverse-beam dynamics was constructed by Courant and Snyder [23]. From the Hamiltonian of a storage ring shown in Eq. (1.8), we obtain the following parts as a Hamiltonian of the transverse degree of freedom.

$$H = \frac{1}{2}\left({p_x}^2 + {p_y}^2\right) + \frac{1}{2}\left(K_x(s)x^2 + K_y(s)y^2\right). \tag{1.12}$$

The equations of motion are given automatically from Eq. (1.12).

$$\frac{d^2x}{ds^2} = -K_x(s)x. \tag{1.13.a}$$

$$\frac{d^2y}{ds^2} = -K_y(s)y. \tag{1.13.b}$$

Eqs. (1.13) are known as Hill's equation, $K_x(s)$ and $K_y(s)$ represent focusing force in an accelerator. When we suppose a circular accelerator, $K_x(s)$ and $K_y(s)$ are periodic functions given from the lattice so they can expressed algebraically as $K_x(s) = K_x(s + L)$ and $K_y(s) = K_y(s + L)$. L is the lattice length. Eqs. (1.13) have same character mathematically, therefore we only focus on the horizontal direction. According to Flouqet's theory a general solution of Hill's equation is known as follows.

$$x(s) = \sqrt{J_x\beta_x(s)}\exp(i\varphi(s) + \varphi_o). \tag{1.14}$$

If we consider only a real part of Eq. (1.14), the single-particle orbit of the horizontal direction is written as

$$x(s) = \sqrt{J_x\beta_x(s)}\cos\left(\varphi(s) + \varphi_o\right). \tag{1.15}$$

$$\frac{dx(s)}{ds} = \cos(\varphi(s) + \varphi_o)\frac{d}{ds}\left(\sqrt{J_x\beta_x(s)}\right) - \frac{d\varphi(s)}{ds}\sqrt{J_x\beta_x(s)}\sin(\varphi(s) + \varphi_o). \tag{1.16}$$

Equation. (1.15) is so-called betatron oscillation. $\beta_x(s)$ is betatron function of the twiss parameters and it is the periodic function of the lattice length ($\beta_x(s) = \beta_x(s+L)$). J_x is the Courant-Snyder invariant and it roughly means the emittance referred in outline. An invariant is an essential element in Hamiltonian formalism for the better understanding of the dynamics. By means of Eq. (1.15) and (1.16) (the differential of Eq. (1.15)), Courant-Snyder invariant is given by

$$\gamma(s)x^2(s) + 2\alpha(s)x(s)\frac{dx(s)}{ds} + \beta(s)\left(\frac{dx(s)}{ds}\right)^2 = J_x. \tag{1.17}$$

$\alpha(s)$, $\beta(s)$, and $\gamma(s)$ are known as twiss parameters defined by

$$\alpha_x(s) = -\frac{1}{2}\frac{d\beta_x(s)}{ds}, \tag{1.18.a}$$

$$\gamma_x(s) = \frac{1}{4\beta_x(s)}\left(\frac{d\beta_x(s)}{ds}\right)^2 + \frac{1}{\beta_x(s)}. \tag{1.18.b}$$

The equation of $\beta(s)$ can be derived by Eq. (1.13.a) and Eq. (1.15) as follows. We often solve Eq. (1.19) numerically and get the solution of the beta function entire the storage ring.

$$\frac{d^2\sqrt{\beta_x(s)}}{ds^2} + K_x(s)\sqrt{\beta_x(s)} - \frac{1}{\beta_x(s)^{3/2}} = 0, \tag{1.19}$$

Integrating Eq. (1.20) throughout a storage ring means a betatron tune of a particle.

$$\frac{d\varphi(s)}{ds} = \frac{1}{\beta_x(s)}. \tag{1.20}$$

$$\nu_x = \frac{1}{2\pi}\int_0^L \frac{1}{\beta_x(s)}ds. \tag{1.21}$$

Needless to say, the same discussion can be done for the vertical degree of freedom. As we mentioned in the previous section, the beam-transport system is constructed by the three-different parts, drift space, quadrupole magnets, and bending magnets. The transfer-matrix theory of each beam-transport system is shown in the following section.

・**Drift space**

A drift space is the section of no electromagnetic fields in the beam-transport system, so the beam-focusing function $K_x(s)$ and $K_y(s)$ are zero. As a result the Hamiltonian of this section is written as

$$H = \frac{1}{2}\left({p_x}^2 + {p_y}^2\right). \tag{1.22}$$

In general the transfer matrix is expressed as $\boldsymbol{X}_{\mathrm{end}} = M_{\mathrm{transfer}}\boldsymbol{X}_{\mathrm{start}}$, where $\boldsymbol{X} = (x, p_x)$ and M_{transfer} is called as a transfer matrix. In the case of a drift space, the particle motion in matrix formulation is written by a following formula.

$$\begin{pmatrix} x \\ p_x \end{pmatrix}_{\mathrm{end}} = \begin{pmatrix} 1 & L_d \\ 0 & 1 \end{pmatrix}\begin{pmatrix} x \\ p_x \end{pmatrix}_{\mathrm{start}}, \tag{1.23}$$

where L_d is the length of a drift space. We can apply the same procedure to the vertical direction.

・**Bending magnet**

A bending magnet is the component to circulate the beam, so there is only a dipole magnetic field. The vector potential of this section is written as $A_s = -\frac{p_0}{q}\frac{x}{\rho_m}$. As a result the Hamiltonian of this section is written as

$$H = \frac{1}{2}\left({p_x}^2 + {p_y}^2\right) + \frac{1}{{\rho_m}^2}x^2, \tag{1.24}$$

where ρ_m is the curvature radius at bending magnets. Therefore, the transfer matrix of a bending magnet is written by a following formula.

$$\begin{pmatrix} x \\ p_x \end{pmatrix}_{\mathrm{end}} = \begin{pmatrix} \cos\left(\frac{1}{\rho_m}L_b\right) & \rho_m \sin\left(\frac{1}{\rho_m}L_b\right) \\ -\frac{1}{\rho_m}\sin\left(\frac{1}{\rho_m}L_b\right) & \cos\left(\frac{1}{\rho_m}L_b\right) \end{pmatrix}\begin{pmatrix} x \\ p_x \end{pmatrix}_{\mathrm{start}}, \tag{1.25}$$

where L_b is the length of a bending magnet. Ideally the vertical direction will not be influenced in this section, so the transfer matrix of the vertical direction is same as the drift space one.

Next, we will mention about the dispersion effect generated by the bending magnets. The strength of a magnetic field in a bending magnet is defined as

$$B_0 = P_0/q\rho_m. \tag{1.26}$$

The designed particle with the momentum P_0 keeps staying at the origin of the horizontal direction, however a curvature of a particle with the momentum deviation δP is changed at the bending magnet. As a result the horizontal orbit deviates from a design orbit due to a bending-magnet section. The orbit deviation can be expressed as

$$x(s) = D_x(s)\frac{\delta P}{P}. \tag{1.27}$$

$D_x(s)$ is know as a dispersion function which can be derived from the following equation of motion.

$$\frac{d^2x}{ds^2} + K_x(s)x = \frac{\delta P}{P}\frac{1}{\rho(s)}. \tag{1.28}$$

Substituting Eq. (1.31) to Eq. (1.32), the equation of a dispersion function is given as

$$\frac{d^2D_x(s)}{ds^2} + K_x(s)D_x(s) = \frac{1}{\rho(s)}. \tag{1.29}$$

By means of Eqs. (1.23) and (1.31), an orbit of the horizontal direction is written as

$$x(s) = \sqrt{\varepsilon_x\beta_x(s)}\cos(\varphi(s) + \varphi_o) + D_x(s)\frac{\delta P}{P}. \tag{1.30}$$

- **Quadrupole magnet**

In the quadrupole-magnet section, the vector potential is written by $A_s = -\frac{p_o}{2q}(K_1x^2 - K_1y^2)$ and a Hamiltonian is given by

$$H = \frac{1}{2}\left({p_x}^2 + {p_y}^2\right) + K_1x^2 - K_1y^2. \tag{1.31}$$

When K_1 has positive value, the transfer matrix is expressed as

$$\begin{pmatrix} x \\ p_x \end{pmatrix}_{\text{end}} = \begin{pmatrix} \cos\left(\sqrt{K_1}L_q\right) & \frac{1}{\sqrt{K_1}}\sin\left(\sqrt{K_1}L_q\right) \\ -\sqrt{K_1}\sin\left(\sqrt{K_1}L_q\right) & \cos\left(\sqrt{K_1}L_q\right) \end{pmatrix}\begin{pmatrix} x \\ p_x \end{pmatrix}_{\text{start}}. \tag{1.32}$$

On the other hand, when K_1 is negative, the transfer matrix is expressed as

$$\begin{pmatrix} x \\ p_x \end{pmatrix}_{\text{end}} = \begin{pmatrix} \cosh\left(\sqrt{K_1}L_q\right) & \frac{1}{\sqrt{K_1}}\sinh\left(\sqrt{K_1}L_q\right) \\ -\sqrt{K_1}\sinh\left(\sqrt{K_1}L_q\right) & \cosh\left(\sqrt{K_1}L_q\right) \end{pmatrix}\begin{pmatrix} x \\ p_x \end{pmatrix}_{\text{start}}. \tag{1.33}$$

where L_q is a length of a quadrupole magnet in the longitudinal direction. Finally the transfer matrix of an entire storage ring is expressed as Eq. (1.34). α_x , β_x, and γ_x are twiss parameters shown in Eq. (1.18)

$$M_{\text{oneturn}} = \begin{pmatrix} \cos(2\pi\nu_x) + \alpha_x \sin(2\pi\nu_x) & \beta_x \sin(2\pi\nu_x) \\ -\gamma_x \sin(2\pi\nu_x) & \cos(2\pi\nu_x) - \alpha_x \sin(2\pi\nu_x) \end{pmatrix}. \tag{1.34}$$

1.1.2 Longitudinal dynamics

For the purpose of the beam acceleration and the beam bunching, a rf cavity of TM_{010} mode is the most convenient component. According to Eq. (1.11), the Hamiltonian of the longitudinal direction obeys

$$\begin{aligned} H \approx \frac{1}{2}{p_z}^2 + \frac{qE_0}{P_0 h_{rf}\omega_0}\Bigg[\cos\left(h_{rf}\frac{z}{\rho_0} + \varphi_0\right) - \cos(\varphi_0) \\ + \left(h_{rf}\frac{z}{\rho_0} + \varphi_0\right)\sin(\varphi_0)\Bigg]\delta_p(s - s_{rf}). \end{aligned} \tag{1.35}$$

The equation of motion in the longitudinal direction is automatically obtained as

$$\begin{aligned} \frac{d^2 z}{ds^2} &\approx -\frac{qE_0}{m(\gamma_0\beta_0 c)^2}\cos(\varphi_0)\sin\left(h_{rf}\frac{z}{\rho_0}\right)\delta_p(s - s_{rf}) \\ &\approx -\frac{q h_{rf} E_0 \cos(\varphi_0)}{m\rho_0(\gamma_0\beta_0 c)^2} z\delta_p(s - s_{rf}). \end{aligned} \tag{1.36}$$

The thin-lens approximation of a rf cavity is supposed in Eq. (1.35). When we set the rf phase of a design particle to $\varphi_0 = 0$, the beam acceleration will not be occurred. The accurate-energy gain of a design particle per passage can be calculated by the integration through the entire rf cavity.

$$\Delta U = qE_0\beta_0 c\int_{-d_{gap}/2\beta_0 c}^{d_{gap}/2\beta_0 c}\cos(h_{rf}\omega_0 t + \varphi_0)\,dt = qV_0\cos(\varphi_0)\,\mathcal{Q}. \tag{1.37}$$

where d_{gap} is the gap length, $V_0 = d_{gap}E_0$ is the maximum voltage, $\mathcal{Q}$ is the transit-time factor defined by

$$\mathcal{Q} = \frac{\sin(h_{rf}d_{gap}/2\rho_0)}{h_{rf}d_{gap}/2\rho_0} \tag{1.38}$$

It represents the effective-acceleration voltage for a design particle. $\mathcal{Q}$ is always smaller than unity and the more $\mathcal{Q}$ large, the more charged particles obtain the large acceleration. When $qV_0\cos(\varphi_0)$ has a positive value, a particle oscillates around

$z = 0$. This is known as a synchrotron motion. Then, we should mention about the two important parameters related to the longitudinal motion. First one is the momentum-compaction factor defined as

$$\zeta = \frac{1}{2\pi\,\rho_0}\int_0^{2\pi\,\rho_0}\frac{D_x(s)}{\rho(s)}\,ds. \tag{1.40}$$

The closed orbit of the entire ring is longer when the momentum deviation exists. The relation between a momentum deviation and the closed-orbit length can be given as

$$\frac{\delta 2\pi\,\rho_0}{2\pi\,\rho_0} = \zeta\frac{\delta P}{P}, \tag{1.39}$$

where ρ_0 is the average curveture of a ring.

The second one is the phase-slip factor defined by $\left(\zeta - \frac{1}{\gamma_0^2}\right)$. In the case of a designed particle, the circulation time of a storage ring is given by $\mathcal{T} = 2\pi\,\rho_0/\beta_0 c$, the particle with the momentum deviation δP takes extra time $\delta\mathcal{T}$ to circulate the ring.

$$\frac{\delta\mathcal{T}}{\mathcal{T}} = \frac{\delta 2\pi\,\rho_0}{2\pi\,\rho_0} - \frac{\delta\beta_0 c}{\beta_0 c} = \frac{\delta 2\pi\,\rho_0}{2\pi\,\rho_0} - \frac{1}{\gamma_0^2}\frac{\delta P}{P} = \varsigma\frac{\delta P}{P}. \tag{1.41}$$

If a phase slip factor is zero, a lap time of all particles have same value. γ_T defined by Eq. (1.42) is called transition energy.

$$\gamma_0 = \frac{1}{\sqrt{\varsigma}} = \gamma_T. \tag{1.42}$$

1.1.3 Resonance instabilities

There are many potential sources of the beam instability that seriously deteriorate the quality of a charged-particle beam. Even if the operating point of an accelerator is properly chosen on the tune diagram to avoid intrinsic resonance lines, the beam may still be unstable due to various extra factors including magnetic error fields, coupling-impedance sources, radio-frequency (rf) noises, etc. The beam loss of high-energy accelerators, due to these instabilities, will generate the radioactive substance. In order to avoid this worst situation, the better understanding of resonance instabilities is essential.

Sum resonance and difference resonance are famous beam instabilities [21, 24 – 27]. When a coupling potential $K(s)x^{l_x}y^{l_y}$ exists in an accelerator, the Hamiltonian of the transverse direction can be obtained as

$$H = \frac{1}{2}\left(p_x{}^2 + p_y{}^2\right) + \frac{1}{2}\left(K_x(s)x^2 + K_x(s)y^2\right) + K(s)x^{l_x}y^{l_y}. \tag{1.43}$$

l_x and l_y are natural numbers. Usually $K(s)$ is much smaller than $K_x(s)$ and $K_y(s)$. The canonical transformation, with the generating functions Eqs. (1.44) and (1.46), are convenient for the analytic calculation of the nonlinear-beam dynamics.

$$F_1(x, y, \psi_x, \psi_y) = -\frac{x^2}{2\beta_x(s)}\left(\tan\psi_x - \frac{\beta_x'(s)}{2}\right) - \frac{y^2}{2\beta_y(s)}\left(\tan\psi_y - \frac{\beta_y'(s)}{2}\right), \tag{1.44}$$

$$\begin{aligned}\widehat{H} = \frac{J_x}{\beta_x(s)} + \frac{J_y}{\beta_y(s)} + \frac{K(s)}{2^{\frac{l_x+l_y}{2}}}\beta_x{}^{\frac{l_x}{2}}(s)\beta_y{}^{\frac{l_y}{2}}(s)J_x{}^{\frac{l_x}{2}}J_y{}^{\frac{l_y}{2}}(\cos\left(l_x\psi_x + l_y\psi_y\right) \\ + \cos\left(l_x\psi_x - l_y\psi_y\right) + \cdots).\end{aligned} \tag{1.45}$$

$$F_2(\psi_x, \psi_y, \overline{J_x}, \overline{J_y}) = \left(\psi_x - \int_0^s \frac{ds}{\beta_x(s)} + \nu_x\frac{s}{\rho_0}\right)\overline{J_x} + \left(\psi_y - \int_0^s \frac{ds}{\beta_y(s)} + \nu_y\frac{s}{\rho_0}\right)\overline{J_y}. \tag{1.46}$$

$$\begin{aligned}\overline{H} = \frac{\nu_x}{\rho_0}\overline{J_x} + \frac{\nu_y}{\rho_0}\overline{J_y} + \overline{J_x}^{\frac{l_x}{2}}\overline{J_y}^{\frac{l_y}{2}}(G_{l_x,l_y,l_s}\cos\left(l_x\overline{\psi_x} + l_y\overline{\psi_y} - l_s\frac{s}{\rho_0} + \sigma_{l_s}\right) \\ + G_{l_x,l_y,l_d}\cos\left(l_x\overline{\psi_x} - l_y\overline{\psi_y} - l_d\frac{s}{\rho_0} + \sigma_{l_d}\right) + \cdots).\end{aligned} \tag{1.47}$$

The Fourier amplitudes G_{l_x,l_y,l_s}, G_{l_x,l_y,l_d} and the phase σ_{l_s}, σ_{l_d} are expressed respectively as

$$G_{l_x,l_y,l_s}e^{i\sigma_{l_s}} = \oint \frac{K(s)}{2^{\frac{l_x+l_y}{2}}}\beta_x{}^{\frac{l_x}{2}}(s)\beta_y{}^{\frac{l_y}{2}}(s)\, e^{i\left[l_x\psi_x + l_y\psi_y - (l_x\nu_x + l_y\nu_y - l_s)\frac{s}{\rho_0}\right]}ds, \tag{1.48.a}$$

$$G_{l_x,l_y,l_d}e^{i\sigma_{l_d}} = \oint \frac{K(s)}{2^{\frac{l_x+l_y}{2}}}\beta_x{}^{\frac{l_x}{2}}(s)\beta_y{}^{\frac{l_y}{2}}(s)\, e^{i\left[m\psi_x - n\psi_y - (l_x\nu_x - l_y\nu_y - l_d)\frac{s}{\rho_0}\right]}ds. \tag{1.48.b}$$

We will explain the sum resonance at first. Under the condition of $l_x\nu_x + l_y\nu_x = l_s$, the Hamiltonian can be approximated as

$$\overline{H} = \frac{\nu_x}{\rho_0}\overline{J_x} + \frac{\nu_y}{\rho_0}\overline{J_y} + \overline{J_x}^{\frac{l_x}{2}}\overline{J_y}^{\frac{l_y}{2}}G_{l_x,l_y,l_s}\cos\left(l_x\overline{\psi_x} + l_y\overline{\psi_y} - l_s\frac{s}{\rho_0} + \sigma_{l_s}\right). \tag{1.49}$$

From the Eq. (1.47), we obtain the following equation.

$$l_y \frac{\partial \overline{J_x}}{\partial s} - l_x \frac{\partial \overline{J_y}}{\partial s} = 0. \tag{1.50}$$

Finally we lead to the following formula of sum resonance.

$$l_y J_x - l_x J_y = constant. \tag{1.51}$$

When tunes set to the condition $l_x \nu_x - l_y \nu_x = l_s$, the relation of the difference resonance is given by the similar procedure as follows.

$$l_y J_x + l_x J_y = constant. \tag{1.52}$$

Under the sum-resonance condition, the beam emittances of the two degrees of freedom keep increasing. Therefore we must pay attention to the sum resonance condition for the accelerator operation.

1.1.4 Definition of beam temperatures

In general the kinetic energy is used for the definition of a temperature. Accordingly we define beam temperatures as follows.

$$k_B T_x = \frac{\langle {P_x}^2 \rangle}{2m}, \tag{1.53.a}$$

$$k_B T_y = \frac{\langle {P_y}^2 \rangle}{2m}, \tag{1.53.b}$$

$$k_B T_z = \frac{\langle {P_z}^2 \rangle}{2m}, \tag{1.53.c}$$

where T is the beam temperature, k_B is the Boltzmann constant, and $\langle A \rangle$ stands for taking the average of the quantity A over the whole phase space. These definitions are correct when a beam is hot enough, however we must not use them for a ultralow temperature beam. Because Eqs. (1.53) include the coherent motion of particles for the evaluation of temperatures. Therefore, instead of the conventional definition, the following new definitions of temperatures have proposed in ref. [28].

$$k_B T_x = \frac{{P_0}^2}{8m} \left(\frac{\epsilon_x}{a_x} \right)^2, \tag{1.54.a}$$

$$k_B T_y = \frac{{P_0}^2}{8m} \left(\frac{\epsilon_y}{a_y} \right)^2, \tag{1.54.b}$$

$$k_B T_z = \frac{{P_0}^2}{8m}\left(\frac{\epsilon_z}{a_x}\right)^2, \tag{1.54.c}$$

where $\epsilon_x = 4\sqrt{\langle x^2\rangle\langle {P_x}^2\rangle - \langle xP_x\rangle^2}/m\beta_0\gamma_0 c$, $\epsilon_y = 4\sqrt{\langle y^2\rangle\langle {P_y}^2\rangle - \langle yP_y\rangle^2}/m\beta_0\gamma_0 c$ $\epsilon_z = \sqrt{\langle x^2\rangle\langle {P_z}^2\rangle - \langle xP_z\rangle^2}/m\beta_0\gamma_0 c$, $a_x = 2\sqrt{\langle x^2\rangle}$, and $a_y = 2\sqrt{\langle y^2\rangle}$ respectively. As is shown in Eqs. (1.54), in the new definition of temperature, the beam emittance is used for the calculation of the beam temperature. Thanks to this new defitition, we are able to evaluate the beam temperature without the coherent motion of particles.

1.1.5 Liouville's theorem

It is well known that the 6 dimensional-phase-space volume of a dynamical system is constant if it obeys Hamiltonian formalism. It is called Liouville's theorem [8]. Let us prove this theorem below.

First we define $f(x, P_x, y, P_y, z, P_z, t)$ as a function of the phase-space density. From the equation of continuity, a following equation is carried out.

$$\frac{\partial f}{\partial t} + \sum_{i=1}^{3}\left(\frac{\partial(f\dot{q}_\iota)}{\partial q_i} + \frac{\partial(f\dot{P}_\iota)}{\partial P_i}\right) = 0, \tag{1.55}$$

where q_i and p_i are canonical variables. The total derivative of the phase-space density $f(x, P_x, y, P_y, z, P_z, t)$ is expressed as

$$\frac{df}{dt} = \frac{\partial f}{\partial t} + \sum_{i=1}^{3}\left(\frac{\partial f}{\partial q_i}\frac{\partial q_i}{\partial t} + \frac{\partial f}{\partial P_i}\frac{\partial P_i}{\partial t}\right), \tag{1.56}$$

The Eq. (1.56) can be transformed as follows by Eq. (1.55), in addition, Eq. (1.58) is concluded in the Hamiltonian formalism.

$$\frac{df}{dt} = -f\sum_{i=1}^{3}\left(\frac{\partial}{\partial q_i}\frac{\partial q_i}{\partial t} + \frac{\partial}{\partial P_i}\frac{\partial P_i}{\partial t}\right). \tag{1.57}$$

$$\frac{\partial q_i}{\partial t} = \frac{\partial H}{\partial P_i}, \qquad -\frac{\partial P_i}{\partial t} = \frac{\partial H}{\partial q_i}. \tag{1.58}$$

Finally the total derivative of the phase-space density $f(x, P_x, y, P_y, z, P_z, t)$ leads to

$$\frac{df}{dt} = 0. \tag{1.59}$$

Equation. (1.59) means that the phase-space density is conserved when a dynamical system obeys Hamiltonian formalism. The external force of accelerators are basically comes from the electromagnetic field. In this system, the beam emittance is an invariant. Therefore some dissipative forces are needed in order to decrease a beam emittance. Several methods are known for the effective hadron-beam cooling, for example, the electron cooling, the stochastic cooling, and Doppler laser cooling. The theoretical idea employing a laser cooling to decrease a gas temperature had proposed by Wineland in 1975 [12]. This method enables us to decrease a temperature of an atom on the order of mK instantly. After that several laser cooling methods have been found. Doppler laser cooling method is recognized as the most effective way for a beam cooling. We will explain a principle of Doppler laser cooling in the Sect. 2.2.

1.2 Space charge effects

Charged-particle beams in regular machines are generally quite hot and low density in real space, which means that the motion of each individual particle is approximately independent of others. Recent progress in accelerator technologies is, however, making it possible to produce extremely intense or high-power hadron beams where inter-particle Coulomb interactions play a noticeable role. For instance, the strong Coulomb potential can be a source of liner and nonlinear *coherent resonances* that can seriously affect the beam stability. In this subsection, a brief description is given of some theoretical models useful to explore the collective motion of space-charge-dominant beams. For simplicity, we here concentrate upon the transverse betatron motion, ignoring the synchrotron oscillations of particles in the longitudinal direction.

1.2.1 Vlasov-Poisson model

In order to investigate space-charge-induced collective effects in intense beams, the scalar potential ϕ_{sc} of the Coulomb interaction has to be included explicitly in the betatron Hamiltonian in Eq. (1.11):

$$H = \frac{1}{2}\left({p_x}^2 + {p_y}^2\right) + \frac{1}{2}\left(K_x(s)x^2 + K_y(s)y^2\right) + \frac{q\phi_{sc}(x,y,s)}{m{\gamma_0}^3{\beta_0}^2c^2}. \tag{1.60}$$

The third term on the right hand side is the source of various collective effects when the beam density is high. Since the Coulomb potential is multiplied by the factor $1/\beta_0^2\gamma_0^3$, the space-charge effects are particularly severe in a region of low beam energy. Given the number density $n(x,y,s)$ of charged particles forming the beam, the corresponding Coulomb potential can be calculated from the Poisson equation

$$\Delta\phi_{sc}(x,y,s) = -\frac{q}{\varepsilon_0}n(x,y,s). \tag{1.61}$$

Needless to say, the particle distribution within a beam evolves in a complex manner as a result from nonlinear Coulomb interactions. The density $n(x,y,s)$ in real space is obtained from the distribution function $f\left(x,y,p_x,p_y,s\right)$ in four-dimensional transverse phase space by integrating it over momentum space:

$$n(x,y,s) = \int f\left(x,y,p_x,p_y,s\right)\, dp_x dp_y. \tag{1.62}$$

The function *f* obeys the Boltzmann equation

$$\frac{\partial f}{\partial s} + [f,H] = \left.\frac{\partial f}{\partial s}\right|_{collision}, \tag{1.63}$$

where the right hand side is referred to as the *collision term*, and [,] stands for the Poisson bracket. Since Coulomb collisions among individual particles are generally negligible in a regular beam as already noted, we usually drop the collision term and adopt the simpler *Vlasov equation*

$$\frac{\partial f}{\partial s} + [f,H] = 0. \tag{1.64}$$

Instead of the Boltzmann equation. Naturally, the Vlasov equation requires the Hamiltonian to be well defined. The Hamiltonian in Eq. (1.60) depends on the scalar potential ϕ_{sc} determined by the Poisson equation in Eq. (1.61). To solve the Poisson equation, we need to know the number density in advance, but $n(x,y,s)$ comes from the distribution function *f* satisfying the Vlasov equation. For a self-consistent treatment of space-charge effects, therefore, we must simultaneously solve the Vlasov and Poisson equations together with the Hamiltonian. It is, however, hopelessly difficult to find a self-consistent solution to the Vlasov-Poisson equations when the external driving force is time-dependent. Multi-particle computer simulations are thus often

employed to clarify the collective behavior of hadron beams in modern high-intensity and/or high-power accelerators. For instance, the Particle-In-Cell (PIC) simulation technique is very popular these days and has actually become a very useful means to collective beam dynamics due to the recent rapid improvement of CPU performance.

It is probably impossible to construct a purely analytic theory that self-consistently describes the time evolution of an arbitrary initial distribution function. Past theoretical attempts to solve the Vlasov-Poisson equations thus mostly rely on a perturbative approach. Specifically, we first find a certain stationary distribution f_0 that satisfies the Vlasov equation. The distribution function is then separated into two parts as $f = f_0 + \delta f$ where δf is small perturbation to the stationary state. The Hamiltonian and the Coulomb potential are also separated into two parts as $H = H_0 + \frac{q\delta\phi_{sc}(x,y,s)}{m{\gamma_0}^3{\beta_0}^2c^2}$ and $\phi_{sc} = \phi_{sc_0} + \delta\phi_{sc}$ where H_0 is the stationary Hamiltonian that includes the stationary Coulomb potential ϕ_{sc_0}. This allows us to expand the basic equations about the stationary state. Leaving only linear perturbative terms, we have

$$\frac{\partial \delta f}{\partial s} + [\delta f, H_0] = \frac{q}{m{\gamma_0}^3{\beta_0}^2c^2}[\delta\phi_{sc}, f_0]. \tag{1.65}$$

$$\Delta\delta\phi_{sc} = -\frac{q}{\varepsilon_0}\int \delta f \, dp_x dp_y. \tag{1.66}$$

This equation is still difficult to solve especially for periodic lattices. Hofmann et al. developed a numerical theory over thirty years ago, taking the Kapchinsky-Vladimirsky (KV) model explained in the next section. A fully analytic theory for a one-dimensional sheet beam was constructed by Okamoto and Yokoya who derived the general condition of space-charge-induced coherent resonance [29].

1.2.2 Kapchinsky-Vladimirsky distribution

It is straightforward to define a stationary state in a uniform focusing channel. Since the driving force is completely static, the corresponding Coulomb potential ϕ_{sc} is independent of s, which makes the Hamiltonian itself a constant of motion. An arbitrary function of the stationary Hamiltonian can then be a solution to the Vlasov equation (recalling the fact that Eq. (1.61) can be rewritten as $df/ds = 0$). This is why most Vlasov theories in the past have employed the smooth approximation. In contrast, it is

extremely difficult to define a perfect stationary state when the beam is exposed to a periodic focusing force. Kapchinsky and Vladimirsky discovered that the following distribution function satisfies the Vlasov-Poisson equations, no matter whether the external beam-focusing potential is periodic or uniform:

$$f_0(J_x, J_y) = \frac{N}{\pi \epsilon_x \epsilon_y} \delta\left(1 - \frac{J_x}{\epsilon_x} - \frac{J_y}{\epsilon_y}\right), \tag{1.67}$$

where $\delta\left(1 - \frac{J_x}{\epsilon_x} - \frac{J_y}{\epsilon_y}\right)$ is the Dirac's delta function, N is the number of particles in the beam per unit length in the longitudinal direction, ϵ_x and ϵ_y are full emittances in the transverse directions.

We can obtain the real space distribution of KV distribution by integrate the velocity space [30, 31].

$$n(x, y, s) = \frac{N}{\pi \epsilon_x \epsilon_y} \int \delta\left(1 - \frac{J_x}{\epsilon_x} - \frac{J_y}{\epsilon_y}\right) dp_x dp_y = \begin{cases} \frac{N}{\pi r_x r_y}, & \text{if } \frac{x^2}{{r_x}^2} + \frac{y^2}{{r_y}^2} \leq 1 . \\ 0 & \text{otherwise,} \end{cases} \tag{1.68}$$

where r_x and r_y are the edge beam radius of each direction. As we confirmed from Eq. (1.68), the real space distribution of KV distribution is uniform. Due to this fact, we obtain the self-field potential of a KV beam as

$$\phi_{sc}(x, y, s) = -\frac{qN}{2\pi\varepsilon_0}\left[\frac{x^2}{r_x(r_x + r_y)} + \frac{y^2}{r_y(r_x + r_y)}\right]. \tag{1.69}$$

As a result, we rewrite the Hamiltonian of a beam in the case of KV distribution as

$$H = \frac{1}{2}\left({p_x}^2 + {p_y}^2\right) + \frac{1}{2}\left[K_x(s) - \frac{2K_{sc}}{r_x(r_x + r_y)}\right] x^2 + \frac{1}{2}\left[K_y(s) - \frac{2K_{sc}}{r_y(r_x + r_y)}\right] y^2, \tag{1.70}$$

where K_{sc} is expressed as $K_{sc} = Nq^2/2\pi\varepsilon_0 m{\gamma_0}^3{\beta_0}^2c^2$.

The KV distribution is currently the only known, perfectly self-consistent solution to the Vlasov-Poisson equations with a *s*-dependent external focusing potential. The KV model has thus been often adopted for stability studies of intense hadron beams. In reality, however, the distribution of any particle beam is quite different from the unique four-dimensional spherical shell as in Eq. (1.67) that produces a completely linear space-charge force. We must thus be careful in interpreting theoretical results based on the KV model. This distribution actually has a unique instability mechanism (known as

the KV instability) that is activated at high beam density [32, 33-41].

1.2.3 Root-mean-squared envelope equations

It is convenient to consider rms quantities instead of single-particle quantities because we can only observe a sort of averages in actual experiments. In particular, we often pay attention to the second moments of canonical variables. The temperature definition in Eq. (1.54) is one such example. The concept of rms beam size is also frequently employed in past various studies of beam dynamics. The horizontal rms beam size x_{rms} can be evaluated by averaging x^2 with the distribution function *f* over the whole phase space:

$$x_{rms} = \sqrt{\langle x^2 \rangle} = \sqrt{\int x^2 f(x, y, p_x, p_x) dx dy dp_x dp_y}. \tag{1.71}$$

Needless to say, we can define similar rms quantities for other variables. Making use of the Vlasov equation in Eq. (1.64) and the canonical equations derived from Eq. (1.60), we can obtain the so-called rms envelope equations

$$\frac{d^2 x_{rms}}{ds^2} + K_x(s) x_{rms} - \frac{{\epsilon_{rms}^{(x)}}^2}{x_{rms}^3} - \frac{2K_{sc}}{x_{rms} + y_{rms}} = 0, \tag{1.72.a}$$

$$\frac{d^2 y_{rms}}{ds^2} + K_y(s) y_{rms} - \frac{{\epsilon_{rms}^{(y)}}^2}{y_{rms}^3} - \frac{2K_{sc}}{x_{rms} + y_{rms}} = 0, \tag{1.72.b}$$

where $\epsilon_{rms}^{(x)}$ and $\epsilon_{rms}^{(y)}$ are the rms beam emittances defined by $\epsilon_{rms}^{(x)} = \sqrt{\langle x^2 \rangle \langle {p_x}^2 \rangle - \langle x p_x \rangle^2}$ and $\epsilon_{rms}^{(y)} = \sqrt{\langle y^2 \rangle \langle {p_y}^2 \rangle - \langle y p_y \rangle^2}$. Sacherer proved that this set of coupled equations strictly folds for an arbitrary phase-space distribution as long as the transverse beam profile has elliptical symmetry [42]. Note that the second-moment equations in Eq. (1.72) form a closed set if the time evolutions of the rms emittances are known a priori. In general $\epsilon_{rms}^{(x)}$ and $\epsilon_{rms}^{(y)}$ are constants after beam injection, $K_x(s)$ and $K_y(s)$ are periodic functions of an independent variable s, then x_{rms} and y_{rms} should be periodic functions of s. When a beam injected into an accelerator, we should change a beam shape into the proper shape in phase space. This is called as a beam matching. If we don't transact a beam matching, several serious problems will happen, for example beam instabilities and a beam halo formation. From Eq. (1.72) we can obtain the periodic function of x_{rms} and y_{rms} numerically and we

avoid an emittance growth and a formation of a beam halo.

When we investigate a higher mode collective oscillation, we have to use a higher order momentum equation. Actually beams have infinite collective mode, therefore we can't deal with every mode analytically in principle. As we mentioned before, $\epsilon_{rms}^{(x)}$ and $\epsilon_{rms}^{(y)}$ are constants, therefore Eq. (1.72.a) and (1.72.b) become the second momentum equations. In order to make an analytic estimate of the tunes of linear collective modes, let us assume a coasting round beam for the sake of simplicity. We further apply the smooth approximation, replacing the focusing functions $K_{x(y)}(s)$ by a constant parameter $k_\perp$. The envelope equations can then be simplified to give

$$\frac{d^2 x_{rms}}{ds^2} + {k_\perp}^2 x_{rms} - \frac{{\epsilon_{rms}}^2}{x_{rms}^3} - \frac{K_{sc}}{x_{rms}} = 0, \tag{1.73}$$

where $\epsilon_{rms}^{(x)} = \epsilon_{rms}^{(y)} \equiv \epsilon_{rms}$, and the same equation holds for y_{rms}. In a stationary state where $x_{rms} \equiv x_0 = const.$, the above equation leads to

$$x_0 = \frac{1}{k_\perp}\sqrt{\frac{K_{sc} + \sqrt{{K_{sc}}^2 + 4{\epsilon_{rms}^{(x)}}^2 {k_\perp}^2}}{2}}. \tag{1.74}$$

If we neglect a space-charge effect, a beam tune can be represented as $\nu_0 = \rho_0 k_\perp / 2\pi$, however a space-charge effect is included, a beam tune can be written as $\nu = \rho_0\sqrt{{k_\perp}^2 - K_{sc}/x_0^2}/2\pi$. It means a beam tune is depressed by Coulomb self-force. We usually use σ_0 and σ as an indicator of beam intensity. This parameter is called tune-depression and it's expressed by

$$\eta = \frac{\nu}{\nu_0} = \sqrt{1 - \frac{K_{sc}}{{k_\perp}^2 x_0^2}}. \tag{1.75}$$

Suppose that x_{rms} and y_{rms} is expressed as $x_{rms} = x_0 + \delta x(s)$ and $y_{rms} = x_0 + \delta y(s)$ respectively. Substitute them into Eqs. (1.72.a) and (1.72.b), we reached to the following equations.

$$\frac{d^2\delta x(s)}{ds^2} + \frac{1}{2{\rho_0}^2}(3{\nu_0}^2 + 5\nu^2)\delta x(s) + \frac{1}{2{\rho_0}^2}({\nu_0}^2 - \nu^2)\delta y(s) = 0, \tag{1.76.a}$$

$$\frac{d^2\delta y(s)}{ds^2} + \frac{1}{2{\rho_0}^2}(3{\nu_0}^2 + 5\nu^2)\delta y(s) + \frac{1}{2{\rho_0}^2}({\nu_0}^2 - \nu^2)\delta x(s) = 0. \tag{1.76.b}$$

Define $\delta X_1(s) = \delta x(s) + \delta y(s)$ and $\delta X_2(s) = \delta x(s) - \delta y(s)$ as a new variable,

finally we obtain following equations.

$$\frac{d^2\delta X_1(s)}{ds^2} + \frac{2}{{\rho_0}^2}({\nu_0}^2 + \nu^2)\delta X_1(s) = 0, \tag{1.77.a}$$

$$\frac{d^2\delta X_2(s)}{ds^2} + \frac{1}{{\rho_0}^2}({\nu_0}^2 + 3\nu^2)\delta X_2(s) = 0. \tag{1.77.b}$$

Two collective-oscillation modes can be given from Eqs. (1.77) as

$$\nu_{breathing} = \sqrt{2({\nu_0}^2 + \nu^2)}, \qquad \nu_{quadrupole} = \sqrt{{\nu_0}^2 + 3\nu^2}\,. \tag{1.78}$$

These collective modes are called a breathing mode and a quadrupole mode. The systematic study of the rms-envelope equation of several kinds of beams had done by Sacherer. We can see his study in Ref. [43].

2 Optimization of laser-cooling parameters for beam crystallization at the storage ring S-LSR

2.1 Crystalline beam

As already mentioned, the emittance, i.e. the phase-space volume occupied by a beam, is a measure of the beam quality. The quality becomes higher as the emittance is reduced. Since the emittance is proportional to the beam temperature, we can state that a beam with lower temperature has higher quality. Recently, particle accelerators have been applied to diverse purposes and, as a result, beam users of various fields are demanding higher quality beams. In theory, it is possible to construct the ultimate "zero-emittance" state or, in other words, "zero-temperature" state where the beam is Coulomb crystallized. The concept of beam crystallization was first discussed by Russian researchers in early 1980's when they tried to explain anomalous Schottky signals from proton beams electron-cooled in the NAP-M ring [44, 45]. Later, Schiffer and his co-workers conducted a systematic theoretical study of beam crystallization, employing the molecular dynamics (MD) technique [46]. His seminal work was generalized by Wei and others who incorporated the discrete AG lattice structure of a storage ring into MD simulations [47-50].

There are several beam cooling method applicable to a hadron beam; namely, electron cooling [9], stochastic cooling [10], and laser cooling [11, 12]. Among them, laser cooling is the most powerful while this method is applicable to limited ion species. Doppler laser cooling of a heavy-ion beam was first carried out at the Test Storage Ring (TSR) of the Max Planck Institute, Heidelberg [13], and then at the ASTRID ring of Aarhus University, Denmark [14]. These proof-of-principle experiments in Europe were successful, reducing the longitudinal beam temperature down to an ultracold level. Reaching a Coulomb crystallized state in these cooler rings was, however, found to be physically impossible due to the lack of several essential conditions [47]. Twenty years after the European attempts, another compact ring equipped with a Doppler laser cooling system was constructed at Kyoto University [15, 51]. The ring was named S-LSR, the abbreviation of "Small Laser-equipped Storage Ring". Compared to TSR

and ASTRID, S-LSR has an AG lattice more suitable for beam crystallization. In addition, this machine was designed to allow the application of the so-called *resonant coupling method* that is a key to transverse laser cooling [17, 18].

In the following sections, we first explain the physical properties of a crystalline beam, and the principle of laser cooling. The careful optimization of laser-cooling parameters is performed considering the actual experimental conditions of S-LSR. The MD simulation code CRYSTAL [19] is employed for this purpose. We shall numerically demonstrate that the production of a one-dimensionally ordered unltracold beam is feasible in S-LSR.

2.1.1 Properties of a crystalline beam

It is well known that the structure of a coasting crystalline-beam changes depending on the line density. At low line density, all ions are aligned along the design beam orbit at equal intervals. Such an ordered state is called “string”. Increasing the line density, we can transform the string into a “zigzag” crystal as shown in Fig. 2.1. At higher density, a three-dimensional “shell” structure is eventually formed.

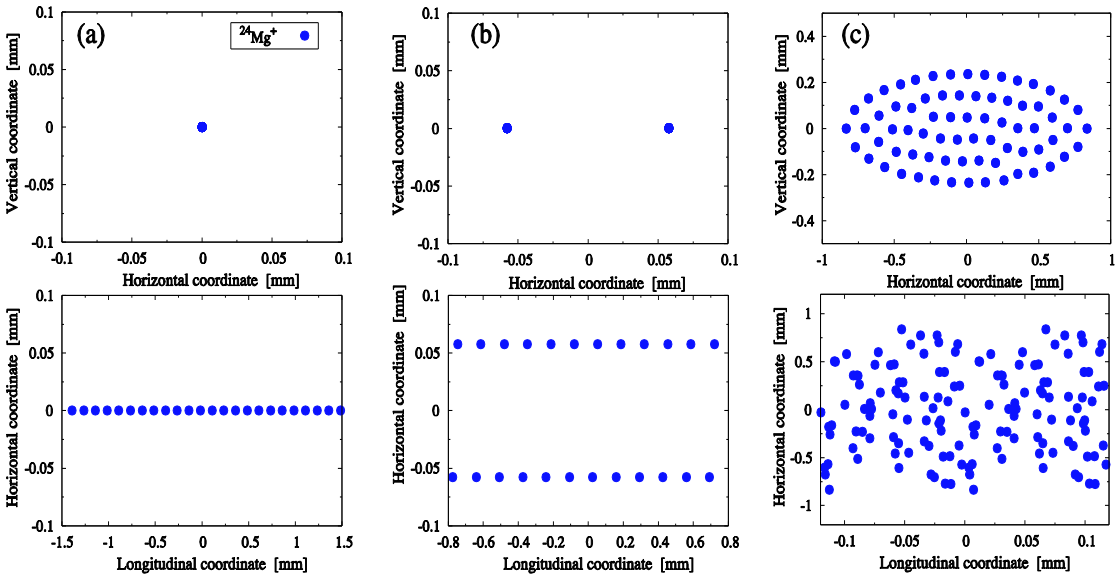

Fig. 2.1: The structure of crystalline beams in real space. Upper panels are transverse planes and lower figures are longitudinal-horizontal planes. A (a) string, (b) zigzag and (c) shells state are formed respectively.

Hasse and Schiffer developed an analytic theory to predict the line density at which a

particular crystalline-configuration is converted into another one [46]. In their theory, the Wigner-Seitz radius defined below plays an important role:

$$a_{WS} = \left[\frac{3q^2}{8\pi\varepsilon_0 m(\sigma\omega_0)^2}\right]^{\frac{1}{3}}, \tag{2.1}$$

Making use of the Wigner-Seitz radius, we introduce the dimensionless line-density

$$\lambda = N a_{WS}, \tag{2.2}$$

where λ is the dimensionless line-density. Hasse and Schiffer derived the transition line-densities listed in Table 2.1 [46]. The validity of their theoretical predictions has been confirmed with past MD simulations.

Table 2.1: The relation between line density and crystalline structure

Line density	Crystalline structure
$0 < \lambda < 0.709$	String (1D)
$0.709 < \lambda < 0.964$	Zigzag (2D)
$0.964 < \lambda < 3.10$	Single shell (3D)
$3.10 < \lambda < 5.70$	Single Shell + String (3D)
$5.70 < \lambda < 9.50$	Double shells (3D)

2.1.2 Coulomb coupling parameter

The phase of a non-neutral plasma can be characterized by the Coulomb-coupling constant

$$\Gamma_C = \frac{q^2}{4\pi\varepsilon_0 d}\frac{1}{k_B T}, \tag{2.3}$$

where $2d$ is the average distance between neighboring particles. A charged-particle beam travelling in an accelerator is generally very and thin, which means that Γ_C is much smaller than unity. Then, the beam is in the *gaseous* state. Γ_C can be made larger by cooling the beam. The so-called *liquid* state is reached when the average Coulomb energy becomes comparable to the average kinetic energy; namely, $\Gamma_C \sim 1$. In the *solid* state where the beam is crystallized, we have $\Gamma_C \geq 170$ [52, 53].

Coulomb crystallization has been experimentally realized in compact ion traps [54, 55]. On the other hand, nobody has succeeded in generating a crystalline beam in a storage-ring accelerator. It, however, seems natural to expect beam crystallization, considering dynamical similarity between an ion trap and an accelerator [56,57]. According to previous theoretical studies [47,50], there are several necessary conditions for a cooler ring to satisfy as explained below. Specifically, the ring must have a proper lattice to avoid collective instability due to linear resonance crossing. Another serious obstacle toward beam crystallization is the existence of momentum dispersion induced by bending magnets. Ion traps are completely free from this effect, which makes it much easier for us to produce a Coulomb crystal. Before proceeding to MD simulations, we describe these fundamental issues of beam crystallization in detail.

・Lattice requirement

As already pointed out in a previous section, there is a possibility of coherent and incoherent beam instabilities depending on the lattice conditions of a storage ring. Once a beam encounters any serious instability, it may just become impossible to cool it further. It is thus quite important to choose a proper operating point, so that no severe beam heating occurs in the cooling process toward an ultracold state. Systematic PIC simulations have indicated that the linear collective resonance is too strong to be overcome with any realistic cooling methods [58]. The condition to avoid this type of resonance can be derived from the rms envelope equation. As shown in Sec. 1.2.4, we can find the tunes of the linear coherent modes (breathing and quadrupole oscillations) from the envelope equation. It is known that a collective oscillation mode becomes resonantly unstable when its tune comes close to a half integer [29]. For the breathing mode, the collective resonance condition can be written as

$$\sqrt{2(\sigma_0{}^2 + \sigma^2)} = \frac{N_{sp}}{2}, \tag{2.4}$$

where N_{sp} is the lattice superperiodicity of the storage ring. As the beam cooling process advances, the left hand side of Eq. (2.4) becomes smaller because σ approaches zero. At the low temperature limit, we have $\sigma_{breathing} = \sqrt{2}\,\sigma_0$ from which we can derive the so-called *maintenance condition* $\sigma_0 < N_{sp}/2\sqrt{2}$ [47]. Note, however, that at the

beginning σ is close to σ_0 rather than zero. σ_0 should thus be smaller than $N_{sp}/2\sqrt{2}$ to avoid the linear resonance throughout the whole cooling process toward the zero-temperature state. Since $\sigma \approx \sigma_0$ at the initial stage of cooling, the ring has to meet the following lattice requirement [58]:

$$\sigma_0 \leq \frac{N_{sp}}{4}. \qquad (2.5)$$

• Cooling requirement

After the beam injection into an accelerator, we start the laser cooling in order to produce a crystalline beam. However, due to a property of the laser cooling, we only can decrease the beam temperature of the longitudinal direction. In the past laser-cooling experiments of a hadron beam, for example ASTRID or TSR, the transverse-beam temperature decreased by intra-beam scattering (IBS). But the cooling effect from the IBS is not strong enough to overcome the IBS heating rate of a liquid state like shown in a following figure. Because of this problem they could not produce a crystalline beam. To improve this problem, an epoch-making method was established [17, 18], this method is called a resonance-coupling method (RCM). Thanks to this idea we expect to obtain a strong transverse-cooling force with a conventional component of accelerators.

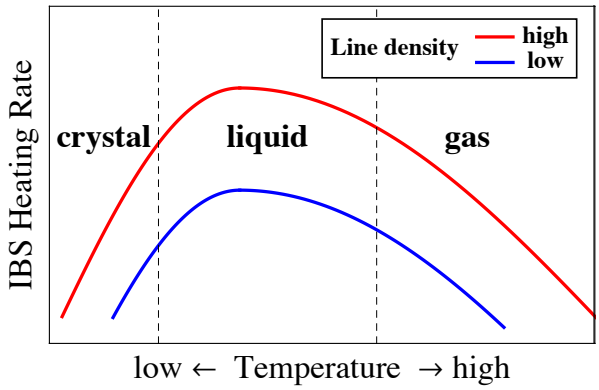

Fig. 2.2: The IBS heating rate as a function of the beam temperature. According to the previous studies it is known that the maximum heating rate exists in the range of liquid state.

The storage ring S-LSR in Kyoto University is the unique accelerator equipped with the laser-cooling system and a resonance-coupling method. An innovative beam-cooling experiment had been done with S-LSR.

・**Tapered cooling**

The Strong-cooling force is the fundamental-physical condition for the production of a crystalline beam. According to the past laser-cooling experiments, Doppler laser cooling enables us to reduce the longitudinal-beam temperature on the order of mK, so the longitudinal velocities of all particles settle into almost the same value. As shown in Fig. 2.1, a 3D crystalline beam spreads in the horizontal degree of freedom, so the lap time of each particle has different value respectively, as a result the laser-cooling method can't maintain the shell structure of a crystalline beam. This is called the bending-shear effect. A string and a zigzag crystalline beams would be generated by Doppler laser cooling because they don't have the spatial spread in horizontal direction.

In order to produce a 3D crystalline beam, we should prepare a particular-cooling force that enables us to produce a beam condition like Fig 2.3. The candidate of this special-cooling force has proposed in the these references [47,50,60], and that can be written as

$$\Delta\left(\frac{\delta p}{p}\right) = -f_z\left[\left(\frac{\delta p}{p}\right) - \frac{\gamma_0 C_{xz}}{\rho_m}x\right], \qquad (2.6)$$

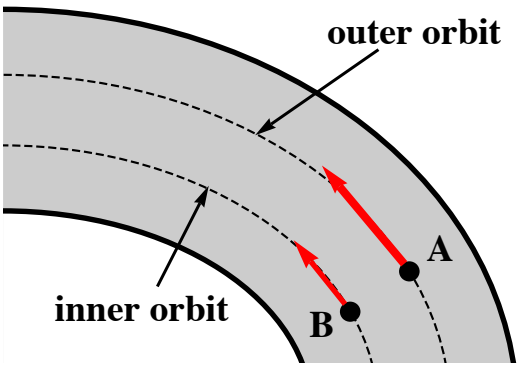

Fig. 2.3: To maintain a crystal structure of the shell state, the special cooling force which enable us to keep the beam velocity as a function of the horizontal amplitude is necessary. The special cooling force is known as a tapered cooling.

where f_z is the strength of the longitudinal-linear-friction force and C_{xz} is the tapering factor. This cooling method is called Tapered cooling [47,50,60]. At the equilibrium state, we have $\Delta(\delta p/p) = 0$, so the tapering factor C_{xz} is written as

$$C_{xz} = \frac{\rho_m}{\gamma_0 x}\frac{\delta p}{p}. \tag{2.7}$$

In addition, a betatron oscillation is completely suppressed at crystal state, the following condition will be satisfied.

$$x = \mathcal{D}_x(s)\frac{\delta p}{p}, \tag{2.8.a}$$

$$y = \mathcal{D}_y(s)\frac{\delta p}{p}, \tag{2.8.b}$$

where $\mathcal{D}_x(s)$ and $\mathcal{D}_y(s)$ are the periodic-orbit function given from the following equations.

$$\frac{d^2\mathcal{D}_x(s)}{ds^2} + K_x(s)\mathcal{D}_x(s) - \frac{K_{sc}}{2\langle(\delta p/p)^2\rangle(\mathcal{D}_x(s) + \mathcal{D}_y(s))} = \frac{1}{\rho}, \tag{2.9.a}$$

$$\frac{d^2\mathcal{D}_y(s)}{ds^2} + K_y(s)\mathcal{D}_y(s) - \frac{K_{sc}}{2\langle(\delta p/p)^2\rangle(\mathcal{D}_x(s) + \mathcal{D}_y(s))} = 0 \tag{2.9.b}$$

Finally we obtain Eq. (2.10) as a relational expression.

$$C_{xz} = \frac{\rho_m}{\gamma_0 \mathcal{D}_x(s)}. \tag{2.10}$$

2.2 Doppler laser cooling

2.2.1 Principle

The principle of Doppler laser cooling is based on resonant interactions between laser photons and ions [61, 62]. Figures 2.4 and 2.5 illustrate how Doppler cooling works.

(a) Suppose an ion that is not fully stripped and moving along a particular orbit at the velocity v. This ion is assumed to have a closed transition between the ground state and a certain excited level. The transition angular frequency is ω_0. We introduce a laser light along the same orbit and let it interact with the moving ion.

(b) The angular frequency ω_L of the laser light seen from the ion is Doppler shifted depending on the velocity v. If we adjust ω_L to the resonant frequency ω_0, this ion

absorbs a single photon and is excited to the upper level. In this process, the ion is slightly accelerated (or decelerated) along the direction of the laser propagation, receiving the tiny momentum of the photon.

(c) Provided the lifetime of the upper state is short, the excited ion immediately comes back to the ground level emitting a single photon. In this process, the ion gains the recoil momentum. The recoil effect, however, becomes negligible after absorption and emission of many photons because the photon emission is spatially isotropic.

(d) Finally, the ion is in the original ground state but the velocity is slightly changed along the orbit.

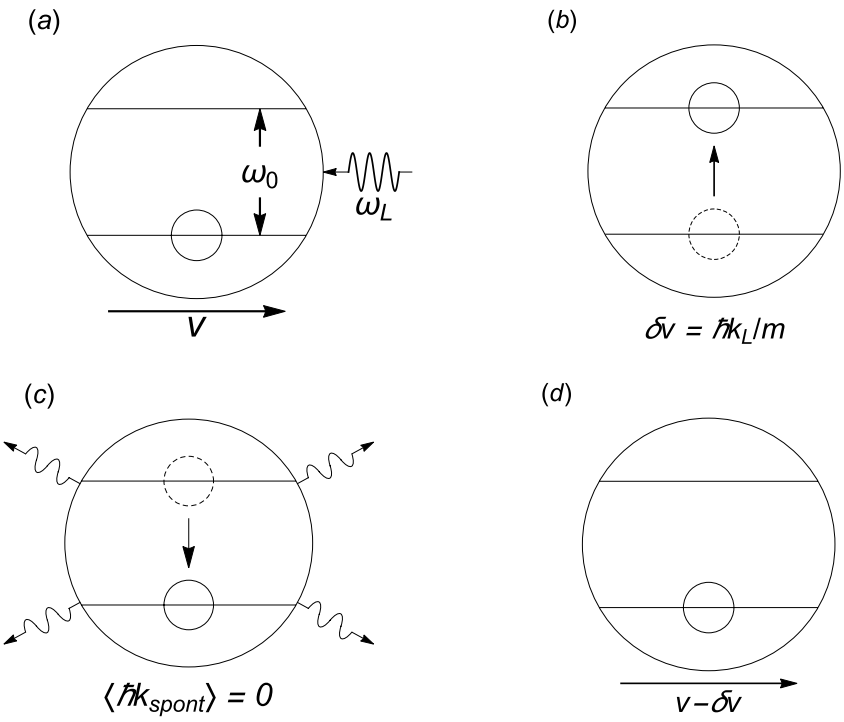

Fig. 2.4: A principle of Doppler laser cooling. The velocity of an ion is controllable by absorption and emission of photons.

We employ the basic cycle in Fig. 2.4 to decrease the temperature of an ion beam. Let us assume that the beam initially has a Maxwell velocity distribution of ions in the longitudinal direction, as shown in Fig. 2.5(a). By properly choosing the angular laser frequency ω_L of a laser in the laboratory frame, we can accelerate ions within a very narrow velocity region as indicated in Fig. 2.5(b). We then slightly shift the laser

frequency in order to have resonance continuously with those accelerated ions. After a frequency scan over possible Doppler shifts, we reach the final velocity distribution in Fig. 2.5(c) where the majority of ions are confined within a narrow range. Note that the laser light must be injected along a straight section of the storage ring, so that the beam can interact with many photons over a certain distance; otherwise, no efficient cooling takes place. This means that Doppler cooling is effective only in the direction of beam motion.

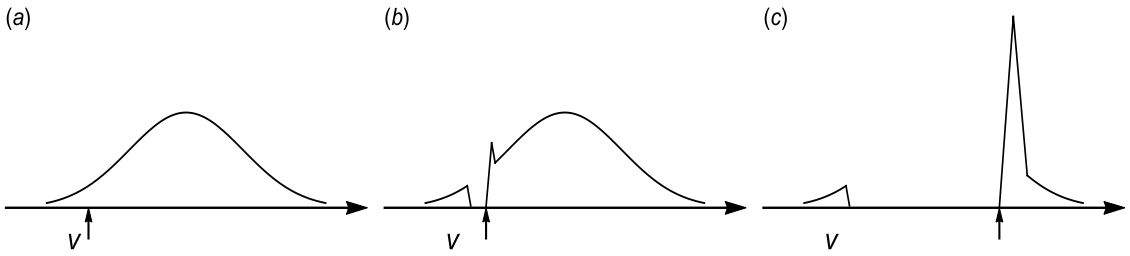

Fig. 2.5: The process of Doppler laser cooling with a sweep laser frequency is shown in the velocity space.

2.2.2 Optimization of laser frequency detuning

As we explained in the previous section, a laser has an ability of producing the dissipative force that can decrease a beam temperature. The formula of the laser dissipative force F_L is known as a following function when an ion has a Lorentzian of transition.

$$F_L(v_Z) = \frac{1}{2}\hbar k_L \Gamma \frac{S}{1 + S + \left(\frac{2}{\Gamma}\Delta\right)^2}, \tag{2.11}$$

where $\hbar k_L$ is the momentum of a laser photon, Γ is a natural-line width of an ion, S is a saturation parameter of a laser, and Δ is a laser detuning. The laser detuning is defined as

$$\Delta = \omega_L \gamma_0 \left(1 - \frac{v_0 + v_z}{c}\right) - \omega_0 . \tag{2.12}$$

The v_0 is a speed of a design particle in the longitudinal direction and v_Z is a speed of an ion from a center-of-mass system of a beam. Therefore a laser detuning means a

difference of the laser frequency for a moving ion in a velocity $v_0 + v_Z$ and the transition frequency of an ion in the laboratory frame. This is one of the most important physical parameter for Doppler laser cooling, because the strength of the cooling force in the laser dissipative force can be decided by a laser detuning. According to a formula (2.11), the following formula can be obtained from the Taylor expansion of Eq. (2.11) by v_Z.

$$F_L(v_Z) \approx \frac{1}{2}\hbar k_L \Gamma \frac{S}{1+S+(2\Delta_0/\Gamma)^2} + 2\hbar {k_L}^2 S \frac{2\Delta_0/\Gamma}{[1+S+(2\Delta_0/\Gamma)^2]^2} v_z \qquad (2.13)$$

$$= F_{L1} + F_{L2} \cdot v_z,$$

here, Δ_0 is a laser detuning of $v_z = 0$, F_{L1} is the constant force, and $F_{L2} \cdot v_z$ is the linear friction force in the longitudinal direction. To maximize the friction force, the following mathematical condition should be satisfied.

$$\frac{dF_{L2}}{d\Delta_0} = 0 \qquad (2.14)$$

Finally, we found Eq. (2.15) as an optimum condition of a laser detuning to maximize the linear friction force.

$$\Delta_0 = \frac{\Gamma}{2}\sqrt{\frac{1+S}{3}}. \qquad (2.15)$$

2.2.3 Doppler limit

The previous studies have verified that Doppler laser cooling can decrease the longitudinal-beam temperature dramatically, however it is well known that there exists the temperature limitation we can reach with this method. It is so-called Doppler limit. Due to the reiteration of the absorption and emission of photons, a momentum in the laser propagating direction is decreased. However the randomness of the absorption and spontaneous emissions of photons give rise to the beam heating. The formulas of the momentum diffusion are written by Eqs. (2.16) and (2.17) respectively.

$$D_{abs} = \frac{1}{2}\hbar^2 k_L^2 \Gamma \frac{S}{1+S+(2\Delta_0/\Gamma)^2}(1+\mathcal{M}). \tag{2.16}$$

$$D_{spn} = \frac{1}{2}\hbar^2 k_L^2 \Gamma \frac{S}{1+S+(2\Delta_0/\Gamma)^2}\alpha_g. \tag{2.17}$$

$\mathcal{M}$ is Mendel parameter [62] and α_g is the geometry factor of the spontaneous emission from ions [62, 63]. From Eq. (2.11), the total friction force from the co-propagating and the counter-propagating lasers are expressed as

$$F_{L2\_total} = 4\hbar {k_L}^2 S \frac{2\Delta_0/\Gamma}{[1+S+(2\Delta_0/\Gamma)^2]^2} v_z = 2F_{L2} \cdot v_z. \tag{2.18}$$

The temperature of Doppler limit can be estimated by the balance between the friction force and the momentum diffusion. Eq. (2.19) shows the balanced dynamical situation. It is given from Eqs. (2.16) − (2.18).

$$-2F_{L2}\langle v_z^2 \rangle + \frac{D}{2m} = 0, \tag{2.19}$$

where D is the momentum diffusion from two lasers expressed as $D = 2(D_{abs} + D_{spn})$, and $\langle v_z^2 \rangle / 2m$ is the longitudinal temperature. Finally we can obtain the beam temperature of Doppler limit.

$$\frac{1}{2}k_B T_z = \frac{D}{8F_{L2}} = \frac{\hbar\Gamma}{16}(1+\mathcal{M}+\alpha_g)\frac{1+S+(2\Delta_0/\Gamma)^2}{2\Delta_0/\Gamma}. \tag{2.20}$$

Suppose that $M \ll 1$ and $2\delta_0/\Gamma = \sqrt{(1+S)/3}$, Eq. (2.27) is transformed as

$$\frac{1}{2}k_B T_z = \frac{\hbar\Gamma}{4}\left(1+\alpha_g\right)\sqrt{\frac{1+S}{3}}. \tag{2.21}$$

If we suppose a one-dimensional system and the low-laser intensity, we achieve the following formula.

$$\frac{1}{2}k_B T_z \approx \frac{\hbar\Gamma}{4}. \tag{2.22}$$

The lowest temperature we can expected from Doppler laser cooling is usually on the order of mK. The beam-cooling experiments with Doppler laser cooling method had been done in 1990's and the effectiveness of laser cooling had confirmed in those experiments. They succeeded to decrease the longitudinal beam temperature, however the temperatures in the transverse direction are still hot compare to the longitudinal direction [13, 14]. Because the reachable temperature in the transverse direction is most

likely limited by intra beam scattering (IBS), therefore the cooling efficiency in the transverse direction is lower than the longitudinal direction. The resonance coupling method was proposed two decades ago to extend a one-dimensional (1D) dissipative effect to the other two degrees of freedom. Thanks to this theory, the strong multi-dimensional cooling comes true.

2.3 Multi-dimensional cooling by means of resonance coupling

The idea of the resonance coupling method had proposed by Okamoto, Sessler, and Möhl in 1994 [17]. Owing to this idea, we are able to extend the cooling effect from the longitudinal to the other two dimensions easily. We explain the concept of the resonance coupling method below.

2.3.1 A theoretical model of multi-dimensional laser cooling

First we suppose the smoothed two-dimensional dynamical system to simplify the physical situation.

$$H = \frac{1}{2}\left({p_x}^2 + {p_y}^2\right) + \frac{1}{2}\left(\nu_x^2 x^2 + \nu_y^2 y^2\right) + K_c xy\,. \tag{2.23}$$

ν_x and ν_y are betatron tunes of each direction and K_c is a factor of the coupling-potential strength. From the Hamiltonian (2.23), the equations of motion for the two degrees of freedom are given as follows.

$$\frac{d^2x}{ds^2} = -\nu_x^2 x - K_c y, \tag{2.24.a}$$

$$\frac{d^2y}{ds^2} = -\nu_y^2 y - K_c x. \tag{2.24.b}$$

Due to the coupling potential, motions of each direction affect each other and when the condition of Eq. (2.25) is satisfied, the temperature exchange will be occurred. The coupling-potential strength K_c determines the frequency of the temperature exchange. This phenomenon is known as the difference resonance referred in sect. 1.1.3. Thanks to the utilization of the difference resonance, the extension of the laser cooling force to the other two degrees of freedom becomes possible.

$$\nu_x - \nu_y \approx integer. \tag{2.25}$$

2.3.2 Optimization of coupling strengths

For circular accelerators, the momentum dispersion can be used for the coupling-potential source. First, according to Eq. (1.8), the beam Hamiltonian of storage rings can be derived as Eq. (2.26). The terms related to the vertical direction are ignored to simplify the problem.

$$H \approx -\frac{\gamma_0}{\rho(s)} x p_z + \frac{1}{2}({p_x}^2 + {p_z}^2) + \frac{1}{2}K_x(s)x^2 + \frac{qE_0}{p_0 h_{rf}\omega_0}\cos\left(\frac{h_{rf}\omega_0}{\beta_0\gamma_0 c}z + \varphi_{rf}\right)\delta_p(s_{rf} - s). \tag{2.26}$$

We suppose the thin-less approximation of a rf cavity, and s_{rf} represents a position of the rf cavity in a circular accelerator.

The temperature comes from the betatron motion should be small to reduce the horizontal emittance. In order to see the effect of the only betatron motion, the canonical transformation with the generation function G_3 enables us to redefine the coordinates without the dispersion effects.

$$G_3 = \widehat{p_x}(x - \gamma_0 D_x \widehat{p_z}) + \gamma_0 D_x' x\widehat{p_z} - \frac{\gamma_0^2 D_x {D_x}'}{2}\widehat{p_z}^2 - z\widehat{p_z} \tag{2.27}$$

From the generation function G_3, we obtain the following canonical transformations.

$$x = \hat{x} + \gamma_0 D_x p_z, \tag{2.28.a}$$

$$p_x = \widehat{p_x} + \gamma_0 {D_x}' p_z, \tag{2.28.b}$$

$$z = \hat{z} + \gamma_0(D_x'\hat{x} - D_x\widehat{p_x}), \tag{2.28.c}$$

$$\widehat{p_z} = p_z. \tag{2.29.d}$$

The Hamiltonian (2.25) can be rewritten by the new canonical variables as

$$H = \frac{\varsigma}{2{\gamma_o}^2}\widehat{p_z}^2 + \frac{1}{2}\widehat{p_x}^2 + \frac{1}{2}K_x(s)\hat{x}^2 + \frac{q\rho_0 E_0}{h_{rf}\beta_o c p_0}\cos\left(\frac{h_{rf}}{\gamma_0\rho_0}\hat{z} + \frac{h_{rf}}{\rho_0}(D_x'\hat{x} - D_x\widehat{p_x})\right)\delta_p(s_{rf} - s). \tag{2.30}$$

We here rewrite the circulate frequency ω_0 as $\beta_0 c/\rho_0$.

For the effective multi-dimension cooling, the cooling efficiency of the horizontal and longitudinal direction should be similar. The strength of the coupling potential is the parameter to optimize the cooling efficiency of the two degrees of freedom, therefore the rf-cavity voltage must be optimized in this case. The theoretical method of optimizing the coupling potential is known as the transfer-matrix theory.

We first have applied the smooth approximation and Taylor expansion of the cosine function to the Hamiltonian (2.30) as follows to simplify the theoretical calculation.

$$\bar{H} = \frac{\varsigma}{2{\gamma_o}^2}\overline{p_z}^2 + \frac{1}{2}\frac{(2\pi\nu_x)^2}{{\rho_0}^2}\bar{x}^2 + \frac{1}{2}\overline{p_x}^2 \qquad (2.31)$$

$$- \frac{q\rho_0 E_0}{h_{rf}\beta_o c p_0}\left[1 - \frac{1}{2}\left(\frac{h_{rf}}{\gamma_0\rho_0}\hat{z} + \frac{h_{rf}}{\rho_0}(D_x'\bar{x} - D_x\overline{p_x})\right)^2\right]\delta_p(s_{rf} - s).$$

In order to calculate the theoretical cooling efficiency, the one-turn transfer matrix is necessary. Therefore we have separated the storage ring into the three parts, an arc-section, a cooling section, and a rf-cavity section. And then define the transfer matrix of each part. We have used the linear friction cooling force in the theoretical calculation. From the Hamiltonian (2.30), the transfer matrix of each section can be expressed as

$$\mathrm{M}_{arc} = \begin{pmatrix} \cos(2\pi\nu_x L_a/\rho_0) & \rho_0\sin(2\pi\nu_x L_a/\rho_0)/2\pi\nu_x & 0 & 0 \\ -2\pi\nu_x\sin(2\pi\nu_x L_a/\rho_0)/\rho_0 & \cos(2\pi\nu_x L_a/\rho_0) & 0 & 0 \\ 0 & 0 & 1 & -\varsigma L_a/{\gamma_o}^2 \\ 0 & 0 & 0 & 1 \end{pmatrix}.$$

$$\mathrm{M}_{cool} = \begin{pmatrix} \cos(2\pi\nu_x L_c/\rho_0) & R_0\sin(2\pi\nu_x L_c/\rho_0)/2\pi\nu_x & 0 & 0 \\ -2\pi\nu_x\sin(2\pi\nu_x L_c/\rho_0)/\rho_0 & \cos(2\pi\nu_x L_c/\rho_0) & 0 & 0 \\ 0 & 0 & 1 & (e^{-F_{lin}L_c} - 1)\varsigma/{\gamma_o}^2 F_{lin} \\ 0 & 0 & 0 & e^{-F_{lin}L_c} \end{pmatrix}.$$

$$\mathrm{M}_{rf\ cavity} = \begin{pmatrix} 1 + \mathcal{A}_1 D_x D_x'/\rho_0 & -\mathcal{A}_1 {D_x}^2/{\rho_0}^2 & \mathcal{A}_1 D_x/\rho_0 & 0 \\ \mathcal{A}_1 {D_x}'^2 & 1 - \mathcal{A}_1 D_x D_x'/\rho_0 & \mathcal{A}_1 D_x' & 0 \\ 0 & 0 & 1 & 0 \\ \mathcal{A}_1 D_x' & -\mathcal{A}_1 D_x/\rho_0 & \mathcal{A}_1 & 1 \end{pmatrix}.$$

L_a is the length of an arc section, L_c is the length of a cooling section, and $-F_{lin}p_z$ is the linear-cooling force. The new characters in $\mathrm{M}_{rf\ cavity}$ are defined as follows.

$$\nu_s{}^2 = \frac{q h_{rf} \varsigma V_0}{2\pi p_o \beta_o c} \quad , \qquad \mathcal{A}_1 = \frac{2\pi \nu_s{}^2}{\varsigma} \tag{2.32}$$

Finally the transfer matrix through a turn of a circular accelerator can be calculated from the following matrix.

$$\mathrm{M}_{one-turn} = \mathrm{M}_{arc}\mathrm{M}_{cool}\mathrm{M}_{rf\ cavity}.$$

It is known the cooling rate of each dimension can be estimated from the eigenvalues of this one-turn transfer matrix and it must be the function of the rf voltage. Therefore we should find the optimum voltage of a rf cavity that satisfy the similar cooling efficiency for both the horizontal and longitudinal direction.

Fig. 2.6 shows the comparison of the theoretical calculation and the single-particle simulation result. The left side of Fig. 2.6, we can see below, is the result of the matrix calculation as a function of rf voltage. The typical horizontal tune in the experiments at S-LSR is 2.07, therefore we set the horizontal tune to $\nu_x = 2.07$ in the calculation.

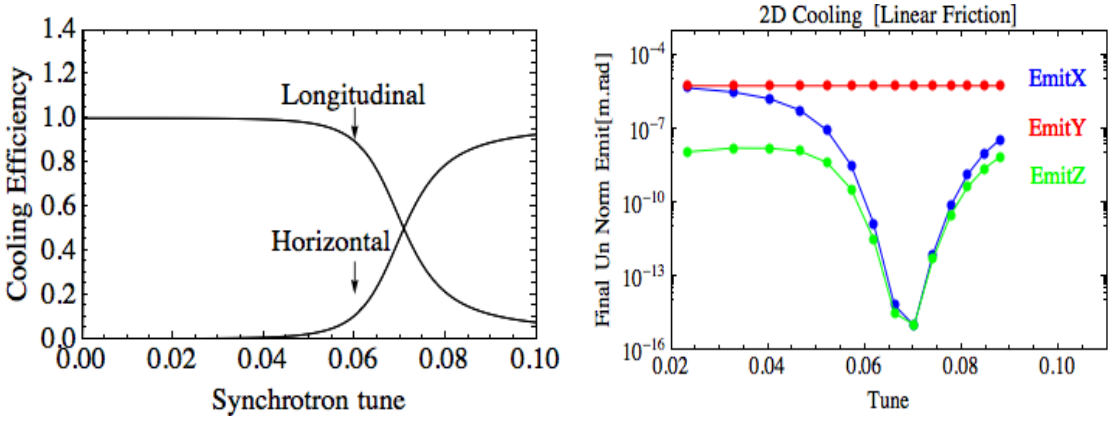

Fig. 2.6: 2D Cooling efficiency of the transfer matrix estimation (left panel) and the single particle simulation with the simulation code "CRYSTAL" (right panel). The maximum longitudinal cooling rate without coupling, i.e. the longitudinal direct cooling efficiency by the laser, is normalized to unity. The sum of the three cooling rates at a certain solenoid field is equal to unity. The good agreement of them is confirmed.

Thanks to the difference resonance, the theoretical calculation shows the similar cooling efficiency of the horizontal and longitudinal direction when the synchrotron tune is around $\nu_z = 0.07$. The right pannel of Fig. 2.6 shows the single-particle simulation results with the simulation code CRYSTAL. The detail of CRYSTAL code is explained in Appendix. A. We apply the linear-friction force in the simulations. The emittances of the horizontal and longitudinal direction at the end of the simulation have minimized when the synchrotron tune have set to 0.07. From these results, the good agreement of the beam cooling efficiency between theoretical calculations and the single-particle simulations has confirmed. The vertical emittance of simulation keeps constant because there is no coupling potential between the vertical and the other two degrees of freedom. We define this multi-dimension cooling as the 2D cooling mode.

Next, consider the 3D cooling mode. In order to extend the dissipative force in the vertical direction, another artificial linear coupling is needed. Past studies have proposed several devices for the new coupling potential sources between the vertical and horizontal direction, for example a skew magnet or a solenoid magnet. The solenoid magnet is adopted as a coupling scheme in S-LSR. First the Hamiltonian of a circular accelerator with the rf cavity and the solenoid magnet can be written as

$$\begin{aligned} H = -\frac{\gamma_0}{\rho(s)} x p_z + \frac{1}{2} {p_z}^2 + \frac{1}{2}\left(K_x(s)x^2 + K_y(s)y^2\right) \\ + \frac{1}{2}\left[\left(p_x + \frac{qB_s(s)y}{2p_o}\right)^2 + \left(p_y + \frac{qB_s(s)x}{2p_o}\right)^2\right] \\ + \frac{qE_0}{p_0 h_{rf}\omega_0}\cos\left(\frac{h_{rf}\omega_0}{\beta_0\gamma_0 c} z + \varphi\right)\delta\left(s - s_{rf}\right). \end{aligned} \tag{2.33}$$

Denoting the axial magnetic field of a solenoid to be B_{sol}, we have $B_s(s) = B_{sol}$ within the solenoid while $B_s(s) = 0$ elsewhere. Similar to the case of the 2D cooling mode, the new coordinate system of free dispersion can be defined and finally we have obtained the Hamiltonian (2.34).

$$
\begin{aligned}
H = \frac{1}{2}\left[-\frac{\varsigma}{{\gamma_o}^2} + g(s)^2{\rho_0}^2\left({D_x}^2 + {D_y}^2\right)\right]\widehat{p_z}^2 + \frac{1}{2}\left[({\nu_x}^2 + g(s)^2{\rho_0}^2)\hat{x}^2 + ({\nu_y}^2 + g(s)^2{\rho_0}^2)\hat{y}^2\right] \\
- \hat{x}\widehat{p_z}\left(g(s)\rho_0 D_y' + g(s)^2{\rho_0}^2 D_x\right) - \hat{y}\widehat{p_z}\left(g(s)\rho_0 D_x' + g(s)^2{\rho_0}^2 D_y\right) \\
+ g(s)\rho_0\widehat{p_z}\left(D_x\widehat{p_y} - D_y\widehat{p_x}\right) + g(s)\rho_0\left(\hat{y}\widehat{p_x} - \hat{x}\widehat{p_y}\right) + \frac{1}{2}\left(\widehat{p_x}^2 + \widehat{p_y}^2\right) \\
+ \frac{q\rho_0 E_0}{h_{rf}\beta_o c p_0}\cos\left(\frac{h_{rf}}{\gamma_0\rho_0}\hat{z} + \frac{h_{rf}}{\rho_0}(D_x'\hat{x} + D_y'\hat{y} - D_x\widehat{p_x} - D_y\widehat{p_y})\right)\delta(s - s_{rf}).
\end{aligned}
\tag{2.34}
$$

where $g(s) = \frac{qB_s(s)}{2p_o}$. The transfer matrix of a solenoid magnet section can thus be given by

$$
\mathrm{M}_{sol} = \begin{pmatrix}
\cos^2(\theta_{sol}) & \frac{1}{g}\cos(\theta_{sol})\sin(\theta_{sol}) & \cos(\theta_{sol})\sin(\theta_{sol}) & \frac{1}{g}\sin^2(\theta_{sol}) & 0 & 0 \\
-g\cos(\theta_{sol})\sin(\theta_{sol}) & \cos^2(\theta_{sol}) & -g\sin^2(\theta_{sol}) & \cos(\theta_{sol})\sin(\theta_{sol}) & 0 & 0 \\
-\cos(\theta_{sol})\sin(\theta_{sol}) & -\frac{1}{g}\sin^2(\theta_{sol}) & \cos^2(\theta_{sol}) & \frac{1}{g}\cos(\theta_{sol})\sin(\theta_{sol}) & 0 & 0 \\
g\sin^2(\theta_{sol}) & -\cos(\theta_{sol})\sin(\theta_{sol}) & -g\cos(\theta_{sol})\sin(\theta_{sol}) & \cos^2(\theta_{sol}) & 0 & 0 \\
A_1 & A_2 & A_3 & A_4 & 1 & A_5 \\
0 & 0 & 0 & 0 & 0 & 1
\end{pmatrix},
$$

where $\theta_{sol} = qB_{sol}L_{sol}/2p_0$ with L_{sol} being the axial length of the solenoid. The new characters in M_{sol} are defined as

$$
A_1 = \frac{g\gamma_0}{2}\left(D_y(\theta_{sol}) + D_y(\theta_{sol})\cos(2\theta_{sol}) + D_x(\theta_{sol})\sin(2\theta_{sol}) - 2D_y(0)\right), \tag{2.35.a}
$$

$$
A_2 = \frac{\gamma_0}{2}\left(D_x(\theta_{sol}) + D_y(\theta_{sol})\sin(2\theta_{sol}) - D_x(\theta_{sol})\cos(2\theta_{sol})\right), \tag{2.35.b}
$$

$$
A_3 = \frac{g\gamma_0}{2}\left(-D_x(\theta_{sol}) - D_x(\theta_{sol})\cos(2\theta_{sol}) + D_y(\theta_{sol})\sin(2\theta_{sol}) + 2D_x(0)\right), \tag{2.35.c}
$$

$$
A_4 = \frac{\gamma_0}{2}\left(D_y(\theta_{sol}) - D_x(\theta_{sol})\sin(2\theta_{sol}) - D_y(\theta_{sol})\cos(2\theta_{sol})\right), \tag{2.35.d}
$$

$$
A_5 = -\frac{\varsigma}{g{\gamma_o}^2}\theta_{sol} + g{\gamma_o}^2\int_0^{\theta_{sol}}\left(D_x(\theta)^2 + D_y(\theta)^2\right)d\theta. \tag{2.35.e}
$$

The transfer-matrix theory is again employed for 3D-cooling system and one-turn matrix can be obtained as

$$\mathrm{M}_{one-turn} = \mathrm{M}_{arc}\mathrm{M}_{cool}\mathrm{M}_{rf\ cavity}\mathrm{M}_{sol}.$$

Needless to say, the eigenvalues of $\mathrm{M}_{one-turn}$ denote the cooling rates of the three directions. The optimum narrow range of the solenoid field strength for the most efficient 3D cooling must be specified theoretically. From the Fig. 2.7, we see that the vertical cooling rate increases at the expense of the cooling rates of the other two directions as the solenoid field is strengthened. The cooling efficiency of the three directions can be made approximately equal when the field strength is about 65 Gauss. The right pannel of Fig. 2.7 is the single particle simulation results with CRYSTAL. The simulation results show the similar tendency with the transfer-matrix theory.

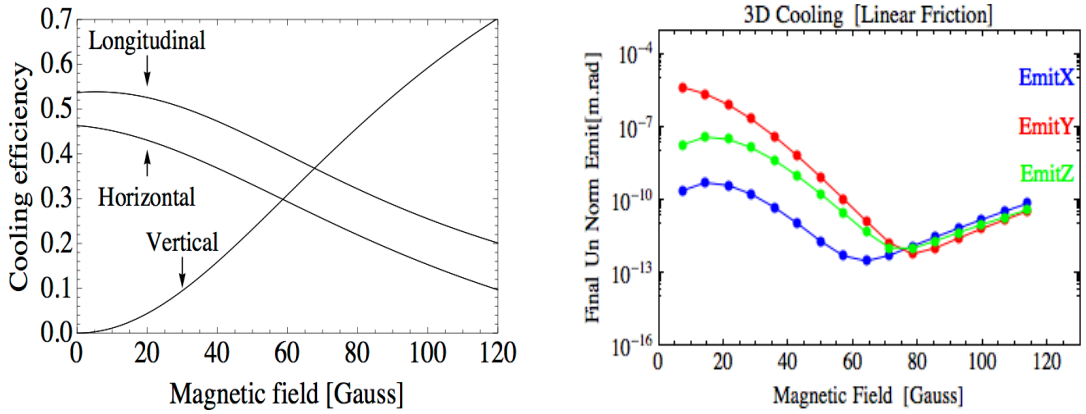

Fig. 2.7: Cooling rates of the three directions estimated from transfer-matrix calculations and the single particle simulations. The lattice parameters in Table 2.2 have been assumed, except for the solenoid field. The good agreement of them is confirmed.

2.4 Molecular dynamics simulations

Accompany with the evolution of calculators, numerical simulations gradually begin to be utilized in many fields recently, for example physics, chemistry, meteorology and social science. In the field of accelerator physics, calculators are often used to explore the space charge effect and to confirm the stability of the beam transport through a lattice. Two simulation methods are mainly employed for the numerical calculation of the multi-particle simulation. The Particle-in-cell code (PIC) and the Molecular-Dynamics code (MD). Each method has strengths and weaknesses, respectively. PIC codes are good at numerical simulations of intense beams but they can't calculate Coulomb collisions between each particle. Therefore we can't use a PIC code for the phenomena where Coulomb collisions have important roles such as crystalline beam. On the other hand, MD code can include accurate Coulomb collisions, however calculation of Coulomb interaction between all particles is very time-consuming when the particle number is large. Therefore MD codes are seldom used for the intense beams simulation. When we consider the multi-dimension cooling in the storage ring S-LSR, the beam intensity is extremely low. Therefore the MD code is available for the numerical simulations of a multi-dimension cooling. In the following section, we explain the storage ring S-LSR at first, and then show the simulation results of the multi-dimension beam cooling.

2.4.1 S-LSR storage ring

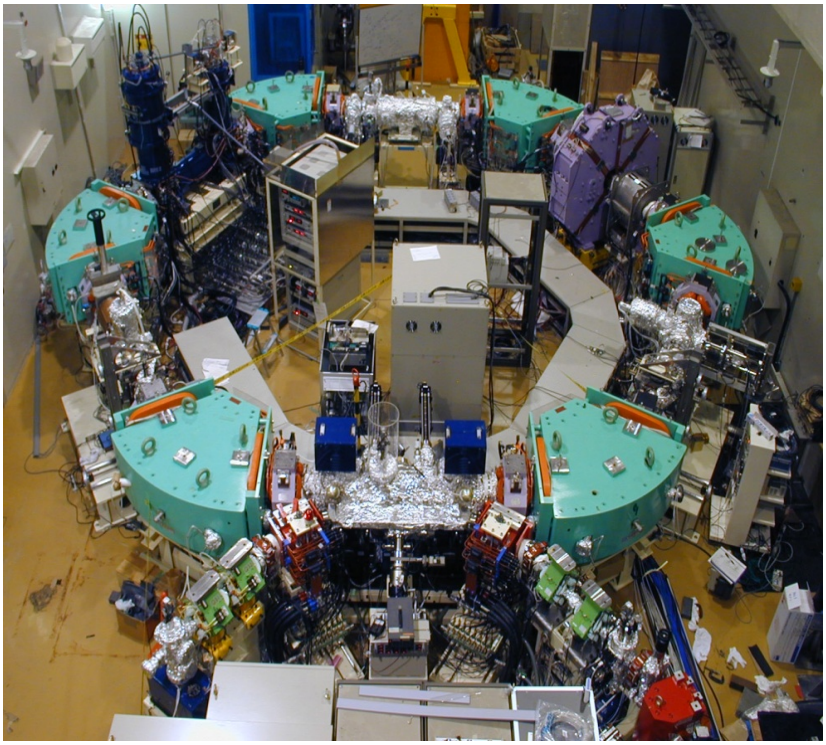

Fig. 2.8 : The storage ring S-LSR in Kyoto University. This accelerator is equipped a laser system, the rf cavity, and the solenoid coil for the experiment of multi-dimensional beam cooling.

Storage ring S-LSR is the circular accelerator in Kyoto University. It was constructed in 2006 and there are several purposes for this accelerator, for example the research of the cancer therapy and the beam cooling with Doppler laser cooling [47, 17, 18]. Fig. 2.8 show the storage ring S-LSR and a schematic drawing of the S-LSR lattice is given in Fig. 2.9. The rf cavity for the longitudinal-horizontal coupling and the solenoid magnet for horizontal-vertical coupling sit in different straight sections. The ion numbers in the bunch reduced by scrapers in order to weaken the effect of the intra-beam scattering (IBS). The cooling laser is introduced in the direction co-propagating with the $^{24}Mg+$ beam. The frequency of the cooling transition of $^{24}Mg+$ ions from the ground state $3s^2S_{1/2}$ to the excited level $3p^2P_{3/2}$ is about 1 PHz, corresponding to a wavelength of 280 nm. The Doppler limit is about 1mK. The reason of six-super periodicity is quite simple. As we said in the section of crystalline beam, Eq. (2.5) should be satisfied to avoid

resonance crossings in the process of the beam cooling. Therefore the minimum tune we are able to set in the transverse direction must be settled to 1.44. Thanks to this transverse tune, we can meet the maintenance condition.

The main parameters of S-LSR for the multi-dimensional beam cooling are shown in Table 2.2. The beam energy is fixed at the extremely low value to achieve the high-laser-cooling efficiency. In the following sections, the optimization of the multi-dimension cooling including space-charge effects will be shown.

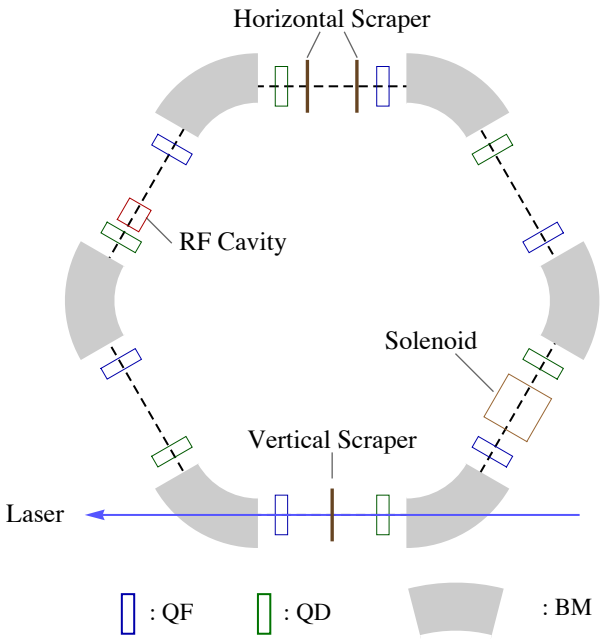

Fig. 2.9: The simple layout of storage ring S-LSR. The beam rotated clockwise and the co-propagating laser, the beam scrapers, the rf cavity, and the solenoid magnet set in each position.

Table 2.2 Main parameters of storage ring S-LSR

Ion species	$^{24}Mg^{+}$
Kinetic energy	40kev
Lorentz factor	$\beta_o = 1.892e-3$ $\gamma_o = 1.00000179$
Ion numbers	~1000 (for a bunch)
Rms beam size	2mm (after scrape a beam)
Momentum spread	7e-4
Circumference of ring	22.56m
Life time of a beam	10 sec
Super period	6
Harmonic number	100
Total laser power (only co-propagating laser)	8.0mW~16.0mW

2.4.2 Two-dimensional cooling

It goes without saying that the high power laser is the essential device for the efficient-Doppler laser cooling experiments. According to the previous studies, the utility factor of the laser cooling method can be estimated by the saturation parameter defined in Eq. (2.11). The saturation parameter of larger than unity is preferred for the efficient laser cooling, however the laser power we apply for the beam cooling experiment at S-LSR is limited only to 10mW. In addition, both the co-propagating and the counter- propagating laser lead beams to the strong cooling, however the S-LSR equips only a single co-propagating laser. Therefore we should determine the optimum laser parameters carefully to enhance the laser-cooling efficiency. For reference, examples of typical-beam profiles before and after multi-dimensional laser cooling are shown in Fig. 2.10. The upper figures are the initial distribution and the lower figures are the final distribution after laser cooling with 2D cooling mode. Owing to the limited laser power at S-LSR as well as strong IBS, a considerable number of ions remain uncooled after a few seconds of cooling. It is possible to remove these hot ions with the scrapers if necessary because they have relatively large transverse oscillation amplitudes. In the following, therefore, we calculate the beam temperature only from the cold laser-cooled portion, disregarding the hot tail particles. In order to separate laser-cooled ions from the other hot ions in MD simulations, we set a tiny closed boundary in each of the horizontal, vertical, and longitudinal phase planes. The area (i.e., emittance) inside each boundary is typically chosen a few times larger than the expected final emittance of the laser-cooled portion. An ion is defined as “laser-cooled” if it is inside the boundaries in all three-phase planes simultaneously. We have confirmed that this definition works well because the ultra cold portion of the beam is generally stable with the cooling laser on and has very small emittances in all directions (see Fig. 2.10). In order to evaluate the efficiency of laser cooling for each numerical simulation, we define the new parameter called the particle capture rate (PCR) that represents the number of cooled ions at final state divided by the number of ions in a bunch. After that we calculate the beam temperatures of three directions.

In the case of 2D cooling scheme, the vertical direction is independent of the other two directions unless imperfection fields and/or inter-particle Coulomb interactions play a noticeable role. Table 2.3 summarizes typical S-LSR parameters in the 2D cooling

mode. The artificial coupling strength between the longitudinal and horizontal degrees of freedom is determined by the magnitude of momentum dispersion at the rf cavity. According to the linear theory [17,18], there is a threshold value of dispersion above which the horizontal cooling efficiency is roughly maintained at the same high level as the longitudinal direct cooling efficiency. A simple theoretical estimate using transfer matrices suggests that the threshold dispersion is only about 0.1m under the lattice conditions in Table 2.3. The actual dispersion is 1.016 m, well above the theoretically demanded minimum value. For the optimization of Doppler laser cooling, the laser spot size and the laser detuning are the most important physical parameters. We have conducted systematic MD simulations with the parameters listed in Table 2.3. In the case of S-LSR where laser photons are co-propagating with the beam, Γ must be negative. Assuming $S \approx 1$ on axis, we have $\Delta \approx -\Gamma/2$, which gives −21MHz for $^{24}Mg^{+}$ ions. While this value of detuning guarantees the highest cooling efficiency for particles near the axis, the number of cooled ions could probably be improved with a larger detuning. We therefore focus our discussion here on four particular choices of detuning; namely, −21 MHz, −42 MHz, −63 MHz, and −84 MHz, which are integer multiples of $-\Gamma/2$. PCR also depends on the laser spot size in practice, so we change the laser spot size from 0.33mm to 6.0mm with 10mW total laser power. Note that in the recent cooling experiment at S-LSR [20], the detuning had been set, typically, at −200MHz to improve the PCR. The cooling laser was focused to $\sigma < 0.5$ mm, much smaller than the initial beam extent. For comparison, we did MD simulations assuming these actual parameters and obtained the possible final temperature of around 10K in the transverse directions and around 0.3K in the longitudinal direction. These numbers are in reasonable agreement with the experimental observation in Ref. [20].

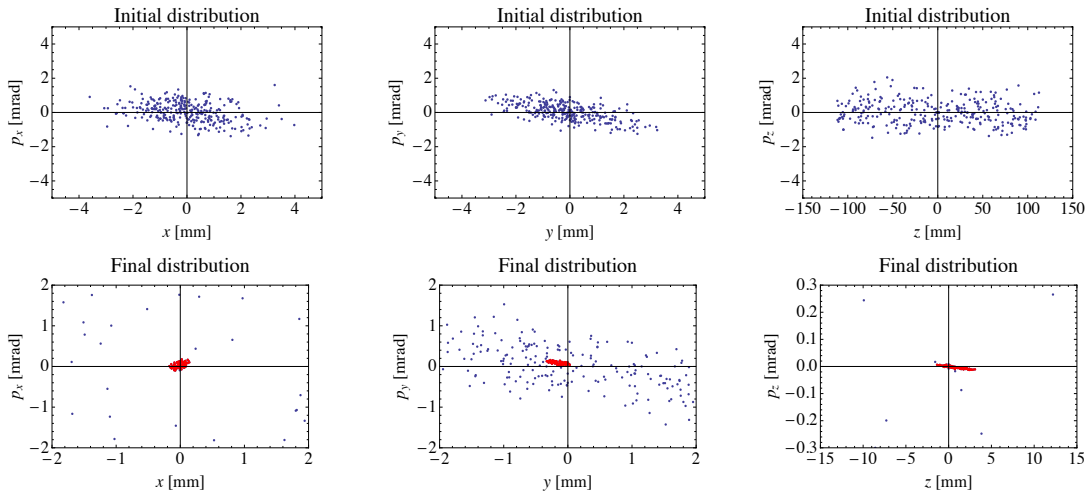

Fig. 2.10: The typical phase space distributions in the horizontal, the vertical, and the longitudinal direction. The initial distributions in the upper panels are changed to the lower ones within a few seconds after multi-dimensional laser cooling. Note that in the lower panels, only the vicinity of the central beam orbit is shown; there are many uncooled ions out of the ranges of the coordinates. We can easily separate the laser-cooled ions that are concentrated near the origin.

Table 2.3 Main parameters of two-dimensional cooling simulations

Ion numbers	300 / bunch
Turn number of simulation	125000 (5sec)
Betatron tunes (ν_x, ν_y)	(2.075, 1.120)
Synchrotron tune ν_z	0.075
Rf voltage	41.8 V
Dispersion function at the rf cavity	1.016 m
Phase slip factor	-0.6758
Solenoid field	OFF
Total laser power	10mW
Laser spot size	0.3 mm ~ 6.0 mm
Laser detuning	-21 MHz, -42 MHz, -63 MHz, -84MHz

PCR evaluated at 5 s after the start of each cooling procedure is plotted in Fig. 2.11 as a function of the laser spot size. Each line corresponds to the each laser detuning written in Fig. 2.11. The PCR become larger when we choose large laser detuning and the maximum value of the PCR are around 1.5 mm, which is somewhat smaller than the initial beam extent (see Fig. 2.11). Ideally, the spot size should be sufficiently greater than the transverse extent of an initial hot beam to cover all ions for cooling. Provided that the transverse beam extent is initially about 3mm in radius, as in the example of Fig. 2.11, the laser spot has to cover an area of 9π mm^2 within which the photon density should preferably be over the saturation level. We then need a total laser power well beyond 70mW to cool all hot ions efficiently because the saturation intensity for $^{24}Mg^+$ is 2.54mWmm^2. The total laser power available in S-LSR is, however, only 10mW, which means that too much expansion of the laser spot results in a considerable reduction of the photon density and thus seriously affects the cooling rate. This is why we have an optimum range of σ for the best cooling performance. Thanks to the betatron oscillations, even tail ions experience finite energy dissipation in the

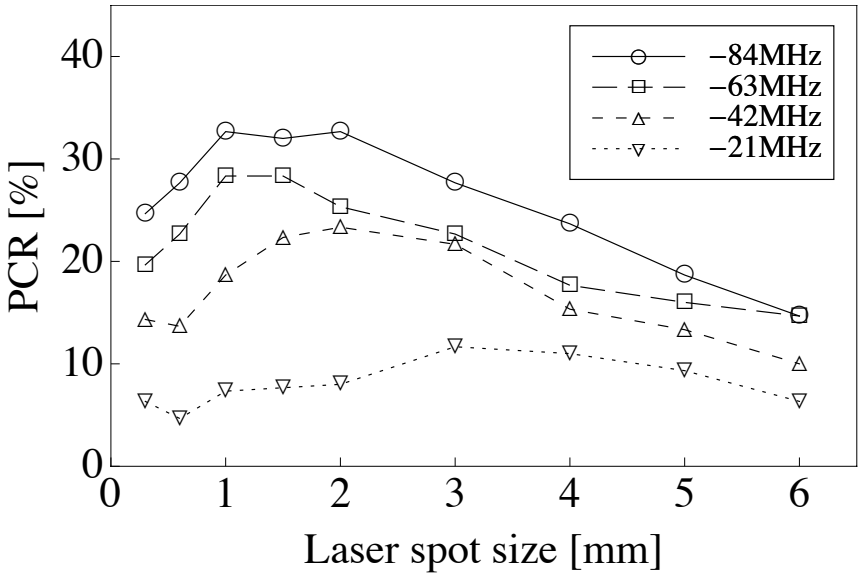

Fig. 2.11: The simulation results of the PCR at 5 sec in the case of 2D cooling. The total laser power is fixed at 10 mW and the laser spot size is changed from 0.3 mm to 6.0 mm. The four lines correspond to the laser detuning -21MHz, -42MHz, -63MHz, and -84MHz. These laser detuning represent $-\Gamma/2, -\Gamma, -3\Gamma/2,$ and -2Γ. The $-\Gamma$ is a natural line width of the $^{24}Mg^+$ ion.

longitudinal direction every few turns. The resonant coupling mechanism then creates a weak but finite cooling effect on the horizontal ion motion, leading to a gradual shrinkage of the beam size and consequently to a better overlap with the laser. The improved overlap between the beam and laser enhances PCR. Fig. 2.12 shows the time development of the PCR of the each 2D cooling simulation. PCR keeps rising at 10 sec owing to the betatron oscillation, even the particles moving with larger amplitudes than the laser spot size can be cooled by the co-propagating laser.

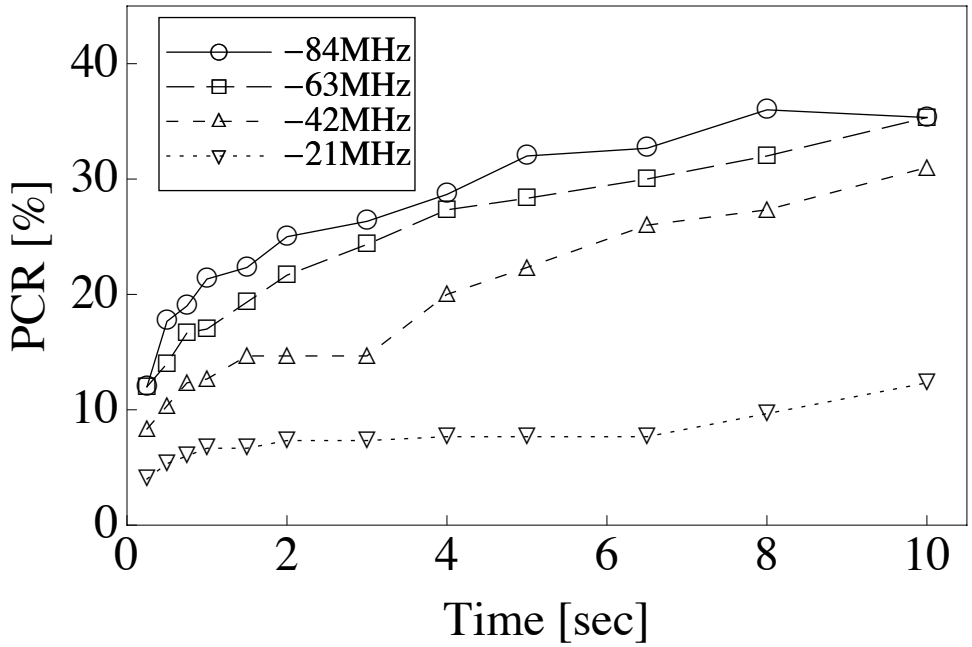

Fig. 2.12: The time evolution of PCR with applying laser cooling in the case of 2D cooling. The PCR increases still in 10sec. The laser spot size is fixed at 1.5 mm.

The following figures are the final temperatures of 2D cooling at 5sec taking account only cooled particles. The circle points represent the horizontal temperatures, the square points represent the vertical temperatures, and the triangle points represent the longitudinal temperatures. The four figures are corresponding to the different laser detuning. Final temperatures of the longitudinal direction are about a hundred times

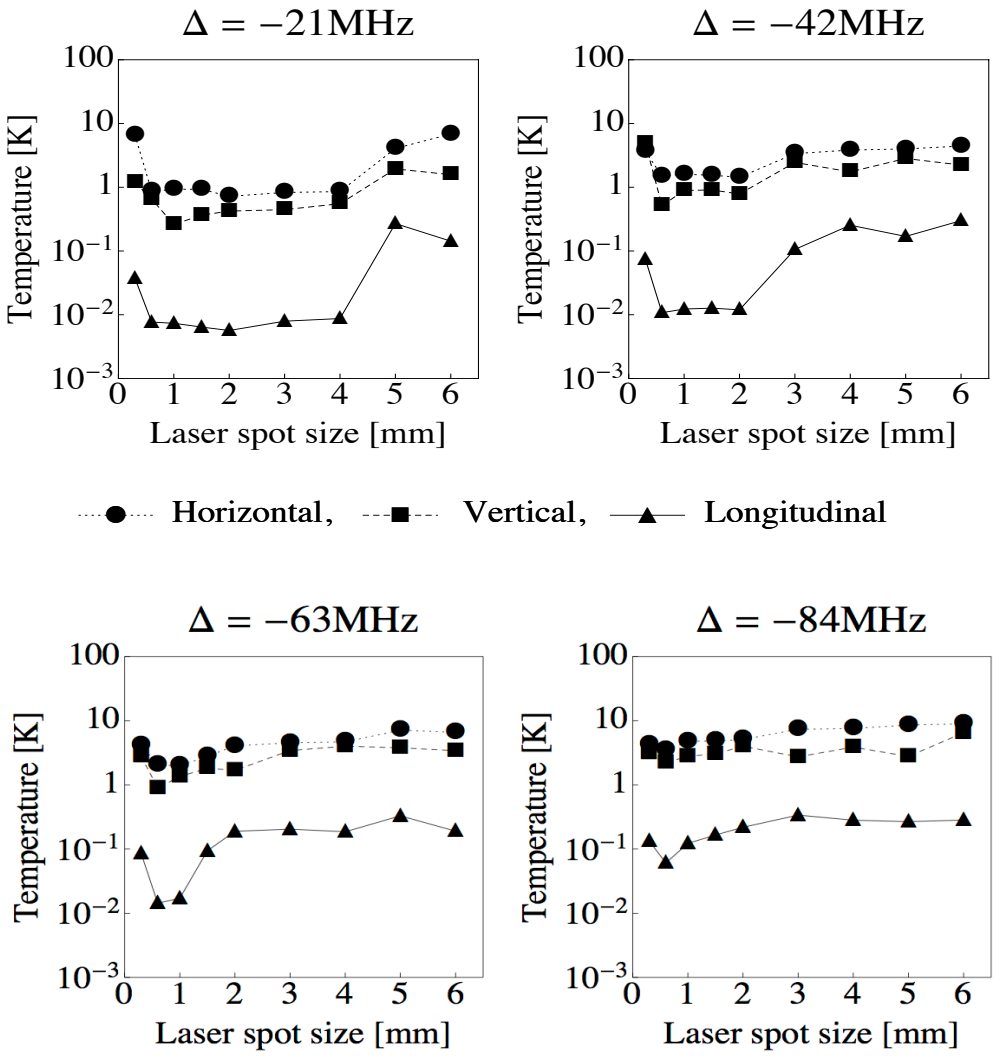

Fig. 2.13: Beam temperature reached in 5 s after injection by the use of the 2D resonant coupling scheme. These values of temperature are evaluated from laser-cooled ions concentrating near the design beam orbit. We have ignored the existence of many hot uncooled ions as observed in Fig. 2.10.

lower than the transverse direction. The apparent difference of final temperatures between the transverse and longitudinal direction caused from the experimental situation that the longitudinal direction cooled directly by Doppler laser cooling.

In addition we found the existence of laser spot regions where the longitudinal temperatures are about ten times lower compare to the other areas. The sharp drop of the equilibrium beam temperature in Fig. 2.13 is a signature of the so-called longitudinal beam ordering. Fig. 2.14 shows the single particle orbits of the ordering beam (left panel) and the non-ordering beam (right panel). In the case of an ordering beam, the synchrotron motions are suppressed due to the strong Coulomb potential. Fig. 2.15 shows the synchrotron tunes of each particle shown in Fig. 2.14 and we confirmed that tunes of the ordering beam are completely zero. The acceptable range for ordering becomes wider for a smaller $|\Delta|$. Contrarily, as already found in Fig. 2.13, PCR is worsened as $|\Delta|$ decreases. Considering these facts, we conclude that from a practical point of view, $|\Delta|$ should be set around Γor slightly higher in the 2D cooling mode at S-LSR. The detuning of -42MHz and the spot size of around 1.5mm appear to be the best combination to attain a reasonably high PCR as well as an ultralow beam temperature. A final temperature near 1K or less is then achievable in both transverse dimensions. The longitudinal temperature can be reduced to about 0.01 K, slightly above the Doppler limit. These temperatures are one order of magnitude lower than the recent experimental result at S-LSR [15].

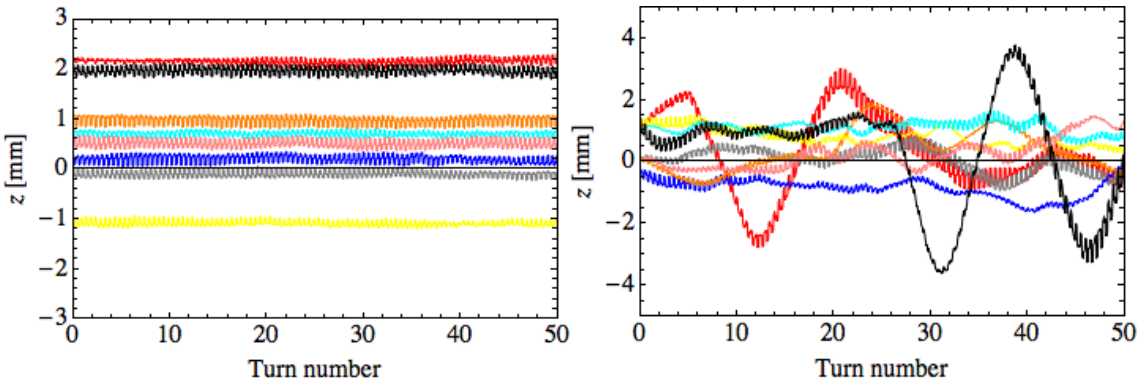

Fig. 2.14: The longitudinal orbits of cooled ions with the laser detuning -42 MHz. The left panel show the result of σ = 2.0 mm and the right panel is the case of σ = 3.0 mm. The synchrotron motions of an ordered beam are completely suppressed due to the Coulomb interaction of each cooled particle.

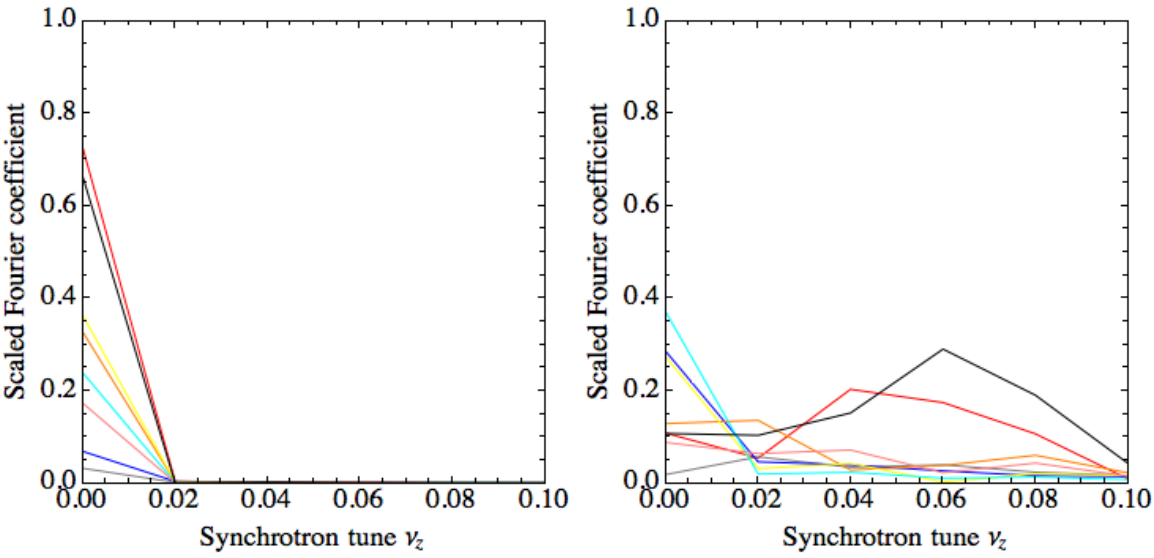

Fig. 2.15: The synchrotron tunes of each particle shown in Fig. 2.14. Tunes of the ordered state beam are depressed to zero due to the Coulomb interaction.

2.4.3 Three-dimensional cooling

We now switch on the solenoid magnet to provide a linear coupling between the horizontal and vertical directions. In general it is easier to make a high quality beam by 3D cooling mode than 2D cooling mode due to the artificial coupling potential of transverse directions. To maximize the indirect laser-cooling rate in the vertical degree of freedom, we need both resonance conditions in Eq. (2.24) to be simultaneously satisfied. The lattice parameters assumed for three-dimensional (3D) cooling simulations are listed in Table 2.4. The fractional parts of the three tunes have been equalized to excite full 3D coupling resonances. The momentum dispersion at the rf cavity, indispensable for transverse cooling, is 1.025 m. Corresponding to this number, there is the optimum narrow range of the solenoid field strength for most efficient 3D cooling. From the transfer-matrix theory, obtain the cooling-rate diagram in Fig. 2.7. We see that the vertical cooling rate increases at the expense of the cooling rates of the other two directions as the solenoid field is strengthened. The cooling efficiency of the three directions can be made approximately equal when the field strength is about 65 Gauss. The dependence of PCR on the laser spot size at 5 sec is depicted in Fig. 2.16.

Table 2.4 Main parameters of three-dimensional cooling simulations

Kinetic energy	40kev
Ion numbers	300 / bunch
Turn number of simulation	125000 (5sec)
Betatron tunes (ν_x, ν_y)	(2.070, 1.070)
Synchrotron tune ν_z	0.070
Rf voltage	36.2 V
Dispersion function at the rf cavity	1.025 m
Phase slip factor	-0.6762
Solenoid field	65.0Gauss
Total laser power	10mW
Laser spot size	0.3 mm ~ 6.0 mm
Laser detuning	-21 MHz, -42 MHz, -63 MHz, -84MHz

We confirm the spot-size dependence similar to that in the 2D cooling case; PCR is maximized with the spot size around 1.5 mm. Compared to the result in Fig. 2.11, PCR has become slightly better in the 3D cooling operation. A preferable effect from the indirect vertical cooling is also visible in Fig. 2.17, which shows the beam temperature reached 5 s after the start of laser cooling. The spot-size range where we can expect the occurrence of the longitudinal beam ordering has clearly been widened. The results in Fig. 2.17 together with those in Fig. 2.16 suggest that the detuning should be chosen between $-3\Gamma/2$ and $-\Gamma$. A larger value of $|\Delta|$ guarantees more efficient capture of ions but makes the tolerable range of the laser spot size narrower. We thus come to the same conclusion as made for the 2D cooling mode; namely, σ and $|\Delta|$ should be set to $\sim$1.5mm and $\sim$42MHz (or somewhat higher) to generate the coldest beam in S-LSR. The possible transverse and longitudinal temperatures we can reach with these parameters are roughly 1K and 0.01 K, respectively.

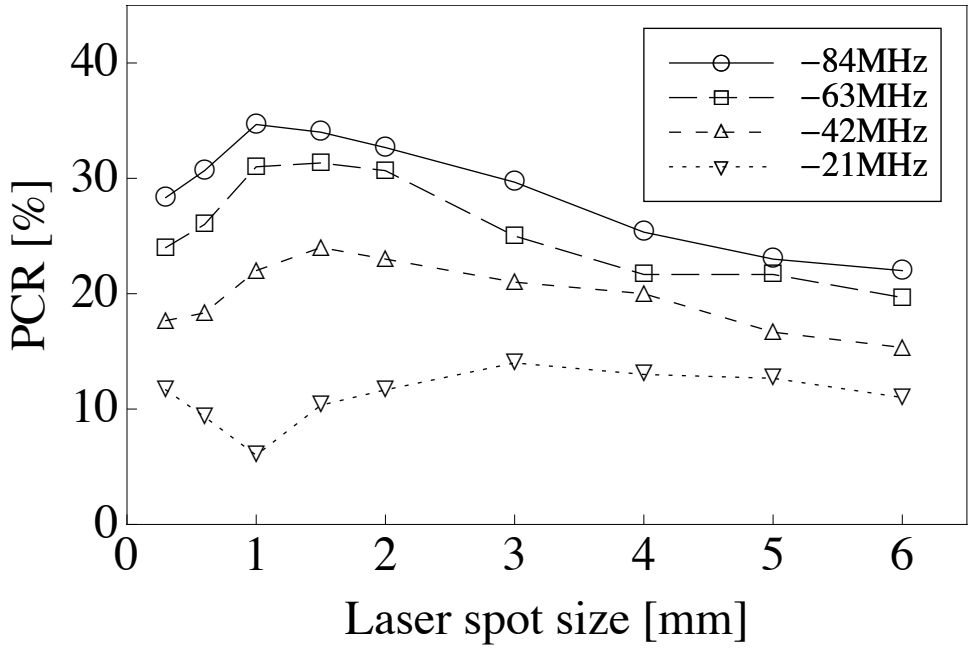

Fig. 2.16: PCR after 5 s of 3D laser cooling at S-LSR vs. laser spot size σ at the center of the cooling straight section. Similarly to the 2D cooling simulations in Fig. 2.11, we have taken four different values of laser detuning into consideration. The lattice parameters assumed here are listed in Table 2.4 .

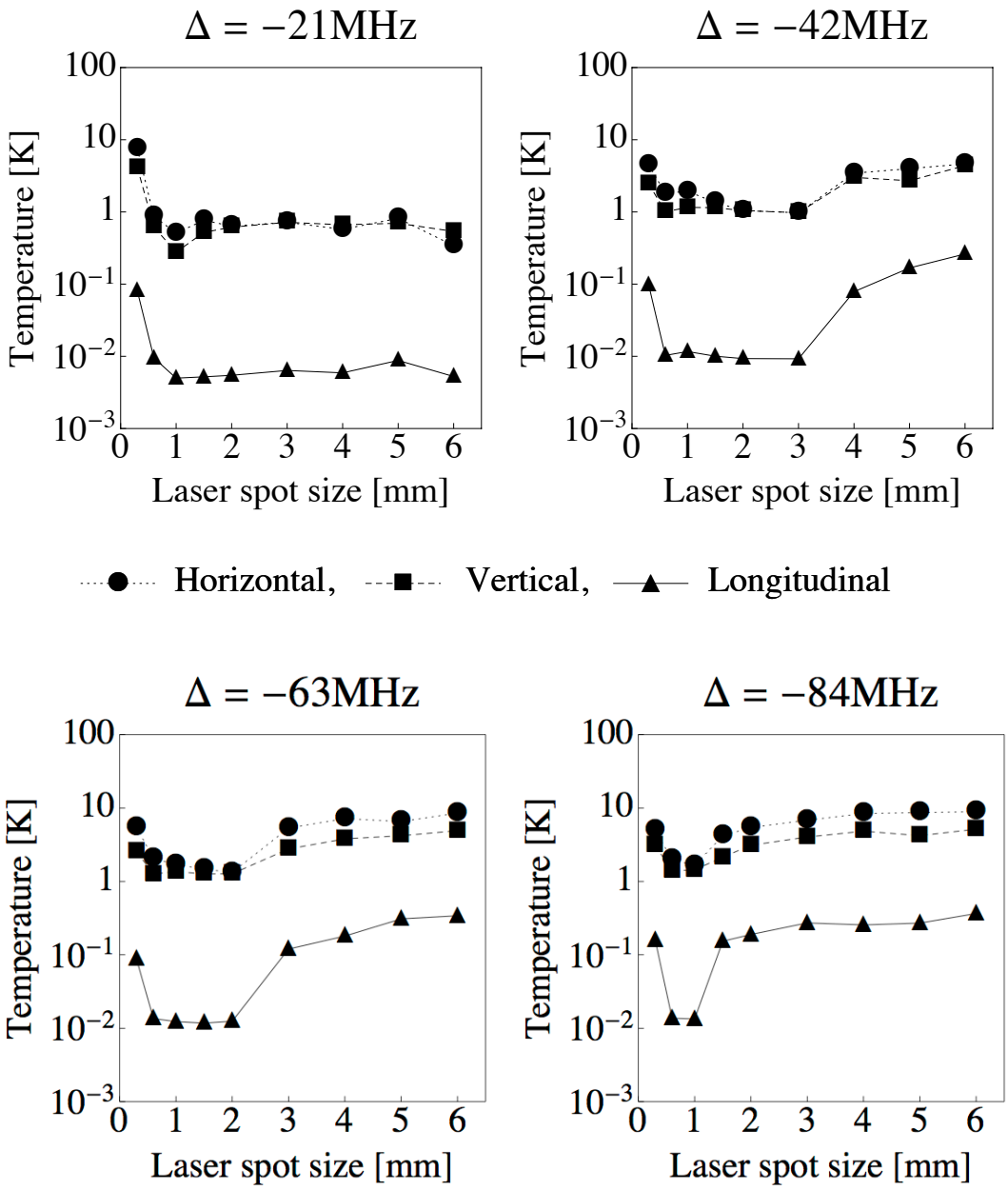

Fig. 2.17: Beam temperature reached in 5 s after injection by the use of the 3D resonant coupling scheme. Similarly to the result in Fig. 2.13, only laser-cooled ions are picked out to evaluate the temperature.

2.4.4 Radio-frequency field ramping for string crystal formation

In the previous section, we revealed that that with proper choices of experimental parameters, we are able to generate a high-quality beam in S-LSR even with a single low power laser. The beam we obtained in MD simulations is so-called ordered state beam and that is extremely low temperature compare to any other beams around the world. However in order to produce a crystalline beam, we have to make a progress. In this section, we make one more step forward to a Coulomb crystalline state. According to a previous MD study assuming two counter-propagating powerful lasers [64], a string-crystal-like structure could be formed in the S-LSR lattice by means of the RCM if the number of ions per bunch is limited to less than 10. Here we considerably increase the ion number and yet show that a long string beam could be attained even with a single low-power laser.

In order to generate a crystalline beam with finite transverse spatial extent, the longitudinal cooling force has to be properly tapered to compensate for the shear force induced by bending magnets [47, 60]. It is also crucial to maintain strict lattice symmetry to prevent transverse coherent instability [65]. Since these requirements are very difficult to meet in practice, the only realistic target we can aim at in S-LSR is the formation of a 1D string crystal. There is the critical line density at which the structural transition from a certain crystalline configuration to another takes place [46]. Needless to say, the threshold line density of the string-to-zigzag transition is the lowest. We thus have to keep the beam line density below a certain level so that the corresponding crystalline configuration, if formed, is a string. The Hasse-Schiffer theory for coasting crystalline beams predicts that the string-to-zigzag transition occurs at a line density of the order of $10^4 m^{-1}$ under the lattice conditions in Table 2.4 [46]. The transition density in the present case must be much lower than this theoretical estimate because the beam is not coasting but bunched by a rather strong rf field. In fact, the bunched string shown in Ref. [64] converts into a zigzag-like configuration if we add only a few more particles. Even if we keep the ion number in a bunch below 10, it is possible to transform the string configuration into a zigzag just by raising the synchrotron tune (or, in other words, by more strongly compressing the beam in the axial direction). In Appendix A, a numerical estimation is made of the number of stored ions with which the formation of an ideal bunched crystalline state is expected in S-LSR.

The simplest method to produce a long string crystalline beam with many ions is weakening the rf field in the cavity. The synchrotron tune then decreases (with the harmonic number fixed), which gives rise to the breakdown of the coupling resonance condition and to the lack of the indirect transverse cooling force. We could, however, rely on the sympathetic effect from Coulomb interactions once the beam is cooled down to an ultralow temperature range. As verified in Fig. 2.13, the sympathetic cooling mechanism can be effective even at low line density if the beam is already cold. We therefore first employ the RCM to strongly cool a low-current beam in S-LSR and, after that, gradually reduce the amplitude of the rf bunching field with the cooling laser on. This process achieves the required bunch lengthening and the maintenance of a three-dimensionally cold state simultaneously. In the following MD simulations, we start from the cold beam that has already been laser-cooled for 5 s in S-LSR under the lattice conditions in Table 2.5. The initial ion distribution is more or less like the one shown in the lower three panels of Fig. 2.10. Recalling the conclusion in the last section, we set the laser detuning and spot size, respectively, at −42MHz and 1.5 mm. Since the PCR after 5 s cooling is 24% with these parameters (see Fig. 2.16), there are 72 cold ions and 228 hot ions in a bunch at the beginning. The number of the initial cold ions can readily be controlled by changing the original beam intensity at injection.

The amplitude of the rf voltage, whose initial value is 36.2V for the synchrotron tune of 0.07, is linearly ramped to a specific final value V_f within the 12500 turns that corresponds to 0.5 s. We then maintain the rf voltage at V_f for the next 0.5 s, keeping the cooling laser on. In the rf ramping process, the hot tail ions oscillating about the design orbit may affect the motions of the cold laser-cooled ions, especially when V_f is low. Such an unfavorable source of heating can be removed effectively with the scrapers installed in S-LSR (see Fig. 2.9). Those scrapers have actually been used to reduce the beam intensity at injection and also to measure the transverse beam profiles. We here move both horizontal and vertical scrapers toward the central beam orbit in the first 12500 turns. At the beginning, the scrapers' edges are located 5mm away from the beam line, which eventually comes to 0.5mm in 0.5 s.

Table 2.5 Main parameters of rf ramping simulations

Ion species	$^{24}Mg^{+}$
Kinetic energy	40kev
Ion numbers	300 / bunch
Betatron tunes (ν_x, ν_y)	(2.070, 1.070)
Initial synchrotron tune ν_z	0.070
Initial rf voltage	36.2 V
Final rf voltage	1 V ~ 30 V
Solenoid field	65.0Gauss
Total laser power	10mW
Laser spot size	1.5 mm
Laser detuning	-42 MHz
Rf ramping start	5.0 sec
Rf ramping stop	5.5 sec
Laser cooling stop	6.0 sec

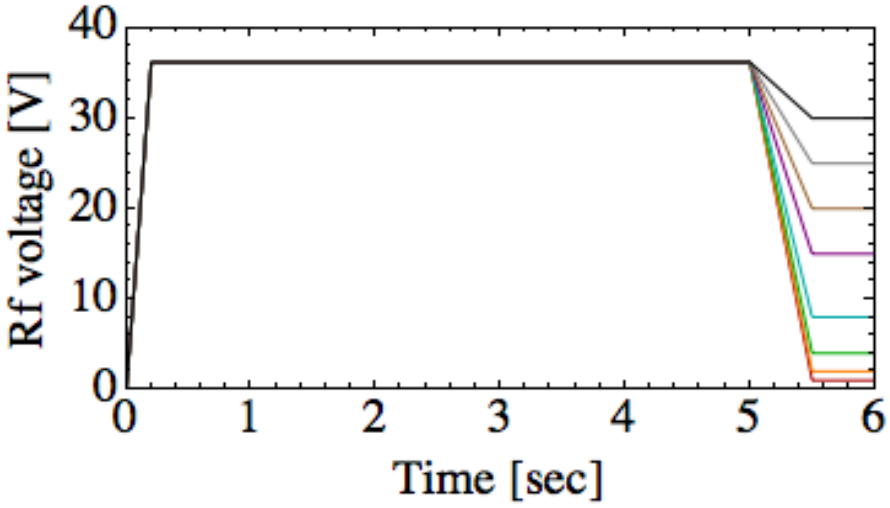

Fig. 2.18: The time evolution of the rf voltage in the cavity. Start ramping the rf field from 5 sec and stop at 5.5 sec. After that keep cooling the beam until 6.0 sec. We change the final voltage of rf field from 1 V to 30 V to find the optimum beam cooling parameter.

The final beam temperature after the rf ramping procedure is plotted in Fig. 2.19 as a function of V_f. Each bunch contains 72 cold ions initially (but a few hot ions are eventually cooled before being scraped and join the ultracold beam core). As expected, the beam temperature can be reduced further by carefully expanding the bunch. The final temperatures reachable with the rf ramping are near 0.1K in the transverse directions and 0.001K in the longitudinal direction. These numbers correspond to the normalized rms emttances around the order of 10^{-12} m and below 10^{-13} m, respectively. After a sort of equilibrium state is reached within 1 s, we ramp the laser power toward zero in 0.2 s, and then wait for another 0.4 s (10000 turns) to check if the beam is stable without the cooling force. Two examples are given in Fig. 2.20 which shows the spatial configurations of ultra-cold beams 0.4 s after the cooling laser is switched off. In the upper example, there are 37 ions forming the string configuration while in the lower example, the ion number is increased to 78. In both cases, V_f is set at 2V. We confirm that the string order of ions is well maintained for many turns around the ring even without the cooling force.

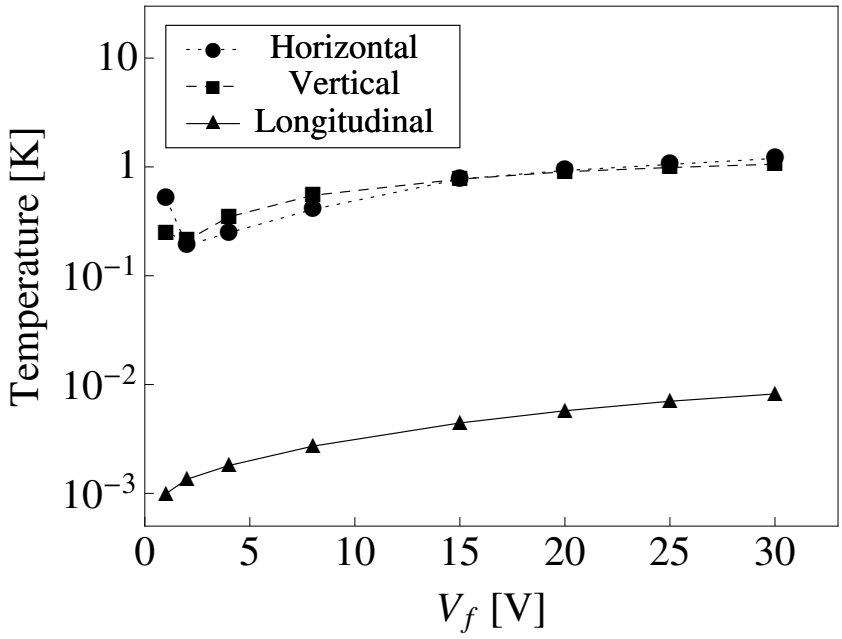

Fig. 2.19: Final beam temperature after the rf ramping procedure. The detuning and the spot size of the cooling laser are fixed, respectively, at − 42MHz and 1.5 mm. The total number of laser-cooled particles in the ring is around 7.5×10^3 in each simulation.

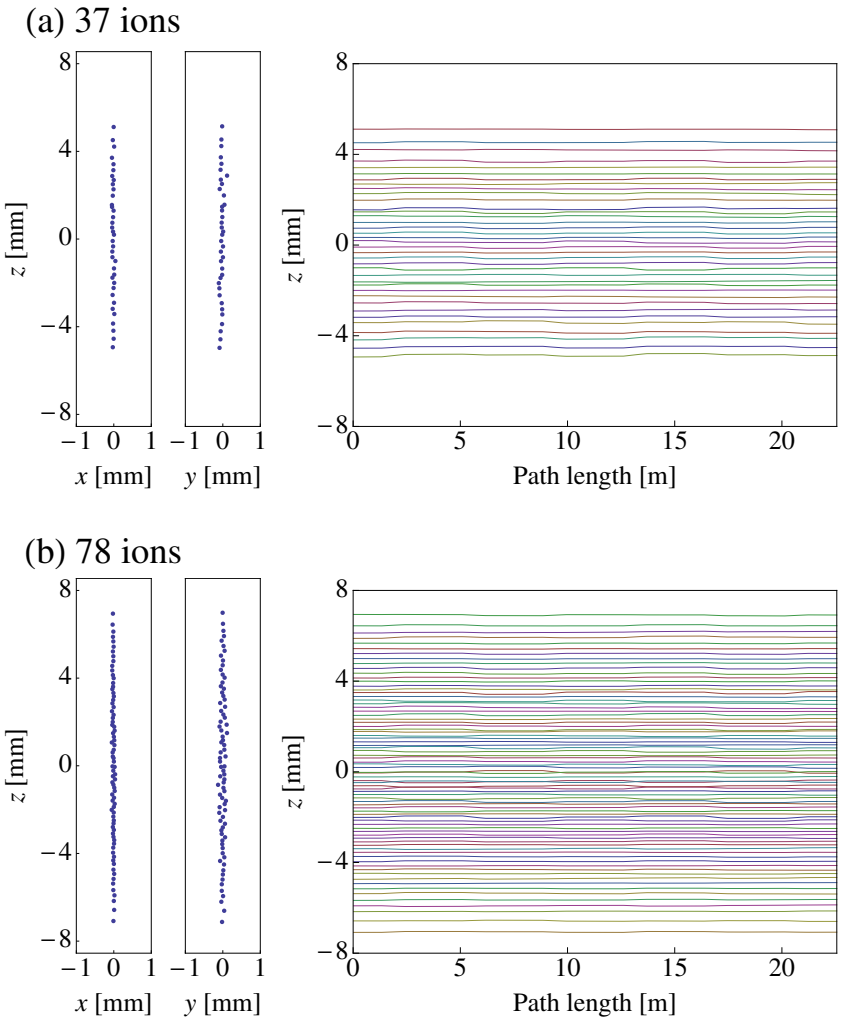

Fig. 2.20: Spatial configurations of laser-cooled beams after the rf ramping and the subsequent laser-power ramping procedures are completed. The two panels on the left side show the top and side views of an ultracold beam consisting of (a) 37 ions or (b) 78 ions, after 10000 turns around S-LSR without the laser cooling force. The axial position of each individual ion within the last turn is plotted on the right panel as a function of the path length along the design orbit. The final voltage V_f after the rf ramping is 2V in both examples. We see that the synchrotron motion is almost completely suppressed in both cases.

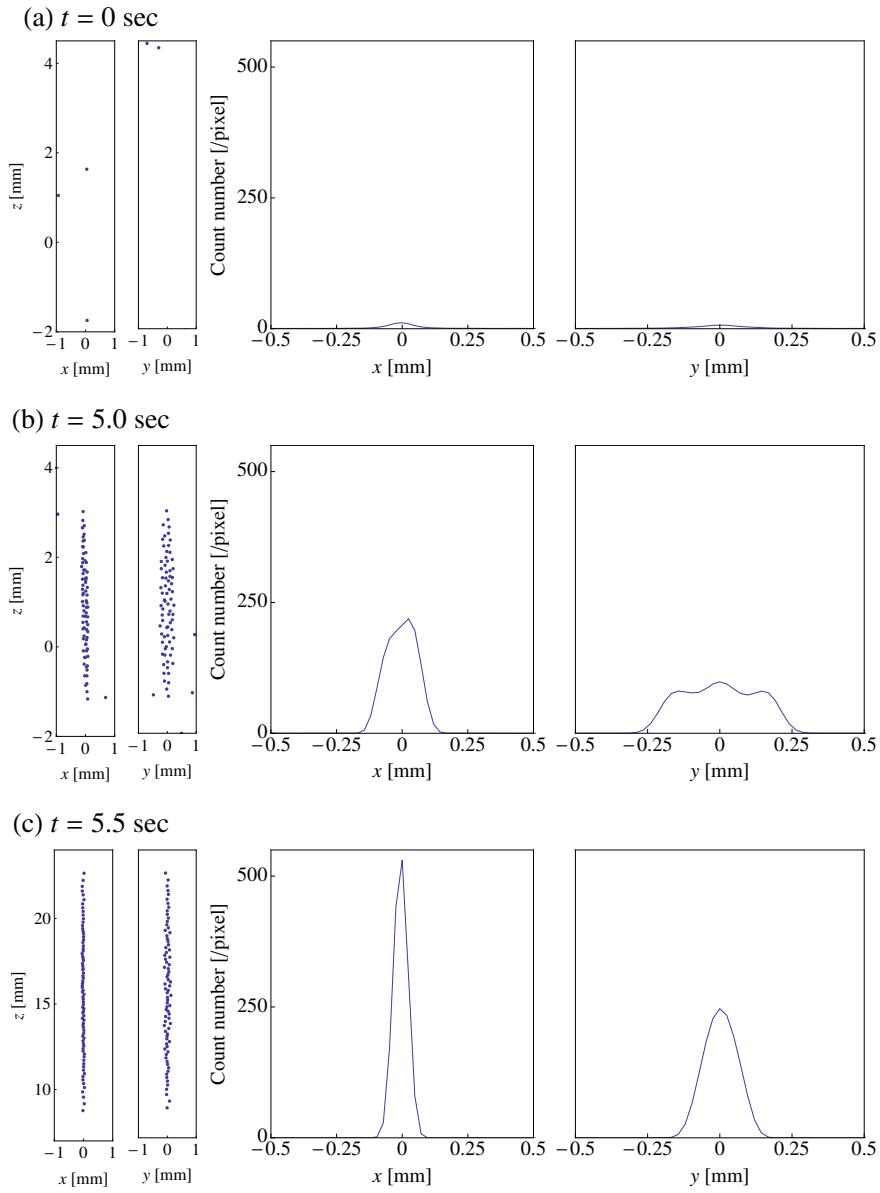

Fig. 2.21: The left panels are the spatial configuration of the laser cooled ions and right panels show the calculation results of LIF measurement in S-LSR. Same parameters of the CCD camera and 3D cooling mode with the optimum parameters are supposed. The upper, middle, and lower panels show the expected images (a) at the beam injection into the ring, (b) after the laser cooling for 5 s, and (c) after the completion of the rf ramping procedure. The exposure time of the camera is set at 0.1 s. Note that the centroid of the laser-cooled beam is axially shifted from the longitudinal origin (the center of the rf bucket) due to the radiation pressure by the co-propagation laser light. By gradually reducing the laser power to zero, the centroid position finally comes to the bucket center, as shown in Fig. 2.20.

In the laser cooling experiment in S-LSR, the LIF measurement by the CCD camera is used to measure the beam size of ions moving in S-LSR. We are able to do a similar calculation from the simulation result using a parameter of the CCD camera used in the experiment in S-LSR. This calculation helps us to evaluate the number of cooled ions in a bunch and obtain the information of the longitudinal temperature. Because in the case of the laser cooling experiment with small ion numbers per a bunch (less than 10^3 per a bunch), it is difficult technically to evaluate the longitudinal temperature in the experiment. Therefore we can obtain the valuable information from the LIF calculation using the distribution of MD simulations. We can confirm the calculation result in Fig. 2.21. The parameter of a LIF measurement and CCD camera equipped in S-LSR is shown in Table 2.6. We suppose the expose time of the CCD camera as 0.1 sec here and it is enough time to accumulate a count number of the camera that we can observe in the actual experiment in S-LSR. Fig. 2.21 shows calculation results of a LIF measurement from the distributions of a MD simulation. We use the simulation result of 3D cooling mode with the optimum parameters. The laser spot size is 1.5 mm, the laser detuning is -42MHz, and the final voltage of the cavity is $V_f = 2$ V. The upper panel shows the result of a LIF measurement from 0 sec to 0.1 sec, the middle panel show the result from 5.0 sec to 5.1 sec, and the lower panel shows the result from 5.5 sec to 5.6 sec. From the result, we confirm that the count number increase after the rf-field ramping.

Table 2.6 Parameters of LIF measurement and CCD camera in S-LSR

Window position from the beam line	14 cm
Diameter of the lenses	2.54 cm
Gain of the camera	1200
Quantum efficiency of the camera	15 %
System gain of the camera	4 electrons / count
Expose time of the camera	0.1 sec

2.5 Summary

We have performed systematic MD simulations assuming the actual hardware conditions for Doppler laser cooling of a 40 keV $^{24}Mg^{+}$ ion beam in S-LSR. Each simulation typically starts with 300 ions per bunch. This corresponds to 3×10^{4} stored ions in the ring, which is on the same order of the total ion number in recent cooling experiments [15]. The numerical data have been used to figure out the optimum cooling parameters with which the ultralow-temperature state of ions can be reached in this particular storage ring. In the past experiments done at S-LSR [51, 15], the laser detuning had been chosen mostly near -200 MHz to ensure a high PCR. The spot size was set at either around 1.4 mm [51] or 0.47 mm [15]. In these conditions, traverse temperature decrease to 20 K in horizontal and to 29 K in vertical. The simulation results in same condition show that temperature decrease to 9.6 K in horizontal and to 6.4 K in vertical. Compare to the experimental results, final temperatures are a little higher, but simulations suppose ideal situations, for example ignore the nonlinear fields or alignment errors of magnets, so results are reasonable. The present MD study has pointed out that such parameter choices are in appropriate for utilizing the full potential of the current Doppler cooling system. The simulation results indicate that the detuning and spot size of the cooling laser should be chosen, respectively, around -42 MHz and 1.5 mm. Then, the use of the RCM makes it possible for us to reach beam-temperature ranges of about 1 K in both transverse dimensions and on the order of 0.01 K in the longitudinal dimension. These numbers are one order of magnitude lower than the recent experimental achievement reported in Ref. [15]. We have also demonstrated that a linearly ordered state of ultra-cold ions, the so-called string state, can be established at low line density by gradually ramping the longitudinal rf field after 3D laser cooling. It is possible to form a long, bunched string beam consisting of nearly 80 ions if the rf voltage is lowered to around 2 V (corresponding to the synchrotron tune of 0.016 for a 40 keV $^{24}Mg^{+}$ ion). During the rf ramping, both transverse and longitudinal equilibrium temperatures are even more reduced to near 0.1 K and the Doppler limit, respectively. The string state is stable and lasts for more than 10,000 turns with no serious heating.

Finally, it is interesting to ask whether we can conclude the formation of the string state in S-LSR from actual experimental data. According to Eq. (2.11), each $^{24}Mg^{+}$ ion traveling in the cooling straight section at the kinetic energy of 40 keV scatters a photon

every few centimeters along the beam line provided $S \approx 1$ and $|\Delta| \approx \Gamma$. At the center of the cooling section, there is a small window located 14 cm away from the beam line [51]. Fluorescence photons passing through the window are eventually focused onto the CCD image sensor whose diameter is 2.54 cm. Considering that a hundred bunches are stored in S-LSR at the revolution frequency of 25 kHz, the sensor will receive over 10^5 photons per second from the ordered beam in Fig. 2.20. Since these photons come only from the vicinity of the design beam line, we expect a clear fluorescence image of the beam to be caught by the camera. Fig. 2.21 shows an example of possible transverse beam images estimated from MD simulation data. The exposure time of the CCD camera has been assumed to be 0.1 sec. Right after the beam injection (t = 0 sec), the fluorescence signal looks so weak that it will probably be hidden behind background noise. In fact, no clear signals have been detected in past cooling experiments when the initial number of stored ions is below the order of 10^4. After 3D laser cooling (t = 5 sec) under the optimum condition, the beam signal is enhanced by an order of magnitude. The signal becomes even sharper in both transverse directions after the rf ramping is completed. The peak level of the signal is much higher than the possible noise level in S-LSR. This numerical result suggests the following: after the initial beam scraping to $\sim 3\times10^4$ stored ions, we lose the uorescence signal or only have a very faint beam image. The signal will, however, be recovered during the most efficient 3D laser cooling. We will observe a sharp fluorescence peak suddenly rising on the beam line if the predicted, linearly ordered configuration is successfully formed.

3 Emittance growth estimation in intense mismatched beams

3.1 Reiser's free energy model

A beam emittance correspond to a beam quality, therefore we must pay attention to the physical phenomenon related to the emittance growth. In accrual accelerators, several elements, such as nonlinear potentials, installation errors of focusing magnets, and initial beam mismatches for beam transport systems, cause the emittance growth [5,66,67]. Especially accelerators those need a low-emittance and a high density beam, the precise beam matching is inevitable to prevent a generation of low-density tail of charged particles around the beam core, this is so-called *beam halo*. Beam halos are troublesome particularly in the case of high-energy accelerators, so the mechanics of generating a beam halo have been studied for long time [5, 68-72, 56, 73-85].

The self-consistent treatment of such a collective effect is extremely difficult. Since the basic equations of motion are too complex to solve mathematically, we try numerical approaches in many cases. Particle-in-cell (PIC) codes are often employed for this purpose, but high-precision PIC simulations are quite time-consuming. In particular, extremely long CPU time is required to simulate the collective behavior of an intense long bunch containing a huge number of particles. It is thus useful in practice to have any mathematical formula that enables us to make a quick estimate of emittance growth expected in a space-charge-dominated beam under a certain non-ideal condition. For the better understanding of the relation between an initially non-static beam and the emittance growth of the beam quantitatively, Reiser had constructed the theory that enable us to estimate an emittance growth of an initially-mismatched-coasting beam. We will explain his theory briefly below.

To simplify the dynamical system, we suppose a uniform-focused-coasting beam that satisfies the following condition.

$$\begin{aligned} \text{If } r < a, \quad & u(r) = N/\pi a^2 , \\ \text{If } a < r, \quad & u(r) = 0 . \end{aligned} \tag{3.1}$$

a is an edge radius of a beam. The distribution defined (3.1) is similar to a high intensity beam. The spatial particle distribution of a high intensity beam is homogenized due to the natural Debye screening effect. The Hamiltonian of a uniformly populated coasting beam can be represented as

$$H = \frac{1}{2}\left({p_x}^2 + {p_y}^2\right) + \frac{1}{2}{k_\perp}^2 r^2 + \left({k_\perp}^2 - f(r){k_\perp}^2\right)a^2 \log\frac{r_{ref}}{a} \qquad (3.2)$$

$$+ \frac{\left({k_\perp}^2 - f(r){k_\perp}^2\right)}{2}(a^2 - r^2).$$

In Eq. (3.2), we ignore effects of the motion in the longitudinal direction, because the dynamics of the longitudinal direction has no contribution to the dynamics system. $k_\perp$ is the tune of the transverse direction, r is the amplitude of a beam orbit, $r_{reference}$ is a reference point of the Coulomb potential and $f(r)$ is the function defined as the following formula.

$$f(r) = 1 - \frac{N}{2\varepsilon_0 \pi r^2 {k_\perp}^2}, \qquad (3.3)$$

where ε_0 is the vacuum permittivity and N is the number of particles in a unit length of the longitudinal degree of freedom. In the case of a matched beam, Eq. (3.4) is derived.

$$\eta_\perp = \sqrt{f(a_0)}, \qquad (3.4)$$

$\eta_\perp$ is so-called a tune depression of the transverse direction that represents the space charge strength of a beam. From the Hamiltonian (3.2), the total average energy per a particle can be expressed as

$$W = \frac{1}{4}{k_\perp}^2 a^2 + \frac{1}{4}f(a){k_\perp}^2 a^2 + \frac{1}{8}\left({k_\perp}^2 - f(a){k_\perp}^2\right)a^2\left(1 + 4\log\frac{r_{ref}}{a}\right). \qquad (3.5)$$

W includes the kinetic energy, the potential energy of the external focusing field, and the potential energy of the Coulomb self-field, is conserved in this closed system. The total average energy should be minimum when a beam is in a perfectly matched state. M.Reiser assumes that due to the excess energy of a mismatched beam, the emittance growth would be occurred.

Let us derive the excess energy of a transversely mismatched beam. Suppose both a mismatched and a perfectly matched beam (subscript 0) in transverse phase space. An initially mismatched beam should be settled into the final stationary state a little later.

And we define that with subscript f. The excess energy of a mismatched beam can be derived as follows.

$$\begin{aligned}\Delta W = W_f - W_0 = &\frac{1}{4}{k_\perp}^2{a_f}^2 + \frac{1}{4}f(a_f){k_\perp}^2{a_f}^2 \\ &+ \frac{1}{8}\left({k_\perp}^2 - f(a_f){k_\perp}^2\right){a_f}^2\left(1 + 4\log\frac{r_{ref}}{a_f}\right) - \frac{1}{4}{k_\perp}^2{a_0}^2 \\ &- \frac{1}{4}f(a_0){k_\perp}^2{a_0}^2 - \frac{1}{8}\left({k_\perp}^2 - f(a_0){k_\perp}^2\right){a_0}^2\left(1 + 4\log\frac{r_{ref}}{a_0}\right) \\ &= \frac{1}{2}{k_\perp}^2{a_0}^2 w.\end{aligned} \tag{3.6}$$

w is called free-energy parameter and defined as

$$w = \left(\frac{a_f}{a_0}\right)^2 - 1 - (1 - f(a_0))\ln\frac{a_f}{a_0}. \tag{3.7}$$

As a result we obtained the relational expression of a_0 and a_f.

$$\frac{a_f}{a_0} = 1 + \frac{w}{1 + {\eta_\perp}^2} \tag{3.8}$$

Eq. (3.9) is the free energy and the free-energy parameter of the initially mismatched beam (subscript i) can be obtained with same procedure of Eqs. (3.7) and (3.8).

$$\begin{aligned}\Delta W = W_i - W_0 = &\frac{1}{4}{k_\perp}^2{a_0}^2 + \frac{1}{4{\xi_\perp}^2}f(\xi_\perp a_0){k_\perp}^2{a_0}^2 \\ &+ \frac{1}{8}\left({k_\perp}^2 - f(\xi_\perp a_0){k_\perp}^2\right){\xi_\perp}^2{a_0}^2\left(1 + 4\log\frac{r_{ref}}{\xi_\perp a_0}\right) - \frac{1}{4}{k_\perp}^2{a_0}^2 - \frac{1}{4}f(a_0){k_\perp}^2{a_0}^2 \\ &- \frac{1}{8}\left({k_\perp}^2 - f(a_0){k_\perp}^2\right){a_0}^2\left(1 + 4\log\frac{r_{ref}}{a_0}\right) = \frac{1}{2}{k_\perp}^2{a_0}^2 w.\end{aligned} \tag{3.9}$$

$$w = \frac{1}{2}{\eta_\perp}^2\left(\frac{1}{{\xi_\perp}^2} - 1\right) + \frac{1}{2}\left({\xi_\perp}^2 - 1\right) + (1 - {\eta_\perp}^2)\ln\frac{1}{\xi_\perp}, \tag{3.10}$$

where $\xi_\perp$ is called a mismatch factor defined as $a_i = \xi_\perp a_0$. We assumed that the mismatched beam initially has the same rms emittance as the matched beam. The emittance ratio between the final state of a mismatched and a perfectly matched beam is given as the following formula.

$$\frac{\epsilon_{\perp f}}{\epsilon_{\perp 0}} = \frac{a_f}{a_0}\sqrt{1+\frac{1}{{\eta_\perp}^2}({\xi_\perp}^2-1)}\,. \tag{3.11}$$

where $\epsilon_\perp$ is a transverse rms emittance. From Eqs. (3.9) – (3.11), we found that if we know a tune depression and an initial mismatch factor of a beam, the emittance growth of an initially mismatched beam can be calculated. This is the abstract of Reiser's free-energy model [22].

3.2 Free energy model for a bunched beam

In the previous section, we briefly confirmed the abstract of Reiser's free energy model for round coasting beams with a uniform-continues focusing. Thanks to his theory, we are able to estimate the emittance growth of an initially mismatched coasting beam easily. But for real, most accelerators operated with bunched beams, therefore we try to generalize his theory to an intense bunched beam with continues linear focusing in the three degrees of freedom. We suppose rotation symmetry in the transverse direction for simplicity. This approximation looks valid because a horizontal tune and a vertical tune have similar value for most accelerators. We will explain the detail of the generalized Reiser's theory below.

3.2.1 Free energy of an initially mismatched bunch

As is well known that an ellipsoidal bunched beam moving through a continues linear focusing system obeys the Hamiltonian

$$H = \frac{1}{2}\left({p_x}^2+{p_y}^2+{p_z}^2\right)+V_{\text{ext}}+\frac{2\pi\varepsilon_0 K_{sc}}{N_b q}U_{\text{C}}, \tag{3.12}$$

where V_{ext} is the external potential provided by beam-focusing magnets, U_{C} is the Coulomb self-field potential, q is the charge state of the particle, ε_0 is the vacuum permittivity, K_{sc} is the generalized beam perveance, and the independent variable is the path length s along the design beam orbit. For a beam traveling at a speed βc with c being the speed of light, the perveance is defined by $K_{sc} = 2N_b r_p/\beta^2\gamma^3$ where N_b is the number of particles in a bunch, r_p is the classical particle radius, and γ is the Lorentz

factor, i.e., $\gamma = 1/(1-\beta^2)^{1/2}$. Employing the smooth approximation, we can express V_{ext} as

$$V_{\text{ext}} = \frac{1}{2}\left[{k_x}^2 x^2 + {k_y}^2 y^2 + {k_\parallel}^2 z^2\right], \tag{3.13}$$

where $(k_x,\ k_y)$ and k_ determine the beam-focusing strengths on the transverse $x-y$ plane and in the longitudinal $z-$ direction. These focusing parameters are proportional to the phase advances or, in other words, the tunes at zero beam intensity. The harmonic oscillator model as in Eq. (3.13) has been frequently used in past theoretical studies of intense beam dynamics [33]. For an ellipsoidal bunch with rotational symmetry, we can put $k_x = k_y\ (\equiv k_\perp)$. At high beam intensity, the spatial particle distribution is homogenized due to the natural Debye screening effect. We thus assume that the charge density is approximately uniform within the ellipsoidal boundary, so beam distribution in the real space is defined as follows.

$$\text{If } \frac{(x^2+y^2)}{a^2} + \frac{z^2}{b^2} \le 1, \qquad u(x,y,z) = \frac{3N_b}{4\pi a^2 b} \equiv \rho, \tag{3.14}$$

$$\text{If } \frac{(x^2+y^2)}{a^2} + \frac{z^2}{b^2} > 1, \qquad u(x,y,z) = 0,$$

where a is the maximum transverse amplitude of a beam and b is the half bunch length of a beam. The corresponding Coulomb potential is given by

$$U_{\text{C}} = -\frac{\rho a^2 b}{4\varepsilon_0}\int_0^\infty \frac{1}{(a^2+\sigma)(b^2+\sigma)^{1/2}}\left(\frac{x^2+y^2}{(a^2+\sigma)} + \frac{z^2}{(b^2+\sigma)}\right)d\sigma. \tag{3.15}$$

Substituting Eqs. (3.15) and (3.17) into (3.13), we obtain

$$H = \frac{1}{2}\left({p_x}^2 + {p_y}^2 + {p_z}^2\right) + \frac{1}{2}{k_\perp}^2 f_\perp(a,b)(x^2+y^2) + \frac{1}{2}{k_\parallel}^2 f_\parallel(a,b) z^2, \tag{3.16}$$

where

$$f_\perp(a,b) = 1 - \frac{3K_{sc}}{4{k_\perp}^2}\int_0^\infty \frac{d\sigma}{(a^2+\sigma)^2(b^2+\sigma)^{\frac{1}{2}}},$$
$$f_\parallel(a,b) = 1 - \frac{3K_{sc}}{4{k_\parallel}^2}\int_0^\infty \frac{d\sigma}{(a^2+\sigma)(b^2+\sigma)^{3/2}}. \tag{3.17}$$

We will derive second momentum equations those we need later. In the transverse x-direction the canonical equations of motion are derived from Hamiltonian

$$\frac{dx}{ds} = p_x, \qquad \frac{dp_x}{ds} = -{k_\perp}^2 f_\perp(a,b)x. \tag{3.18}$$

Provided that the particle distribution function obeys the Vlasov equation in phase space, the use of these canonical equations allows us to obtain

$$\frac{d^2 a_{\mathrm{rms}}}{ds^2} + {k_\perp}^2 f_\perp(a,b) a_{\mathrm{rms}} - \frac{{\epsilon_\perp}^2}{{a_{\mathrm{rms}}}^3} = 0, \tag{3.19.a}$$

where ε⊥ is the transverse rms emittance defined by $\epsilon_\perp = (a_{\mathrm{rms}}^2 \langle p_x^2 \rangle - \langle x p_x \rangle^2)^{1/2}$.Similar second moment equations hold for the other two directions. While a uniform particle density has been assumed here, the rms envelope equations are insensitive to the type of distribution function, as theoretically proven by Sacherer [42].

$$\frac{d^2 b_{\mathrm{rms}}}{ds^2} + {k_\parallel}^2 f_\parallel(a,b) b_{\mathrm{rms}} - \frac{{\epsilon_\parallel}^2}{{b_{\mathrm{rms}}}^3} = 0, \tag{3.19.b}$$

Ideally, an intense beam injected into an accelerator should be not only well matched to the machine lattice but also in thermal equilibrium (or, in other words, *equipartitioned* [86]). No emittance growth occurs in that case. The beam is perfectly stationary under the uniform restoring force generated by V_{ext}, so we write $a \equiv a_0 (= \mathrm{const})$ and $b \equiv b_0 (= \mathrm{const})$. A uniformly populated bunch, the rms envelope equations lead to

$$\epsilon_{\perp 0} = \frac{k_\perp \eta_\perp {a_0}^2}{5} \text{ and } \epsilon_{\parallel 0} = \frac{k_\parallel \eta_\parallel {b_0}^2}{5}, \tag{3.20}$$

where $\epsilon_{\perp 0}$ and $\epsilon_{\parallel 0}$ represent the transverse and longitudinal rms emittances of the matched beam, a_0 and b_0 is the maximum beam radius and half bunch length of a matched beam, and $\eta_\perp$ and $\eta_\parallel$ are the tune depression of the transverse and the longitudinal direction represented by $\eta_\perp = [f_\perp(a_0, b_0)]^{1/2}$ and $\eta_\parallel = [f_\parallel(a_0, b_0)]^{1/2}$. We use $a_{\mathrm{rms}} = a_0/\sqrt{5}$ and $b_{\mathrm{rms}} = b_0/\sqrt{5}$ when we derive Eq. (3.20). By definition, the tune depressions become unity at the low-beam-intensity limit, i.e. $K_{sc} \rightarrow 0$. As the beam density increases, both parameters approach zero.

Assuming the thermal equilibrium state for the matched beam, we obtain

$$\frac{\epsilon_{\parallel 0}}{\epsilon_{\perp 0}} = \frac{k_\perp \eta_\perp}{k_\parallel \eta_\parallel} = R_0, \tag{3.21}$$

where $R_0 \equiv b_0/a_0$ is the aspect ratio of the matched bunch. Under this condition, the tune depression factors can be written as

$$\eta_\perp{}^2 = 1 - Q_0 I_\perp(R_0) \text{ and } \eta_\parallel{}^2 = 1 - Q_0 \left(\frac{\eta_\parallel}{\eta_\perp}\right)^2 I_\parallel(R_0), \tag{3.22}$$

where $Q_0 = 3K_{\rm sc}/4(k_\perp a_0)^2 a_0$, $I_\perp(R_0)$, and $I_\parallel(R_0)$ are defined as

$$I_\perp(R_0) = \int_0^\infty \frac{d\sigma'}{(1+\sigma')^2\left(R_0{}^2 + \sigma'\right)^{1/2}}, \tag{3.23.a}$$

$$I_\parallel(R_0) = R_0{}^2 \int_0^\infty \frac{d\sigma'}{(1+\sigma')\left(R_0{}^2 + \sigma'\right)^{3/2}}. \tag{3.23.b}$$

According to Eq. (3.22) and (3.23) we found that the aspect ratio R_0 are uniquely determined for the equipartitioned bunch.

As we said in the previous section, if a bunch is perfectly matched to the external focusing potential, the total energy of the system takes the minimum value W_0. Unfortunately, it is impossible in any realistic cases to establish such a perfect stationary state at the beginning; the beam is more or less deviated from the ideal condition because of unavoidable artificial errors. The beam then possesses a greater energy W_i ($>W_0$) depending on the degree of the initial mismatch. The mismatched bunch cannot be stationary but starts to execute a complex collective motion. It is reasonable to expect that, after some relaxation period, the non-stationary beam will settle into a stationary state with final energy W_f [22]. The excess energy $\Delta W = W_f - W_0$ is, according to Reiser, consumed to increase the rms emittance. Since the energy conservation law requires $W_f = W_i$, the emittance growth rate is directly linked to how much free energy is produced at the beginning by a certain mismatch. The average total energy of the system per particle is the sum of the kinetic energy $E_{\rm k}$, the beam focusing potential $E_{\rm p}$, and the Coulomb self-field energy $E_{\rm c}$. In the case of an initially matched beam, the second-moment equations yield the simple relations $\langle p_x^2 \rangle = (k_\perp a_0)^2 f_\perp(a_0, b_0)/5$, etc. because everything is static; namely, all *s*-derivatives vanish. We then readily find

$$E_{\rm k} = \frac{1}{2}\left(\langle p_x{}^2\rangle + \langle p_y{}^2\rangle + \langle p_z{}^2\rangle\right) = \frac{1}{5}(k_\perp \eta_\perp a_0)^2 + \frac{1}{10}(k_\parallel \eta_\parallel b_0)^2. \tag{3.24}$$

On the other hand, $E_{\rm p}$ is given by

$$E_{\rm p} = \frac{1}{2}\left(k_\perp{}^2\langle x^2\rangle + k_\perp{}^2\langle y^2\rangle + k_\parallel{}^2\langle z^2\rangle\right) = \frac{1}{5}(k_\perp a_0)^2 + \frac{1}{10}(k_\parallel b_0)^2. \tag{3.25}$$

We also calculate the average of the potential energy of the Coulomb self-field $E_{\rm C}$ as

$$E_{\mathrm{C}} = \frac{3K_{\mathrm{sc}}}{16}\int_0^{\infty}\frac{d\sigma}{(a_0{}^2+\sigma)\left(b_0{}^2+\sigma\right)^{1/2}} - \frac{1}{10}(k_{\perp}a_0)^2(1-\eta_{\perp}{}^2) - \frac{1}{20}(k_{\parallel}b_0)^2(1-\eta_{\parallel}{}^2). \tag{3.26}$$

Hence, the minimum energy of the matched state can be calculated by

$$W_0 = \frac{1}{10}(k_{\perp}a_0)^2(1+3\eta_{\perp}{}^2). + \frac{1}{20}(k_{\parallel}b_0)^2(1+3\eta_{\parallel}{}^2) + \frac{3K_{\mathrm{sc}}}{16}\int_0^{\infty}\frac{d\sigma}{(a_0{}^2+\sigma)\left(b_0{}^2+\sigma\right)^{1/2}}. \tag{3.27}$$

The final stationary state of an initially mismatched bunch is approximately uniform in real space, so the total average energy per particle can be defined with Eq. (3.28)

$$W_f = \frac{1}{10}\left(k_{\perp}a_f\right)^2\left(1+3f_{\perp}\left(a_f,b_f\right)\right). + \frac{1}{20}\left(k_{\parallel}b_f\right)^2\left(1+3f_{\parallel}\left(a_f,b_f\right)\right) + \frac{3K_{\mathrm{sc}}}{16}\int_0^{\infty}\frac{d\sigma}{\left(a_f{}^2+\sigma\right)\left(b_f{}^2+\sigma\right)^{1/2}}, \tag{3.28}$$

Although an initial mismatch often develops a low-density tail around the beam core, the number of these halo particles is typically a few percent of N_b. We, therefore, assume a uniform density profile to be approximately valid in the final state, as Reiser did in his original work for a coasting beam [22]. By expanding W_f about the matched state and keeping only low-order terms, an approximate expression of the excess energy ΔW takes the form

$$\frac{\Delta W}{(k_{\perp}a_0)^2} = \frac{1}{20}(11\eta_{\perp}{}^2-3)\left[\left(\frac{a_f}{a_0}\right)^2-1\right] + \frac{1}{40}(11\eta_{\parallel}{}^2-3)\left(\frac{\eta_{\perp}}{\eta_{\parallel}}\right)^2\left[\left(\frac{b_f}{b_0}\right)^2-1\right] + \frac{3Q_0}{20}\left[4I_1(R_0)\left(\frac{a_f}{a_0}\right)^2 + I_2(R_0)\left(\frac{b_f}{b_0}\right)^2\right]\left[\left(\frac{a_f}{a_0}\right)^2-1\right] + \frac{3Q_0}{40}\left[2I_2(R_0)\left(\frac{a_f}{a_0}\right)^2 + 3I_3(R_0)\left(\frac{b_f}{b_0}\right)^2\right]\left[\left(\frac{b_f}{b_0}\right)^2-1\right], \tag{3.29}$$

where $I_1(R_0)$, $I_2(R_0)$, and $I_3(R_0)$ are defined as

$$I_1(R_0) = \int_0^{\infty}\frac{d\sigma'}{(1+\sigma')^3\left(R_0{}^2+\sigma'\right)^{1/2}}, \tag{3.30.a}$$

$$I_2(R_0) = R_0{}^2\int_0^{\infty}\frac{d\sigma'}{(1+\sigma')^2\left(R_0{}^2+\sigma'\right)^{3/2}}, \tag{3.30.b}$$

$$I_3(R_0) = {R_0}^4 \int_0^\infty \frac{d\sigma'}{(1+\sigma')\left({R_0}^2+\sigma'\right)^{5/2}}. \tag{3.30.c}$$

After the relaxation process of an initially mismatched beam is completed, the transverse rms emittance has reached the approximate final value of Eq. (3.31), the emittance growth rate can thus be estimated from

$$\epsilon_{\perp f} = \frac{k_\perp \left[f_\perp(a_f, b_f)\right]^{1/2} {a_f}^2}{5} \text{ and } \epsilon_{\|\mathrm{f}} = \frac{k_\| \left[f_\|(a_f, b_f)\right]^{1/2} {b_f}^2}{5}, \tag{3.31}$$

$$\frac{\epsilon_{\perp f}}{\epsilon_{\perp 0}} \approx \frac{1}{\eta_\perp}\left(\frac{a_f}{a_0}\right)^2 \left[f_\perp(a_f, b_f)\right]^{1/2} \tag{3.32.a}$$

$$\approx \left(\frac{a_f}{a_0}\right)^2 \sqrt{1 + \frac{2Q_0 I_1(R_0)}{{\eta_\perp}^2}\left[\left(\frac{a_f}{a_0}\right)^2 - 1\right] + \frac{Q_0 I_2(R_0)}{2{\eta_\perp}^2}\left[\left(\frac{b_f}{b_0}\right)^2 - 1\right]},$$

$$\frac{\epsilon_{\| f}}{\epsilon_{\| 0}} \approx \frac{1}{\eta_\|}\left(\frac{b_f}{b_0}\right)^2 \left[f_\|(a_f, b_f)\right]^{\frac{1}{2}} \tag{3.32.b}$$

$$\approx \left(\frac{b_f}{b_0}\right)^2 \sqrt{1 + \frac{Q_0 I_2(R_0)}{{\eta_\perp}^2}\left[\left(\frac{a_f}{a_0}\right)^2 - 1\right] + \frac{3Q_0 I_3(R_0)}{2{\eta_\perp}^2}\left[\left(\frac{b_f}{b_0}\right)^2 - 1\right]}.$$

As already mentioned, the values of Q_0 and R_0 are fixed once the tune depressions $\eta_\perp$ and $\eta_\|$ are chosen. Therefore, the additional pieces of information required to find the emittance growth rates are the ratios a_f/a_0 and b_f/b_0.

Unlike the previous study by Reiser [22], two independent conditions are necessary to determine the emittance growth rates because we have one more dimension. The first condition can be obtained from Eq. (3.29) by calculating ΔW for a particular non-stationary initial state. We here focus our discussion on one of the most probable initial errors in general accelerators, i.e., a mismatch in the transverse and longitudinal beam sizes at injection. The corresponding free-energy formula can be given as a function of known parameters, which we employ to derive a relation of a_f/a_0 and b_f/b_0. Although we still need one more condition to determine these ratios, it seems difficult to deduce another useful relation from a simple physical hypothesis. In the latter part of this section, therefore, we try to introduce an empirical formula on the basis of information from self-consistent numerical simulations.

Let us consider a bunch that initially has semi-axes of a_i (transverse) and b_i (longitudinal). Ideally, a_i and b_i must be adjusted precisely to the matched values a_0

and b_0, but, in reality, we can only achieve an approximate matching where $a_i = \xi_\perp a_0$ and $b_i = \xi_\parallel b_0$ with positive constants $\xi_\perp$ and $\xi_\parallel$ is mismatch factors same as defined in the previous section. The total energy W_i of a mismatched bunch can be calculated in the same way as described in the last section:

$$W_i = \frac{1}{10}(k_\perp a_0)^2 \left[\xi_\perp{}^2 + 2\left(\frac{\eta_\perp}{\xi_\perp}\right)^2 + \xi_\perp{}^2 f_\perp(\xi_\perp a_0, \xi_\parallel b_0)\right] + \frac{1}{20}(k_\parallel b_0)^2 \left[\xi_\parallel{}^2 + 2\left(\frac{\eta_\parallel}{\xi_\parallel}\right)^2 + \xi_\parallel{}^2 f_\parallel(\xi_\perp a_0, \xi_\parallel b_0)\right] + \frac{3K_{sc}}{16}\int_0^\infty \frac{d\sigma}{\left(\xi_\perp{}^2 a_0{}^2 + \sigma\right)\left(\xi_\parallel{}^2 b_0{}^2 + \sigma\right)^{1/2}}. \tag{3.33}$$

where we have assumed that the mismatched beam initially has the same rms emittance as the matched beam. Provided that the mismatch is not too large, the free energy can be written as

$$\frac{\Delta W}{(k_\perp a_0)^2} \approx \frac{\xi_\perp{}^2 - 1}{20}\left[\left(\frac{\eta_\perp}{\xi_\perp}\right)^2 \left(7\xi_\perp{}^2 - 4\right) - 3 + 4Q_0\xi_\perp{}^2 I_1(R_0) + Q_0\xi_\parallel{}^2 I_2(R_0)\right] + \frac{\xi_\parallel{}^2 - 1}{40}\left[\left(\frac{\eta_\perp}{\xi_\parallel}\right)^2 \left(7\xi_\parallel{}^2 - 4\right) - 3\left(\frac{\eta_\perp}{\eta_\parallel}\right)^2 + 2Q_0\xi_\perp{}^2 I_2(R_0) + 3Q_0\xi_\parallel{}^2 I_3(R_0)\right]. \tag{3.34}$$

Given the design tune depressions $\eta_\perp$ and $\eta_\parallel$, we can readily evaluate $\Delta W/(k_\perp a_0)^2$ from Eq. (3.34) for a non-stationary bunch that has specific mismatch factors at injection. We then substitute the obtained value of $\Delta W/(k_\perp a_0)^2$ into the left-hand side of Eq. (3.29), which leads to a simple algebraic equation of a_f/a_0 and b_f/b_0.

3.2.2 Temperature anisotropy after relaxation

It may be rational to think that an initially mismatched bunch will relax into an equipartitioned state. If that is the case, the temperature ratio $T_f = k_\perp{}^2 a_f{}^2 f_\perp(a_f, b_f)/k_\parallel{}^2 b_f{}^2 f_\parallel(a_f, b_f)$ should be close to unity after a final quasi-equilibrium is reached. We can then use the equation $T_f = 1$ as the second condition to determinea_f/a_0 and b_f/b_0. We have, however, found through numerical simulations that the final state is often quite anisotropic. Only when $R_0 \approx 1$ (a spherical bunch), the bunch stays near an equipartitioned state unless them is match is too large. In order to judge whether a mismatched beam has reached a quasi-equilibrium state, we paid attention to the time evolution of the transverse and longitudinal rms emittances. Figure 3.2 shows the

typical emittance evolution calculated with the particle-in-cell code "Warp" [87]. Warp was originally developed in Lawrence Berkeley National Laboratory to simulate space charge effects in high-density ion beams for heavy ion fusion. When them is match is large, the rms emittances rapidly grow at the beginning in both the transverse and longitudinal directions and then come to a plateau. Since weak emittance oscillations do not completely vanish within a reasonable CPU time, we take an average over the last few tens of betatron periods to estimate the equilibrium emittance and temperature after relaxation. The temperature ratio T_f in the final state is plotted in Fig. 3.1 at several different bunch densities and aspect ratios as a function of the transverse mismatch factor $\xi_\perp$. The longitudinal mismatch factor $\xi_\parallel$ is varied in the range $0.8 \leq \xi_\parallel \leq 1.2$. The initial distribution of macro-particles is uniform in real space and Maxwellian in velocity space. The figure suggests that the temperature anisotropy in the final state is enhanced as we increase the mismatch and/or bunch density. The observed dependence of the anisotropy on free parameters needs to be incorporated properly into our model. Among a number of possible choices, we here try the following function:

$$
\begin{aligned}
&T_f(\xi_\perp, \xi_\parallel; \eta_\perp, R_0) \\
&\quad \approx 1 + \frac{R_0 - 1}{R_0}\left[(A_1 e^{-A_2 R_0} + A_3)\frac{\left(\xi_\perp^{\mathrm{sgn}(\xi_\perp - 1)} - 1\right)^2}{\eta_\perp}\right. \\
&\qquad \left. + (B_1 e^{-B_2 R_0} + B_3)\frac{\left(\xi_\parallel^{\mathrm{sgn}(\xi_\parallel - 1)} - 1\right)^2}{{\eta_\perp}^3}\right],
\end{aligned}
\tag{3.35}
$$

where constants in the function are given by $A_1 = 1.67, A_2 = 0.27, A_3 = 1.46, B_1 = -1.49, B_2 = 0.43,$ and $B_3 = -1.71$ respectively. The solid lines in Fig. 3.2 are represented by Eq. (3.35) and we can confirm the good agreement between simulation results and solid lines in wide parameters range. Naturally, the temperature anisotropy in the final state is not symmetric about the matched line $\xi_\perp$ = 1 because the bunch initially becomes denser with $\xi_\perp$ < 1 and thinner with $\xi_\perp$ > 1. From the equation $T_f = {k_\perp}^2 {a_f}^2 f_\perp(a_f, b_f)/{k_\parallel}^2 {b_f}^2 f_\parallel(a_f, b_f)$, we have

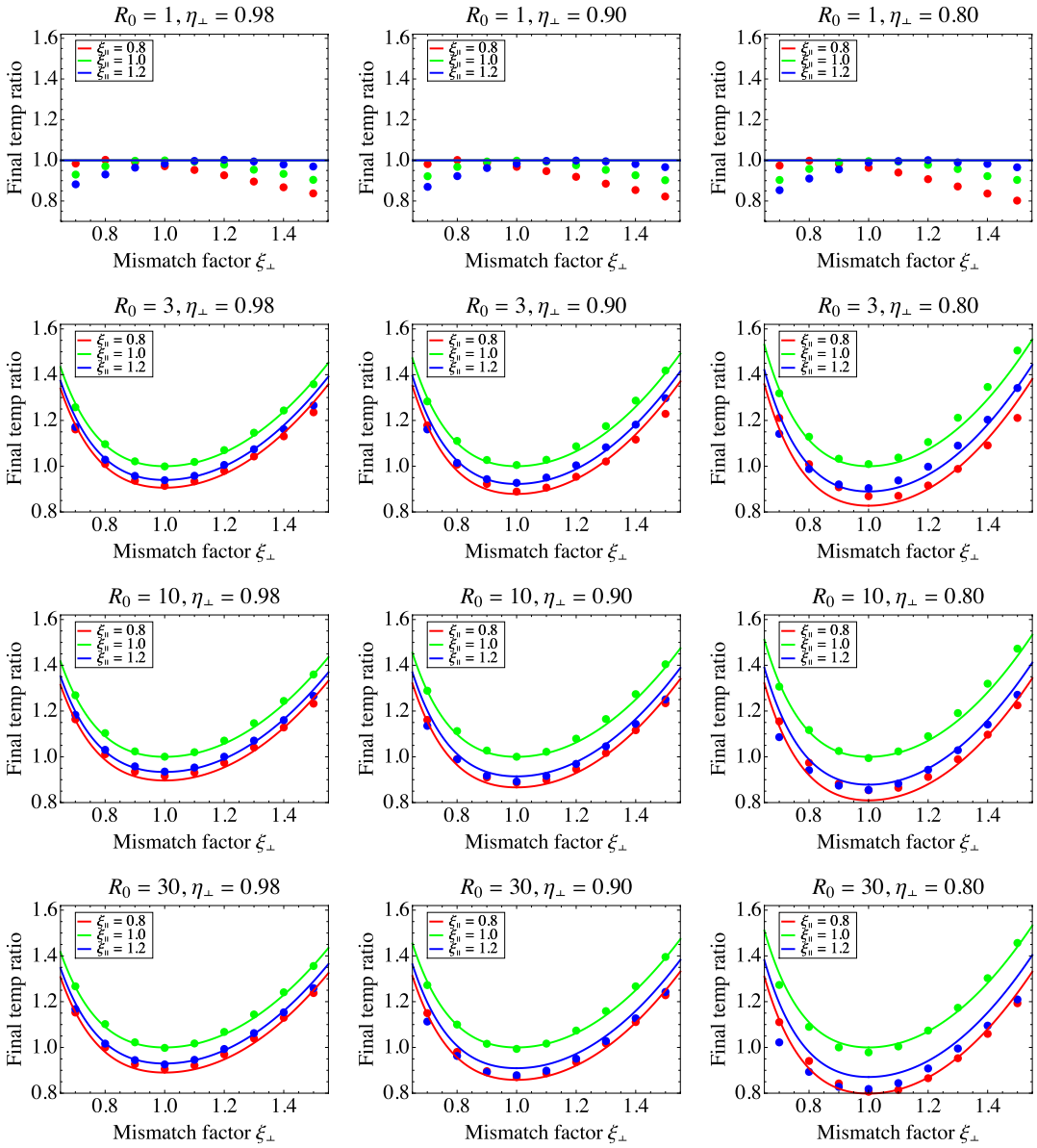

Fig. 3.1: The final temperature ratio of each simulation result as a function of the transverse mismatch factor $\xi_\perp$. The dots represent the final temperature ratio of simulation results and solid lines are drawn by the function defined as Eq. (3.35). In the case of $R_0 = 1$, there is a little difference between simulation results and solid lines, however we can see the good agreement of the other aspect ratios.

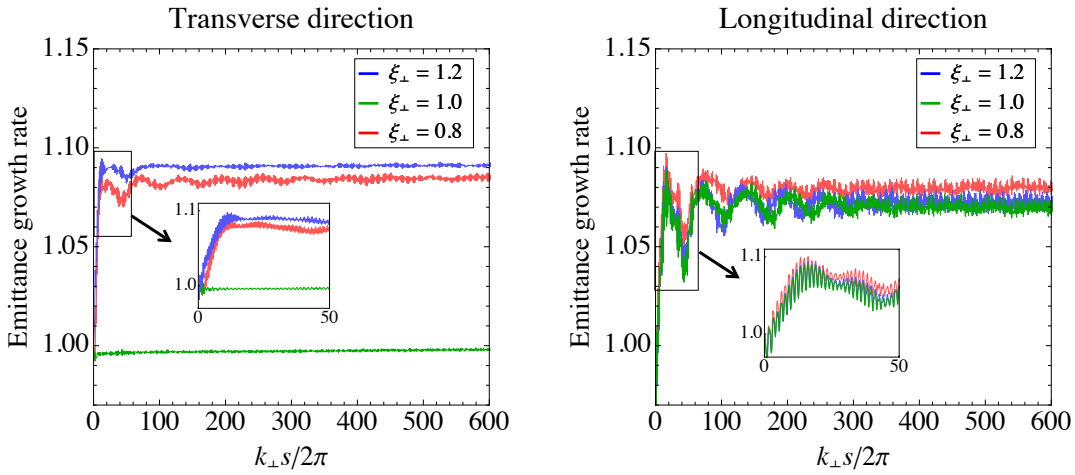

Fig. 3.2: The time evolution of emittance growth rate in both transverse and longitudinal direction. The aspect ratio of the beam is $R_0 = 3$ and the transverse tune depression is $\eta_\perp = 0.8$. The transverse mismatch factor $\xi_\perp$ are verified from 0.8 to 1.2 and longitudinal mismatch factor $\xi_\parallel$ fixwd at 1.2. The rms emittance enhanced within a few tens of betatron oscillations, after that reach to a quasi-equilibrium state in both transverse and longitudinal direction.

$$T_f = \frac{{k_\perp}^2 {a_f}^2 f_\perp(a_f, b_f)}{{k_\parallel}^2 {b_f}^2 f_\parallel(a_f, b_f)} \tag{3.36}$$

$$\approx \frac{\left(\frac{a_f}{a_0}\right)^2 \left\{1 + \frac{2Q_0 I_1(R_0)}{{\eta_\perp}^2}\left[\left(\frac{a_f}{a_0}\right)^2 - 1\right] + \frac{Q_0 I_2(R_0)}{2{\eta_\perp}^2}\left[\left(\frac{b_f}{b_0}\right)^2 - 1\right]\right\}}{\left(\frac{b_f}{b_0}\right)^2 \left\{1 + \frac{Q_0 I_2(R_0)}{{\eta_\perp}^2}\left[\left(\frac{a_f}{a_0}\right)^2 - 1\right] + \frac{3Q_0 I_3(R_0)}{2{\eta_\perp}^2}\left[\left(\frac{b_f}{b_0}\right)^2 - 1\right]\right\}},$$

which gives another explicit relation of a_f/a_0 and b_f/b_0 once the initial tune depressions and mismatch factors are chosen. Together with the free-energy equation, i.e. Eq. (3.29) equated to Eq. (3.34), we now have sufficient conditions to determine a_f/a_0 and b_f/b_0, the values of which are inserted into Eqs. (3.32) for emittance-growth evaluation.

(i) Initial distribution, $R_0 = 3,\ \eta_\perp = 0.98,\ \xi_\perp = \xi_{II} = 1.2$

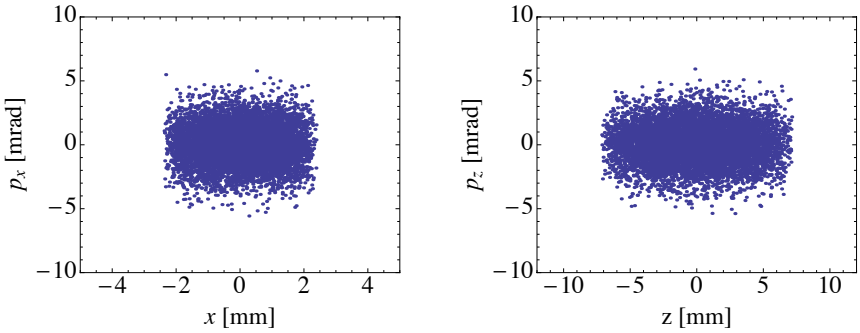

(ii) Final distribution, $R_0 = 3,\ \eta_\perp = 0.98,\ \xi_\perp = \xi_{II} = 1.2$

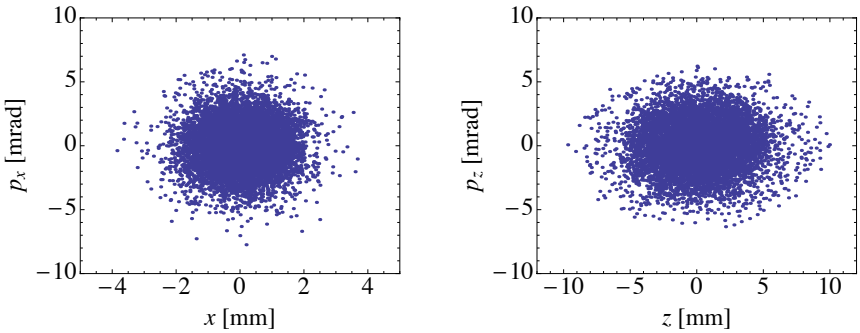

Fig. 3.3: The typical phase space distributions of initially mismatched beam in the horizontal and the longitudinal degrees of freedom. The extension of the phase space areas at final stationary states means the emittance growth due to initial beam mismatches.

3.3 Comparison of theoretical predictions with Warp simulations

Systematic Warp simulations were performed to verify how accurately the present theoretical model predicts the rms emittance growth of an initially mismatched bunch. We considered the fundamental parameters listed in Table 3.1. As explained above, we only need two given independent parameters to construct an equipartitioned matched state; namely, we can uniquely define the matched state by fixing two of the four parameters ($\eta_\perp$, $\eta_\parallel$, R_0, and Q_0). In the numerical examples here, we take the aspect ratio R0 and the transverse tune depression $\eta\perp$ under the equipartitioning condition in Eq. (3.21), and then apply a spatial bunch deformation corresponding to given mismatch factors $\xi_\perp$ and $\xi_\parallel$.

Table 3.1 Simulation parameters of initially mismatched beams.

Aspect ratio R_0	1, 2, 3, 6, 10, 30
Transverse tune depression $\eta_\perp$	0.98, 0.90, 0.80
Transverse mismatch factor $\xi_\perp$	0.7 ~ 1.5
Longitudinal mismatch factor $\xi_\parallel$	0.8 ~ 1.2

3.3.1 Tune depression $\eta_\perp = 0.98$

Let us first look at a relatively low-density case, setting $\eta_\perp$ = 0.98. The longitudinal tune depression $\eta_\parallel$ ranges from 0.98 to 0.80 corresponding to the change of the aspect ratio R_0 from 1 to 30. Figure 3.4 shows the transverse rms emittance growth rate plotted as a function of $\xi_\perp$. Five different values of $\xi_\parallel$ are considered in each panel where the aspect ratio is fixed at either 1, 3, or 30. The five colored curves are theoretical predictions based on the emittance-growth formula in Eq. (3.32). Following the prescription described in previous sections, we first insert the given numbers of $\eta_\perp$ and R_0 into the free-energy formula (Eq. (3.29) together with Eq. (3.34)) and the temperature anisotropy formula (Eq. (3.36) together with Eq. (3.35)). These two conditions are then solved with specific mismatch factors to find the ratios a_f/a_0 and b_f/b_0 that are substituted in Eq. (3.32) to predict the emittance growth rate. Colored dots in each panel represent Warp simulation results. We see that the free-energy model can explain the Warp data very well. Note that, at this tune depression, the transverse emittance growth rate is insensitive to the longitudinal mismatch factor $\xi_\parallel$. Similar results have been obtained for other aspect ratios, i.e. R_0 = 2, 6, and 10. Reasonable agreement between the theory and self-consistent simulations is also confirmed for the longitudinal degree of freedom, as demonstrated in Fig. 3.5. Interestingly, the longitudinal growth rate appears to be almost independent of $\xi_\perp$ and R_0, except for the spherical bunch (R_0 = 1).

(a) Transverse direction

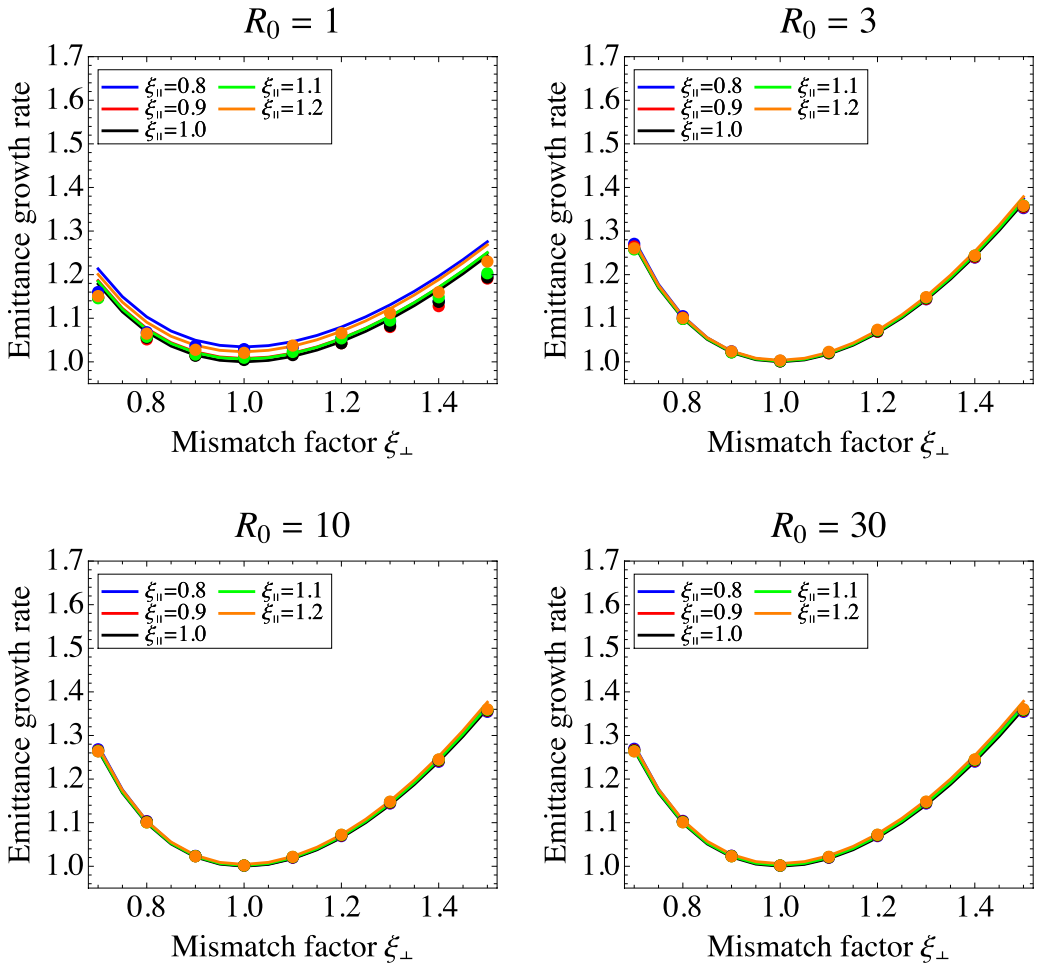

Fig. 3.4: The growth rates of the rms emittance in the transverse direction are plotted as a function of transverse mismatch factor $\xi_{\perp}$. The tune depression fixed at $\eta_{\perp}$= 0.98. Colored dots represent Warp simulation results based on the fundamental parameters in Table 3.1. Different colors stand for different longitudinal mismatch factors: $\xi_{\parallel}$ = 0.8 (blue), 0.9 (red), 1.0 (black), 1.1 (green), and 1.2 (orange). Solid lines are the predictions from the free-energy model. The results obtained with other aspect ratios (R_0 = 2 and 6) are similar to those of R_0 = 3, 10, and 30.

(b) Longitudinal direction

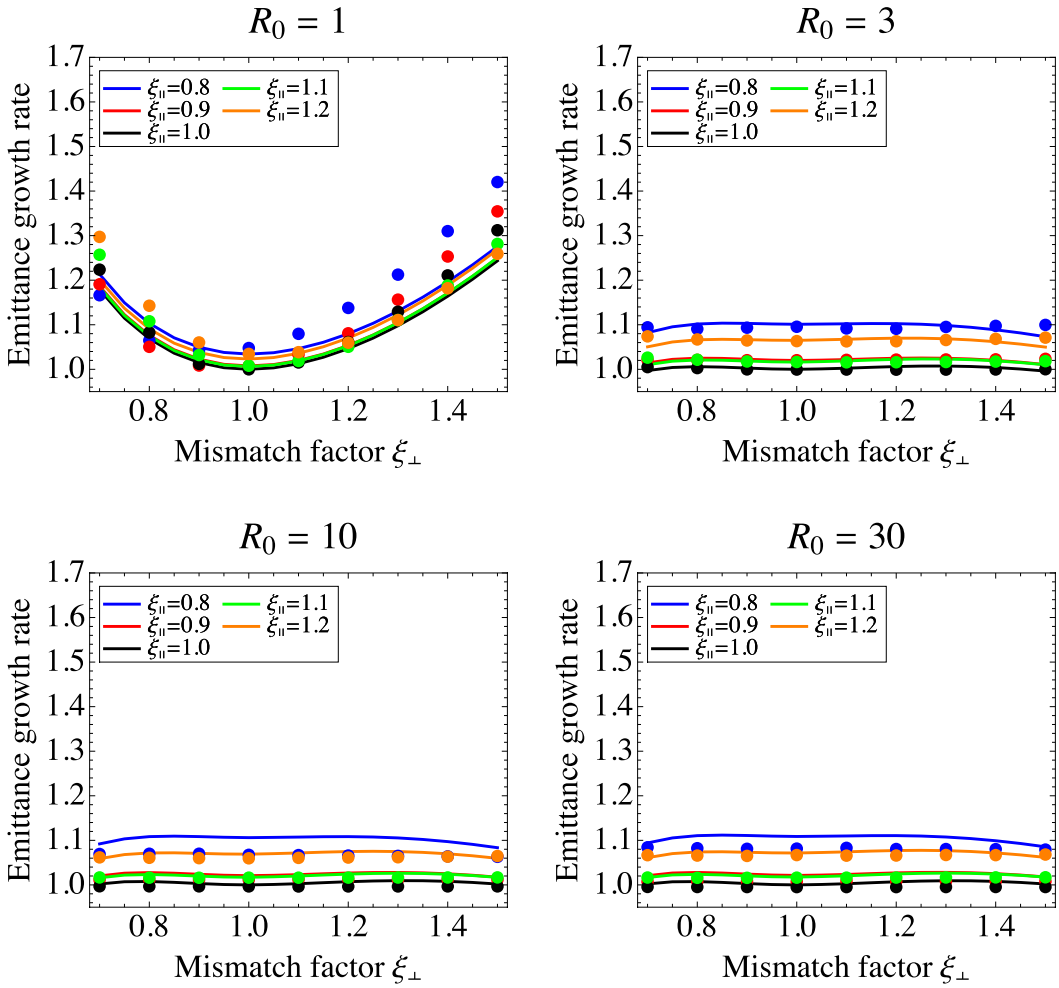

Fig. 3.5: The growth rates of the rms emittance in the longitudinal direction are plotted as a function of transverse mismatch factor $\xi_\perp$. The tune depression fixed at $\eta_\perp$= 0.98. Similar to the case of transverse direction, the results show the good agreement between the theory and simulations.

3.3.2 Tune depression $\eta_\perp = 0.90$

We now increase the bunch density from $\eta_\perp$ = 0.98 to higher levels where $\eta_\perp$ is set equal to 0.9 or 0.8 initially. Theoretical and simulation results in the case of $\eta_\perp$ = 0.9 are summarized in Fig. 3.6 and 3.7. We again only show the data obtained with R_0 = 1, 3, and 30. The dependence of rms emittance growth on the mismatch factors is more or less similar to what we found in Fig. 3.4 and 3.5. In any case, the theoretical estimate from the free-energy model is in good agreement with the corresponding Warp results over the whole parameter ranges considered here.

3.3.3 Tune depression $\eta_\perp = 0.80$

Figure 3.8 and 3.9 show the results of $\eta_\perp$ = 0.8. The transverse emittance growth is slightly enhanced compared to the lower-density cases in Fig. 3.3 and 3.4 while, in the longitudinal direction, no significant change is observed. We recognize that the accuracy of the theoretical prediction is somewhat worsened, especially in the longitudinal emittance growth estimate. A possible reason for this is the deterioration of the fitting accuracy by Eq. (3.35). Another reason could be a deviation of the final bunch profile from the uniform distribution assumed in our model. In fact, a noticeable beam halo is inevitably formed around the core as we increase the bunch density and the degree of initial mismatches. Typical phase-space distributions of mismatched bunches after relaxation are shown in Fig. 3.10 for reference. Despite these limitations, it is evident from Figs. 3.6–3.10 that the present formulas are useful in estimating the rate of potential emittance growth.

(a) Transverse direction

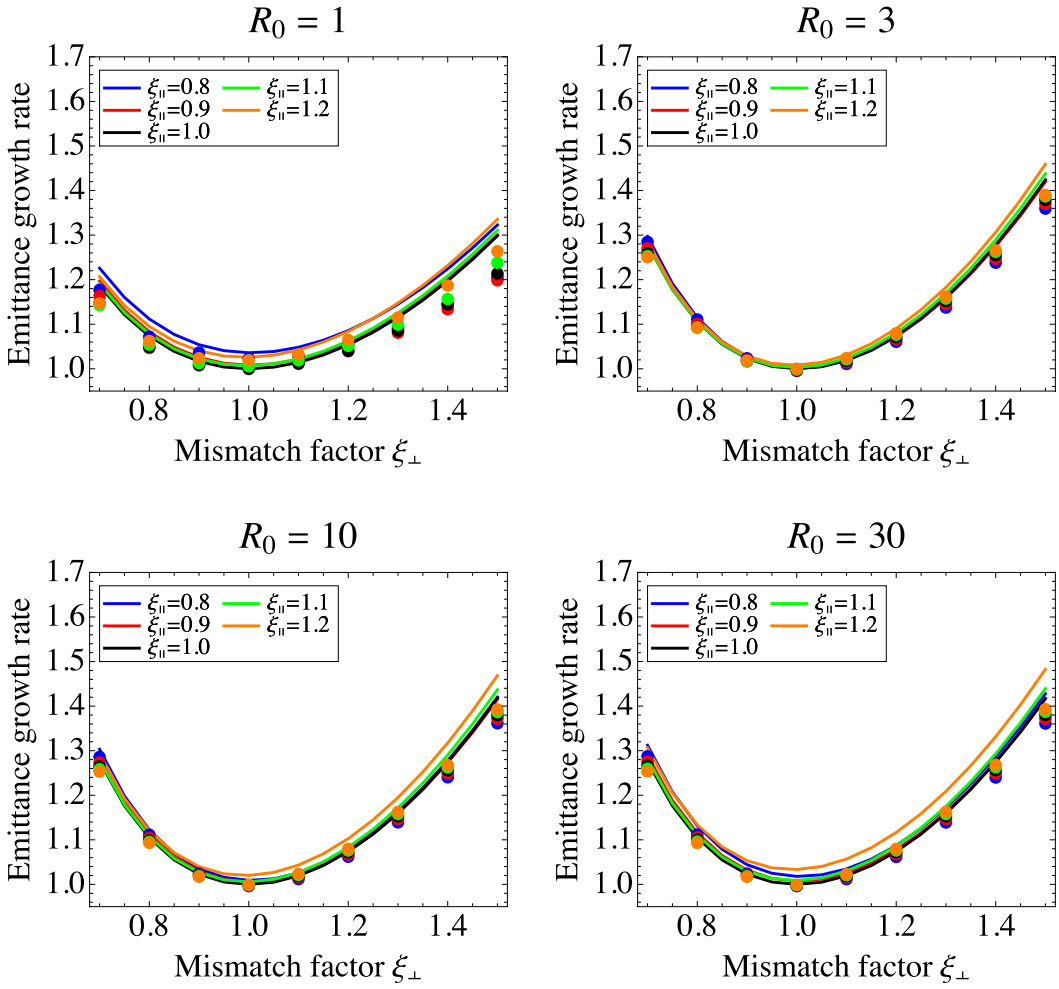

Fig. 3.6: Transverse rms emittance growth at $\eta_\perp$ = 0.9. Theoretical predictions from the free-energy model are compared with Warp simulation results. Fundamental parameters considered here are the same as those in Figs. 3.5 and 3.6. except for the bunch density. The longitudinal tune depression $\eta_\parallel$ ranges from 0.9 to 0.64 corresponding to the change of R_0 from 1 to 30.

(b) Longitudinal direction

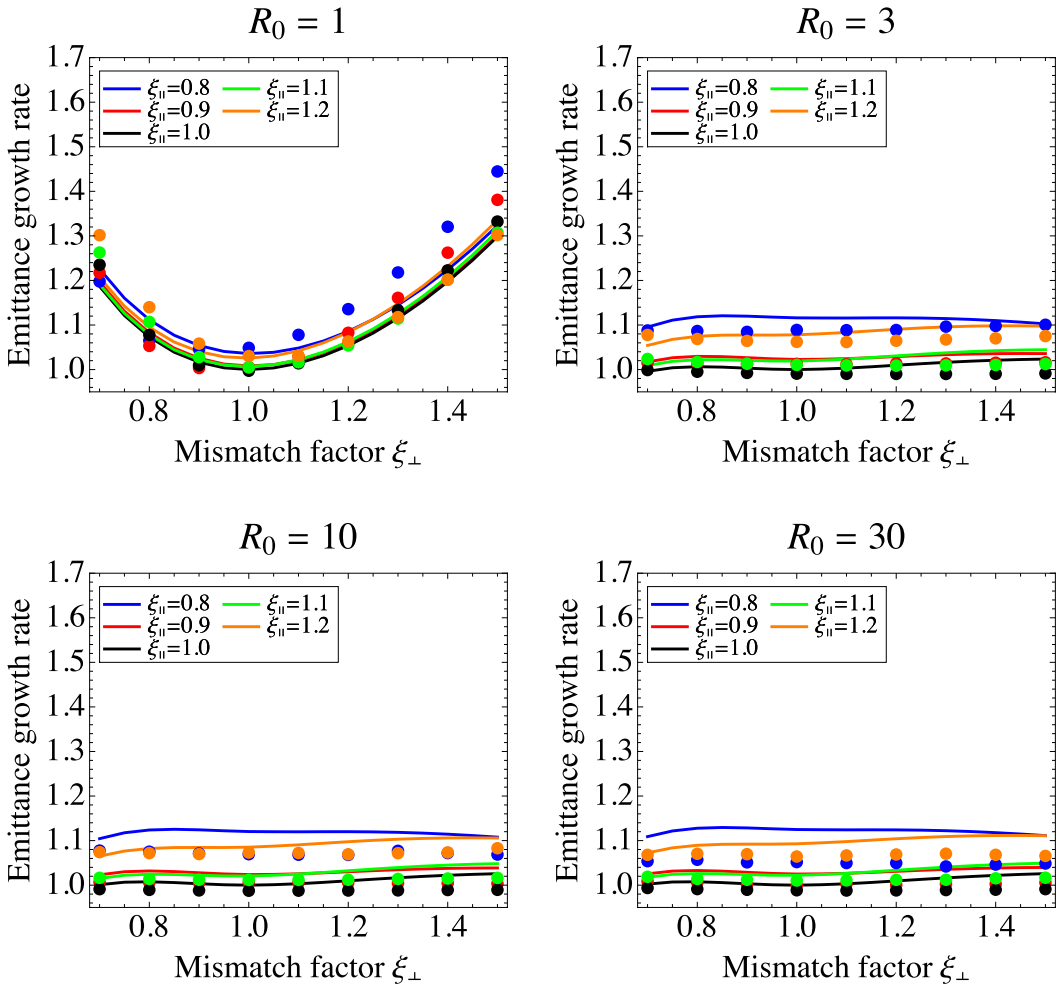

Fig. 3.7: Rms emittance growth of longitudinal degree of freedom at $\eta_{\perp}$ = 0.9.

(a) Transverse direction

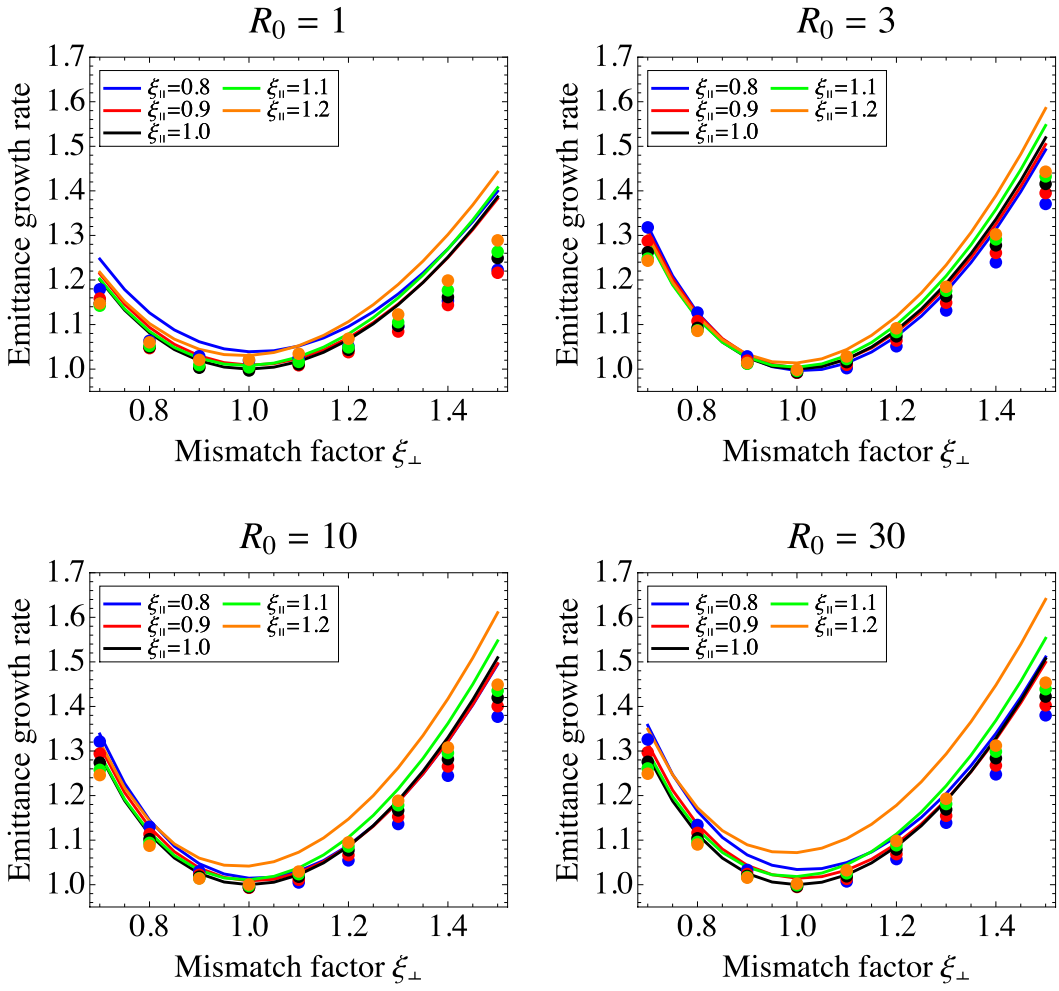

Fig. 3.8: Transverse rms emittance growth at $\eta_\perp$ = 0.8. Theoretical predictions from the free-energy model are compared with Warp simulation results. Fundamental parameters considered here are the same as those in Figs. 3.5 and 3.6. except for the bunch density. The longitudinal tune depression $\eta_\parallel$ ranges from 0.9 to 0.64 corresponding to the change of R_0 from 1 to 30.

(b) Longitudinal direction

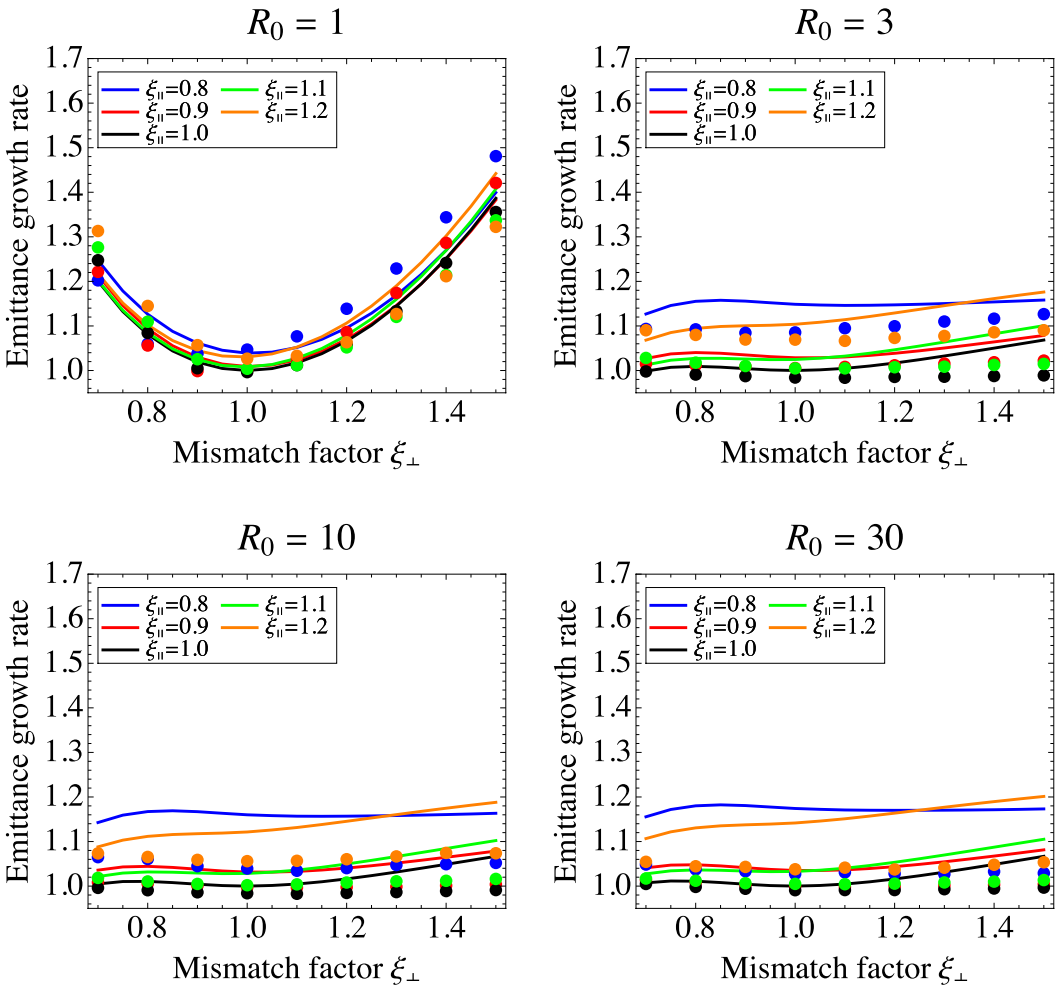

Fig. 3.9: Rms emittance growth of longitudinal degree of freedom at $\eta_\perp$ = 0.8.

(i) Final distribution, $R_0 = 3,\ \eta_\perp = 0.98,\ \xi_\perp = 1.5, \xi_{\shortparallel} = 1.2$

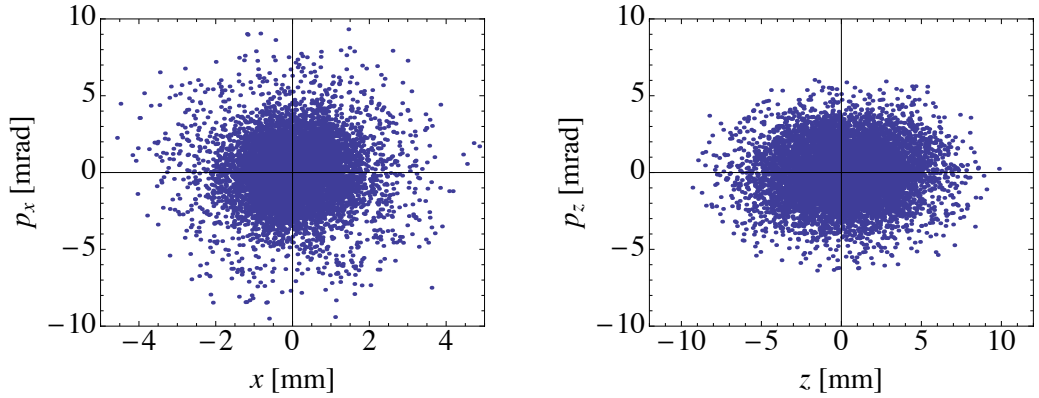

(ii) Final distribution, $R_0 = 3,\ \eta_\perp = 0.80,\ \xi_\perp = 1.5, \xi_{\shortparallel} = 1.2$

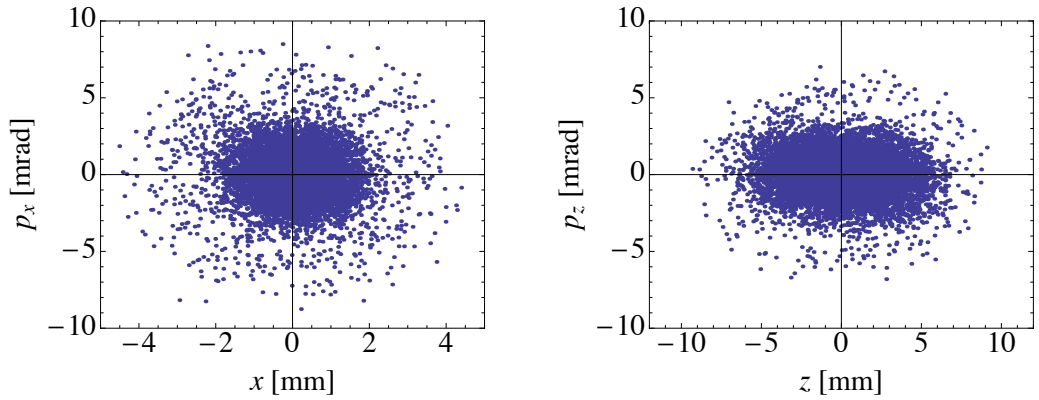

Fig. 3.10: The final phase space distributions in the horizontal and the longitudinal direction. The upper panels are the case of a low-density bunch $\eta_\perp = 0.98$ and lower panels are the case of a high-density bunch $\eta_\perp = 0.80$. Due to the large initial mismatch in both transverse and longitudinal direction, we can confirm the existence of the beam halo around the beam core.

3.4 Summary

We have developed a simple analytic theory to estimate the rms emittance growth of an intense beam when its spatial extent disagrees with the ideal matched value at injection. The Reiser's free-energy model for a coasting beam is generalized to treat an ellipsoidal bunch focused three-dimensionally by a linear external potential. Given the initial beam density, or more correctly, two of the four free parameters $(\eta_\perp, \eta_\parallel, R_0, Q_0)$, the stationary matched state is uniquely defined. The transverse and longitudinal emittance growth rates can then be calculated from Eqs. (3.32.a) and (3.32.b) for a certain degree of initial bunch deformation characterized by the mismatch factors $\xi_\perp$ and $\xi_\parallel$. To find the ratios a_f/a_0 and b_f/b_0 in these equations, we employ the free-energy formula which we have obtained. The left hand side of Eq. (3.29), i.e. the excess free energy of an initially mismatched bunch, is evaluated from Eq. (3.34) for specific mismatch factors, which yields an explicit relation of a_f/a_0 and b_f/b_0. Similarly, Eq. (3.36) gives another relation of a_f/a_0 and b_f/b_0 if the temperature anisotropy T_f is known as a function of the mismatch factors. In the present study, we carried out systematic numerical simulations to clarify the parameter dependence of T_f. Equation (3.35) is a possible choice that fits numerical data over a wide range of parameters at reasonable accuracy. Equation of the free energy and the temperature anisotropy after relaxation of mismatched beams make it possible to determine a_f/a_0 and b_f/b_0 that are substituted in Eq. (3.32.a) and (3.32.b) to obtain the emittance growth rates. We compared theoretical predictions with time-consuming multi-particle simulations, confirming that the present model can explain self-consistent numerical results fairly well. The simple algebraic equations derived in this paper thus enable us to estimate the degree of mismatch-induced emittance growth in an intense bunch easily and quickly.

Reference

[1] J. D. Cockcroft, E.T.S. Walton, Proc. Royal Soc. London, Series A136 (1932) p.619

[2] Japanese report of the National Institute of Science and Technology Policy can be downloaded from the URL

[3] Lawrence,Edlefsen,ScienceLXXII, 376 (1930).

[4] M. O. Oliphant, The acceleration of particles to very high energies, Classified memo submitted to DSIR (1943), U. Birmingham Archive

[5] A. W. Chao and M. Tigner (eds.), Handbook of Accelerator Physics and Engineering (World Scientific, Singapore, 1999) and references therein.

[6] C.Karzmark, R.Morton, Medical Physics Publishing Corp., Madison 1989

[7] J.Purdy, D.A.Goer, Nucl. Instrum. Methods Phys. B10/11, 1090-95 1985

[8] Liouville, J. Math. Pures Appl.3, 342 (1838).

[9] G. I. Budker, Atomnaja Energia 22 346 (1967).

[10] S. van der Meer, CERN Report CERN/ISR-PO/72-31 (1972).

[11] T. Hansch and A. Schawlow, Opt. Commun. 13, 68 (1975);

[12] D. J. Wineland and H. Dehmelt, Bull. Am. Phys. Soc. 20, 637 (1975).

[13] S. Schroder et al., Phys. Rev. Lett. 64, 2901 (1990).

[14] J. S. Hangst et al., Phys. Rev. Lett. 67, 1238 (1991).

[15] H. Souda et al., Jpn. J. Appl. Phys. 52, 030202 (2013).

[16] A. Noda, M. Nakao, H. Okamoto, K. Osaki, Y. Yuri, H. Souda, H. Tonguu, K. Jimbo, M. Grieser, Z. He, and A. Smirnov, Proc. 5th International Particle Accelerator Conf. (2014) pp. 28 – 33.

[17] H. Okamoto, A. M. Sessler and D. Mo¨hl, Phys. Rev. Lett. 72, 3977 (1994).

[18] H. Okamoto, Phys. Rev. E 50, 4982 (1994)

[19] Dr. Yosuke Yuri, private note

[20] K. Osaki and H. Okamoto, Prog. Theor. Exp. Phys. 2014, 053G01.

[21] T. P. Wangler, RF Linear Accelerators (Wiley, 2008)

[22] M. Reiser, J. Appl. Phys. 70, 1919 (1991).

[23] E. D. Courant and H. S. Snyder, Ann. Phys. 3, 1 (1958)

[24] S. Y. Lee, Accelerator Physics, (World Scientific, Singapore, 1999).

[25] H. Wiedemann, Particle Accelerator Physics, (Springer, Berlin,2007)
[26] G. Guignard, CERN 76 – 06, (1976).
[27] G. Guignard, CERN 78 – 11, (1978).
[28] H. Okamoto, H. Sugimoto, and Y. Yuri J. Plasma Fusion Res., 8, 950, 954, (2009).
[29] H. Okamoto, K.Yokoya, Nucl. Instrum. Meth. A 482, 51 (2002).
[30] I.M. Kapchinsky and V.V. Vladimirsky, in Proceed. Int. Conf. on High Energy Accelerators (CERN, Geneva, 1959), p. 274
[31] Steven M. Lund, Takashi Kikuchi, and Ronald C. Davidson. Phys. Rev. ST Accel. Beams 12, 114801 (2009).
[32] I. Hofmann et al., Particle Accelerators 13, 145 (1983).
[33] M. Reiser, Theory and Design of Charged Particle Beams (John Wiley & Sons, Inc., New York, 1994), and references therein.
[34] R.C. Davidson, "An Introduction to the Physics of Nonneutral Plasmas" (Addison-Wesley, Redwood City, 1990) and references therein.
[35] R. C. Davidson and H. Qin, Physics of Intense Charged Particle Beams in High Energy Accelerators (World Scientific, New York, 2001), and references therein.
[36] Robert L. Gluckstern, Wen-Hao Cheng, and Huanchun Ye. Phys. Rev. Lett. 75, 2835 (1995).
[37] I. Hofmann. Phys. Rev. E 57, 4713 (1998).
[38] I. Hofmann et al., Phys. Rev. ST Accel. Beams 6, 024202 (2003).
[39] T.-S. F. Wang. Phys. Rev. ST Accel. Beams 7, 024201 (2004)
[40] Steven M. Lund and Boris Bukh. Phys. Rev. ST Accel. Beams 7, 024801 (2004).
[41] Steven M. Lund, Sven H. Chilton, and Edward P. Lee. Phys. Rev. ST Accel. Beams 9, 064201 (2006).
[42] F. J. Sacherer, IEEE Trans. Nucl. Sci. 18, 1105 (1971).
[43] F. J. Sacherer, ”TRANSVERSE SPACE-CHARGE EFFECTS IN CIRCULAR AC- CELERATORS”, Ph.D.Thesis, University of California Berkeley, UCRL-18454, (1968).
[44] V. V. Parkhomchuk and D. V. Pestrikov, Soviet Physics Technical Physics 25 818 (1980);
[45] E. N. Dement’ev et al., Soviet Physics Technical Physics 25 , 1001 (1980).
[46] R. W. Hasse and J. P. Schiffer, Ann. Phys. 203 , 419 (1990).
[47] J. Wei, H. Okamoto and A. M. Sessler, Phys. Rev. Lett. 80, 2606 (1998)

[48] J. Wei, X.-P. Li and A. M. Sessler, Brookhaven National Laboratory Report BNL-52381 (1993).
[49] J. Wei, X-P. Li and A. M. Sessler, Phys. Rev. Lett. 73 , 3089 (1994).
[50] J. Wei et al., in Crystalline Beams and Related Issues, 229 (1996).
[51] M. Nakao et al., Phys. Rev. ST Accel. Beams. 15, 110102 (2012).
[52] S. Ichimaru, Rev. Mod. Phys. 54 , 1017 (1982).
[53] D. H. E. Dubin and T. M. O'Neil, Rev. Mod. Phys. 71 , 87 (1999).
[54] S. N. Atutov et al. , Phys. Rev. L 80 , 2129 (1998).
[55] G. Birkl, S. Kassner and H. Walther, Nature 357 , 310 (1992).
[56] H. Okamoto, H. Tanaka, Nucl. Instrum. Meth. A 437, 178. (1999).
[57] H . Okamoto, Y. Wada, and R. Takai, Nucl. Instrum. Meth. A 485, 244-254 (2002).
[58] K.Okabe and H.Okamoto, Jpn. J. Appl. Phys 42, 4584 (2003)
[59] T. Kihara et al., Phys. Rev. E 59 , 3594 (1999).
[60] H. Okamoto and J. Wei, Phys. Rev. E 58 , 3817 (1998).
[61] D. J. Wineland and W. M. Itano, Phys. Rev. A 20 , 1521 (1979).
[62] S. Stenholm, Rev. Mod. Phys. 58 , 699 (1986).
[63] J. Javanainen and S. Stenholm, Appl. Phys. 21 , 35 (1980).
[64] Y. Yuri and H. Okamoto, Phys. Rev. Lett. 93, 204801 (2004).
[65] Y. Yuri and H. Okamoto, Phys. Rev. ST Accel. Beams 8, 114201 (2005).
[66] M. Reiser, in Proceedings of the 1991 Particle Accelerator Conference, eds. L. Lizama et al. (IEEE, San Francisco, CA, 1991), p. 2497.
[67] A. Cucchetti, M. Reiser, and T. Wangler, in Proceedings of the 1991 Particle
[68] R. L. Gluckstern, Phys. Rev. Lett. 73, 1247 (1994).
[69] J. M. Lagniel, Nucl. Instrum. Meth. A 345, 46 (1994).
[70] J. M. Lagniel, Nucl. Instrum. Meth. A 345, 405 (1994).
[71] A. Riabko, M. Ellison, X. Kang, S. Y. Lee, D. Li, J. Y. Liu, X. Pei, and L. Wang, Phys. Rev. E 51, 3529 (1995).
[72] H. Okamoto and M. Ikegami, Phys. Rev. E 55, 4694 (1997).
[73] I. Hofmann. Phys. Rev. ST Accel. Beams 16, 084201 (2013)
[74] I. Hofmann and J. Struckmeier, Part. Accel. 21, 69 (1987)
[75] S.M. Lund, J.J. Barnard, Proceedings of the 1997 ParticleAccelerator Conference, IEEE, Piscataway, 1998, p. 1932.

[76] J.J. Barnard, S.M. Lund, Proceedings of the 1997Particle Accelerator Conference, IEEE, Piscataway, 1998,p. 1929.

[77] M. Ikegami, H. Okamoto, Jpn. J. Appl. Phys. 36 (1997) 7028.

[78] Yu.Senichev, N.Vasyukhin, Nucl. Instrum. Meth. A 561, 166 (2006).

[79] R. L. Gluckstern, A. V. Fedotov, S. S. Kurennoy, and R. D. Ryne, Phys. Rev. E 58, 4977 (1998).

[80] R. L. Gluckstern. W. H. Cheng. S. S. Kurennoy. H. Ye Phys. Rev E 54, 6788 (1996).

[81] P. Muggli et al., Phys. Rev. Lett 101, 055001 (2008) .

[82] A. V. Fedotov, R. L. Gluckstern, S. S. Kurennoy, and R. D. Ryne. Phys. Rev. ST Accel. Beams 2, 014201 (1999).

[83] Ji Qiang and Robert D. Ryne. Phys. Rev. ST Accel. Beams 3, 064201 (2000).

[84] Kiran G. Sonnad and John R. Cary. Phys. Rev. ST Accel. Beams 8, 064202 (2005).

[85] T. P. Wangler, K. R. Crandall, R. Ryne, and T. S. Wang. Phys. Rev. ST Accel. Beams 1, 084201 (1998).

[86] R. A. Jameson, IEEE Trans. Nucl. Sci. 28, 2408 (1981).

[87] D. P. Grote, A. Friedman, G. D. Craig, I. Haber, and W. M. Sharp, Nucl. Instrum. Meth. A464, 563 (2001).

Appendix A

Molecular Dynamics simulation codes are used frequently when Coulomb collisions have an important role. In the calculation of MD codes, accurate Coulomb interactions between all particles can considered, as a result the calculation time of MD codes increases proportional to the square of the particle number. Therefore it is difficult to apply Molecular Dynamics simulation codes to the typical beams in accelerators due to the extremely long CPU time.

In a MD simulation code, we suppose a periodic distribution of a beam in the longitudinal direction and divided them into periodic cells like Fig. A.1. Coulomb potential of charged particles in a same MD cell (black arrows) are written like a following formula (A.1). N in Eq. (A.1) is the particle number in a MD cell.

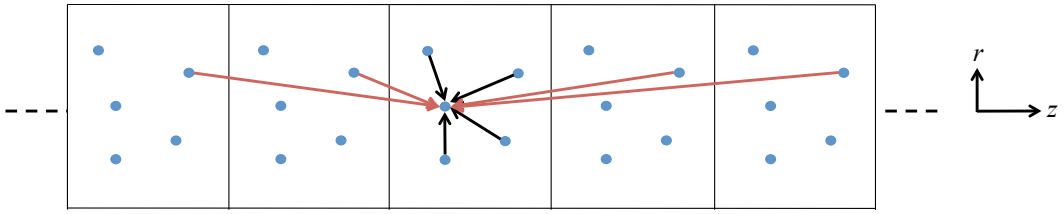

Fig. A.1 : Calculation of Coulomb interactions in MD simulation code. We should consider not only the Coulomb force from the charged particles in the bunch, but also from other bunches like red allows.

$$U_{cell} \propto \sum_{i=1}^{N} \frac{1}{[(r-r_i)^2 + (z-z_i)^2]^{1/2}}. \qquad \text{(A.1)}$$

Coulomb potential generated from the particles in other cells like red allows is written as

$$U_{MD} = \sum_{i=1}^{N} \int_0^{\infty} A(k) \left[\cosh\left(\frac{k(z-z_i)}{L}\right) J_0\left(\frac{k(r-r_i)}{L}\right) - 1 \right] dk. \qquad \text{(A.2)}$$

where J_0 is Bessel function of order 0. The total self-field potential is expressed as $U = U_{MD} + U_{cell}$. The periodic particle distribution in the longitudinal direction is

assumed, therefore the following periodic boundary condition is carried out.

$$\frac{\partial U_{MD}(r,-L/2)}{\partial z} = \frac{\partial U_{MD}(r,L/2)}{\partial z} = 0, \tag{A.2}$$

where L is the length of a MD cell. As a result, $A(k)$ in Eq. (A.2) can be obtained as $A(k) = 2/(L(e^k - 1))$. From these self-potentials, the equation of motion in the three degrees of freedom can be written as

$$\frac{\partial U}{\partial x} = -\sum_{i=1}^{N}\left[\frac{x - x_i}{[(r-r_i)^2 + (z-z_i)^2]^{3/2}}\right. \tag{A.3.a}$$

$$\left. + \frac{x - x_i}{r - r_i}\frac{4}{L^2}\int_0^\infty \frac{e^{-k}k}{\sinh(k)}\left[\cosh\left(\frac{2k(z-z_i)}{L}\right)J_1\left(\frac{2k(r-r_i)}{L}\right)\right]dk\right],$$

$$\frac{\partial U}{\partial y} = -\sum_{i=1}^{N}\left[\frac{y - y_i}{[(r-r_i)^2 + (z-z_i)^2]^{3/2}}\right. \tag{A.3.b}$$

$$\left. + \frac{y - y_i}{r - r_i}\frac{4}{L^2}\int_0^\infty \frac{e^{-k}k}{\sinh(k)}\left[\cosh\left(\frac{2k(z-z_i)}{L}\right)J_1\left(\frac{2k(r-r_i)}{L}\right)\right]dk\right],$$

$$\frac{\partial U}{\partial z} = -\sum_{i=1}^{N}\left[\frac{z - z_i}{[(r-r_i)^2 + (z-z_i)^2]^{\frac{3}{2}}}\right. \tag{A.3.c}$$

$$\left. + \frac{z - z_i}{r - r_i}\frac{4}{L^2}\int_0^\infty \frac{e^{-k}k}{\sinh(k)}\left[\cosh\left(\frac{2k(z-z_i)}{L}\right)J_1\left(\frac{2k(r-r_i)}{L}\right)\right]dk\right],$$

where J_1 is Bessel function of order 1. The detail of analytic calculation is written in Ref [17].

In the process of generating a crystalline beam, the precise calculation of Coulomb interactions between all particles is inevitable, that's why we employee the MD simulation code "CRYSTAL" in the study of S-LSR. In the case of S-LSR, Coulomb interaction from other bunches are very weak and take too much calculation time. Therefore we ignore the Coulomb interaction from other bunches this time. Dr. Yuri composed a MD simulation code "CRYSTAL" for the systematic study of a crystalline

beam. The detail of the simulation code “CRYSTAL” is explained in Ref. [17].

公表論文

(1) Free-energy formula for emittance-growth estimation in intense mismatched beams
K. Osaki and H. Okamoto
Progress of Theoretical and Experimental Physics, **2015**, 093G01 (2015). (12 pages)

(2) Parameter optimization for Doppler laser cooling of a low-energy heavy ion beam at the storage ring S-LSR
K. Osaki and H. Okamoto
Progress of Theoretical and Experimental Physics, **2014**, 053G01 (2014). (16 pages)

PTEP

Prog. Theor. Exp. Phys. **2015**, 093G01 (12 pages)
DOI: 10.1093/ptep/ptv128

Free-energy formula for emittance-growth estimation in intense mismatched beams

Kazuya Osaki and Hiromi Okamoto*

Graduate School of Advanced Sciences of Matter, Hiroshima University, 1-3-1 Kagamiyama, Higashi-Hiroshima 739-8530, Japan
*E-mail: okamoto@sci.hiroshima-u.ac.jp

Received May 18, 2015; Revised August 1, 2015; Accepted August 11, 2015; Published September 18, 2015

We construct a theoretical model that allows a quick estimate of emittance growth in an intense charged-particle beam initially mismatched to an external linear focusing potential. The present theory is a natural generalization of Reiser's free-energy model for coasting round beams in a uniform focusing channel. The free energy generated by a spatial mismatch, i.e. a discrepancy between the ideal beam size and an actual beam size, is calculated for an ellipsoidal bunch with an arbitrary aspect ratio. Following Reiser's prescription, we assume that the excess free energy is converted into root-mean-squared emittance growth. Multi-particle simulations are performed for comparison with theoretical predictions, which indicates that an initially mismatched bunch eventually settles into a sort of thermally anisotropic state when the mismatch is large. It is shown that the free-energy formula can explain simulation results over a wide range of parameters if the degree of the temperature anisotropy in the final state is properly incorporated into the theory.

Subject Index G10, G11

1. Introduction

There are many potential sources of instabilities that seriously deteriorate the quality of a charged-particle beam. Even if the operating point of an accelerator is properly chosen on the tune diagram to avoid intrinsic resonance lines, the beam may still be unstable due to various extra factors including magnetic error fields, coupling-impedance sources, radio-frequency (rf) noises, etc. (see, e.g., Ref. [1]). At high beam density, the natural Coulomb potential also plays an important role, leading to significant emittance growth even without these external driving forces. A typical example is the instability caused by an initial mismatch between the ideal beam configuration in phase space and the actual beam shape. It is known that a low-density particle cloud called a *beam halo* is developed around the central core if the mismatch is large (Refs. [2–9], and R. A. Jameson, Los Alamos Report LA-UR-93-1209, 1993 (unpublished)).

The self-consistent treatment of such a collective effect is extremely difficult. Since the basic equations of motion are too complex to solve mathematically, we try numerical approaches in many cases. Particle-in-cell (PIC) codes are often employed for this purpose, but high-precision PIC simulations are quite time-consuming. In particular, extremely long CPU time is required to simulate the collective behavior of an intense long bunch containing a huge number of particles. It is thus useful in practice to have any mathematical formula that enables us to make a quick estimate of emittance growth expected in a space-charge-dominated beam under a certain non-ideal condition.

Consider an intense beam traveling through a uniform focusing channel. The total energy E per particle, which includes the kinetic energy and the potential energies of the external focusing field and Coulomb self-field, is conserved in this closed system. E should be minimum when the beam is in the perfect stationary state at the beginning. Any realistic beam is, however, more or less deviated from the stationary state, which implies that the system usually possesses an excess energy. Reiser assumed that this free energy is consumed to increase the beam emittance. He developed a simple analytic theory under this assumption to evaluate the possible root-mean-squared (rms) emittance growth in a non-stationary coasting round beam [10]. We here generalize his theory to treat an intense bunched beam focused by linear external forces in all three dimensions. An ellipsoidal bunch with rotational symmetry is assumed for the sake of simplicity because the horizontal and vertical betatron tunes are often close in ordinary beam transport channels. The excess free energy is calculated in the case where a stationary bunch in the thermal equilibrium is spatially distorted in both the transverse and longitudinal directions. Such a spatial mismatch is unavoidable in practice.

The paper is organized as follows. In Sect. 2, we first outline the Hamiltonian model employed for the present study and then derive formulas to estimate emittance growth rates in a non-stationary bunch. The free energy produced by a deformation of the bunch shape is calculated in Sect. 3. We also discuss temperature anisotropy developed during the relaxation process of the initially deformed (mismatched) bunch. On the basis of the free-energy and temperature-anisotropy equations given in Sect. 3, the possible emittance growth due to an initial mismatch is evaluated in Sect. 4 and compared with self-consistent multi-particle simulations. Concluding remarks are finally given in Sect. 5.

2. Model

2.1. Basic equations for a uniformly populated bunch

As is well known, the motion of a charged particle in a dense beam traveling through a linear focusing channel obeys the Hamiltonian

$$H = \frac{p_x^2 + p_y^2 + p_z^2}{2} + V_{\rm ext} + \frac{2\pi\varepsilon_0 K_{\rm p}}{Nq} U_{\rm C}, \tag{1}$$

where $V_{\rm ext}$ is the external potential provided by beam-focusing magnets, $U_{\rm C}$ is the Coulomb self-field potential, q is the charge state of the particle, ε_0 is the vacuum permittivity, $K_{\rm p}$ is the generalized beam perveance, and the independent variable is the path length s along the design beam orbit. For a beam traveling at a speed βc with c being the speed of light, the perveance is defined by $K_{\rm p} = 2Nr_{\rm p}/\beta^2\gamma^3$ where N is the number of particles in a bunch, $r_{\rm p}$ is the classical particle radius, and γ is the Lorentz factor, i.e., $\gamma = 1/(1-\beta^2)^{1/2}$. Employing the smooth approximation, we can express $V_{\rm ext}$ as

$$V_{\rm ext} = \frac{1}{2}\left(k_x^2 x^2 + k_y^2 y^2 + k_\parallel^2 z^2\right), \tag{2}$$

where (k_x, k_y) and $k_\parallel$ determine the beam-focusing strengths on the transverse x–y plane and in the longitudinal z-direction. These focusing parameters are proportional to the phase advances or, in other words, the *tunes* at zero beam intensity. The harmonic oscillator model as in Eq. (2) has been frequently used in past theoretical studies of intense beam dynamics [11]. For an ellipsoidal bunch with rotational symmetry, we can put $k_x = k_y (\equiv k_\perp)$. At high beam intensity, the spatial particle distribution is homogenized due to the natural Debye screening effect. We thus assume that the charge density ρ is approximately uniform within the ellipsoidal boundary $\left(x^2 + y^2\right)/a^2 + z^2/b^2 = 1$.

The corresponding Coulomb potential is given by

$$U_{\mathrm{C}} = -\frac{\rho a^2 b}{4\varepsilon_0} \int_0^\infty \frac{1}{\left(a^2+\sigma\right)\left(b^2+\sigma\right)^{1/2}} \left(\frac{x^2+y^2}{a^2+\sigma} + \frac{z^2}{b^2+\sigma} \right) d\sigma. \tag{3}$$

When the bunch contains N particles, $\rho = Nq/(4\pi a^2 b/3)$. Substituting Eqs. (2) and (3) into Eq. (1), we have

$$H = \frac{p_x^2+p_y^2+p_z^2}{2} + \frac{1}{2}k_\perp^2 f_\perp(a,b)\left(x^2+y^2\right) + \frac{1}{2}k_\parallel^2 f_\parallel(a,b)\, z^2, \tag{4}$$

where

$$f_\perp(a,b) = 1 - \frac{3K_{\mathrm{p}}}{4k_\perp^2} \int_0^\infty \frac{d\sigma}{\left(a^2+\sigma\right)^2\left(b^2+\sigma\right)^{1/2}} \quad \text{and}$$
$$f_\parallel(a,b) = 1 - \frac{3K_{\mathrm{p}}}{4k_\parallel^2} \int_0^\infty \frac{d\sigma}{\left(a^2+\sigma\right)\left(b^2+\sigma\right)^{3/2}}.$$

For later convenience, we introduce several useful equations of second moments. In the transverse x-direction the canonical equations of motion are derived from Hamiltonian (4) as $dx/ds = p_x$ and $dp_x/ds = -k_\perp^2 f_\perp(a,b)x$. Provided that the particle distribution function obeys the Vlasov equation in phase space, the use of these canonical equations allows us to obtain $da_{\mathrm{rms}}/ds = \langle xp_x\rangle/a_{\mathrm{rms}}$ and $d\langle xp_x\rangle/ds = \langle p_x^2\rangle - k_\perp^2 f_\perp(a,b)a_{\mathrm{rms}}^2$, where the symbol $\langle A\rangle$ stands for averaging the quantity A over all particles and a_{rms} is the rms beam size defined by $a_{\mathrm{rms}} = \langle x^2\rangle^{1/2}$. a_{rms} satisfies the rms envelope equation

$$\frac{d^2 a_{\mathrm{rms}}}{ds^2} + k_\perp^2 f_\perp(a,b)\, a_{\mathrm{rms}} - \frac{\varepsilon_\perp^2}{a_{\mathrm{rms}}^3} = 0, \tag{5}$$

where $\varepsilon_\perp$ is the transverse rms emittance defined by $\varepsilon_\perp = \left(a_{\mathrm{rms}}^2\langle p_x^2\rangle - \langle xp_x\rangle^2\right)^{1/2}$. Similar second-moment equations hold for the other two directions. While a uniform particle density has been assumed here, the rms envelope equations are insensitive to the type of distribution function, as theoretically proven by Sacherer [12].

Ideally, an intense beam injected into an accelerator should be not only well matched to the machine lattice but also in thermal equilibrium (or, in other words, *equipartitioned* [13]). No emittance growth occurs in that case. The beam is perfectly stationary under the uniform restoring force generated by V_{ext}, so we write $a \equiv a_0(=\text{const.})$ and $b \equiv b_0(=\text{const.})$. Since $a_{\mathrm{rms}} = a/\sqrt{5}$ and $b_{\mathrm{rms}} = b/\sqrt{5}$ for a uniformly populated bunch, the rms envelope equations lead to

$$\varepsilon_\perp^{(0)} = \frac{k_\perp \eta_\perp a_0^2}{5} \quad \text{and} \quad \varepsilon_\parallel^{(0)} = \frac{k_\parallel \eta_\parallel b_0^2}{5}, \tag{6}$$

where $\varepsilon_\perp^{(0)}$ and $\varepsilon_\parallel^{(0)}$ represent the transverse and longitudinal rms emittances of the matched beam, and the so-called *tune depressions* have been introduced as $\eta_\perp = [f_\perp(a_0,b_0)]^{1/2}$ and $\eta_\parallel = \left[f_\parallel(a_0,b_0)\right]^{1/2}$. By definition, the tune depressions become unity at the low-beam-intensity limit, i.e. $K_{\mathrm{p}} \to 0$. As the beam density increases, both parameters approach zero. Assuming a

matched beam initially equipartitioned, we obtain [13]

$$\frac{\varepsilon_{\parallel}^{(0)}}{\varepsilon_{\perp}^{(0)}} = \frac{k_{\perp}\eta_{\perp}}{k_{\parallel}\eta_{\parallel}} = R_0, \tag{7}$$

where $R_0 \equiv b_0/a_0$ is the aspect ratio of the matched ellipsoid. Under this condition, the tune depression factors can be written as

$$\eta_{\perp}^2 = 1 - Q_0 I_{\perp}(R_0) \quad \text{and} \quad \eta_{\parallel}^2 = 1 - Q_0 \left(\frac{\eta_{\parallel}}{\eta_{\perp}}\right)^2 I_{\parallel}(R_0), \tag{8}$$

where $Q_0 = 3K_{\rm p}/4(k_{\perp}a_0)^2 a_0$,

$$I_{\perp}(R_0) = \int_0^{\infty} \frac{d\sigma'}{(1+\sigma')^2\left(R_0^2+\sigma'\right)^{1/2}} \quad \text{and} \quad I_{\parallel}(R_0) = R_0^2 \int_0^{\infty} \frac{d\sigma'}{(1+\sigma')\left(R_0^2+\sigma'\right)^{3/2}}.$$

Equations (8) indicate that, given $\eta_{\perp}$ and $\eta_{\parallel}$, the parameter Q_0 and the aspect ratio R_0 are uniquely determined for the equipartitioned bunch.

2.2. *Emittance growth due to excess free energy*

If a bunch is perfectly matched to the external focusing potential, the total energy of the system takes the minimum value W_0. Unfortunately, it is impossible in any realistic cases to establish such a perfect stationary state at the beginning; the beam is more or less deviated from the ideal condition because of unavoidable artificial errors. The beam then possesses a greater energy $W_i (> W_0)$ depending on the degree of the initial mismatch. The mismatched bunch cannot be stationary but starts to execute a complex collective motion. It is reasonable to expect that, after some relaxation period, the non-stationary beam will settle into a stationary state with final energy W_f [10]. The excess energy $\Delta W = W_f - W_0$ is, according to Reiser, consumed to increase the rms emittance. Since the energy conservation law requires $W_f = W_i$, the emittance growth rate is directly linked to how much free energy is produced at the beginning by a certain mismatch.

The average total energy of the system per particle is the sum of the kinetic energy $E_{\rm k}$, the beam-focusing potential $E_{\rm p}$, and the Coulomb self-field energy $E_{\rm C}$. In the case of an initially matched beam, the second-moment equations yield the simple relations $\langle p_x^2 \rangle = k_{\perp}^2 a_0^2 f_{\perp}(a_0, b_0)/5$, etc. because everything is static; namely, all s-derivatives vanish. We then readily find

$$E_{\rm k} = \frac{1}{2}\left(\left\langle p_x^2\right\rangle + \left\langle p_y^2\right\rangle + \left\langle p_z^2\right\rangle\right) = \frac{(k_{\perp}\eta_{\perp}a_0)^2}{5} + \frac{\left(k_{\parallel}\eta_{\parallel}b_0\right)^2}{10}. \tag{9}$$

On the other hand, $E_{\rm p}$ is given by

$$E_{\rm p} = \frac{(k_{\perp}a_0)^2}{5} + \frac{\left(k_{\parallel}b_0\right)^2}{10}. \tag{10}$$

Integrating the Coulomb potential over the whole bunch, we obtain the average self-field energy per particle:

$$E_{\rm C} = \frac{3K_{\rm p}}{16}\int_0^{\infty} \frac{d\sigma}{\left(a_0^2+\sigma\right)\left(b_0^2+\sigma\right)^{1/2}} - \frac{(k_{\perp}a_0)^2}{10}\left(1-\eta_{\perp}^2\right) - \frac{\left(k_{\parallel}b_0\right)^2}{20}\left(1-\eta_{\parallel}^2\right). \tag{11}$$

Hence, the minimum energy of the matched state can be calculated from

$$W_0 = \frac{(k_{\perp}a_0)^2}{10}\left(1+3\eta_{\perp}^2\right) + \frac{\left(k_{\parallel}b_0\right)^2}{20}\left(1+3\eta_{\parallel}^2\right) + \frac{3K_{\rm p}}{16}\int_0^{\infty} \frac{d\sigma}{\left(a_0^2+\sigma\right)\left(b_0^2+\sigma\right)^{1/2}}. \tag{12}$$

In the final stationary state reached from a certain mismatched beam, the semi-axes of the bunch are no longer a_0 and b_0 but changed to, say, a_f and b_f. The total energy W_f can be expressed similarly to Eq. (12) as long as the bunch density stays approximately uniform:

$$W_f = \frac{\left(k_\perp a_f\right)^2}{10}\left[1+3f_\perp\left(a_f,b_f\right)\right] + \frac{\left(k_\parallel b_f\right)^2}{20}\left[1+3f_\parallel\left(a_f,b_f\right)\right] + \frac{3K_\mathrm{p}}{16}\int_0^\infty \frac{d\sigma}{\left(a_f^2+\sigma\right)\left(b_f^2+\sigma\right)^{1/2}}. \tag{13}$$

Although an initial mismatch often develops a low-density tail around the beam core, the number of these halo particles is typically a few percent of N. We, therefore, assume a uniform density profile to be approximately valid in the final state, as Reiser did in his original work for a coasting beam [10]. By expanding W_f about the matched state and keeping only low-order terms, an approximate expression of the excess energy ΔW takes the form

$$\begin{aligned}\frac{\Delta W}{\left(k_\perp a_0\right)^2} \approx{}& \frac{1}{20}\left(11\eta_\perp^2-3\right)\left[\left(\frac{a_f}{a_0}\right)^2-1\right] + \frac{1}{40}\left(11\eta_\parallel^2-3\right)\left(\frac{\eta_\perp}{\eta_\parallel}\right)^2\left[\left(\frac{b_f}{b_0}\right)^2-1\right] \\ &+ \frac{3Q_0}{20}\left[4I_1\left(R_0\right)\left(\frac{a_f}{a_0}\right)^2 + I_2\left(R_0\right)\left(\frac{b_f}{b_0}\right)^2\right]\left[\left(\frac{a_f}{a_0}\right)^2-1\right] \\ &+ \frac{3Q_0}{40}\left[2I_2\left(R_0\right)\left(\frac{a_f}{a_0}\right)^2 + 3I_3\left(R_0\right)\left(\frac{b_f}{b_0}\right)^2\right]\left[\left(\frac{b_f}{b_0}\right)^2-1\right],\end{aligned} \tag{14}$$

where we have used Eq. (7) and introduced the following integral functions of R_0:

$$I_1\left(R_0\right) = \int_0^\infty \frac{d\sigma'}{\left(1+\sigma'\right)^3\left(R_0^2+\sigma'\right)^{1/2}}, \quad I_2\left(R_0\right) = R_0^2\int_0^\infty \frac{d\sigma'}{\left(1+\sigma'\right)^2\left(R_0^2+\sigma'\right)^{3/2}}, \text{ and}$$

$$I_3\left(R_0\right) = R_0^4\int_0^\infty \frac{d\sigma'}{\left(1+\sigma'\right)\left(R_0^2+\sigma'\right)^{5/2}}.$$

For a spherical beam where $R_0 = 1$, we have $I_1 = I_2 = I_3 = 2/5$.

After the relaxation process of an initially mismatched beam is completed, the transverse rms emittance has reached the approximate final value $\varepsilon_\perp^{(f)} \approx k_\perp a_f^2\sqrt{f_\perp\left(a_f,b_f\right)}$. The emittance growth rate can thus be estimated from

$$\begin{aligned}\frac{\varepsilon_\perp^{(f)}}{\varepsilon_\perp^{(0)}} &\approx \frac{1}{\eta_\perp}\left(\frac{a_f}{a_0}\right)^2\sqrt{f_\perp\left(a_f,b_f\right)} \\ &\approx \left(\frac{a_f}{a_0}\right)^2\sqrt{1+\frac{2Q_0I_1\left(R_0\right)}{\eta_\perp^2}\left[\left(\frac{a_f}{a_0}\right)^2-1\right]+\frac{Q_0I_2\left(R_0\right)}{2\eta_\perp^2}\left[\left(\frac{b_f}{b_0}\right)^2-1\right]}.\end{aligned} \tag{15}$$

Similarly, we have the longitudinal emittance-growth formula:

$$\begin{aligned}\frac{\varepsilon_\parallel^{(f)}}{\varepsilon_\parallel^{(0)}} &\approx \frac{1}{\eta_\parallel}\left(\frac{b_f}{b_0}\right)^2\sqrt{f_\parallel\left(a_f,b_f\right)} \\ &\approx \left(\frac{b_f}{b_0}\right)^2\sqrt{1+\frac{Q_0I_2\left(R_0\right)}{\eta_\perp^2}\left[\left(\frac{a_f}{a_0}\right)^2-1\right]+\frac{3Q_0I_3\left(R_0\right)}{2\eta_\perp^2}\left[\left(\frac{b_f}{b_0}\right)^2-1\right]}.\end{aligned} \tag{16}$$

As already mentioned, the values of Q_0 and R_0 are fixed once the tune depressions $\eta_\perp$ and $\eta_\parallel$ are chosen. Therefore, the additional pieces of information required to find the emittance growth rates are the ratios a_f/a_0 and b_f/b_0.

3. Determination of a_f/a_0 and b_f/b_0

Unlike the previous study by Reiser [10], two independent conditions are necessary to determine the emittance growth rates because we have one more dimension. The first condition can be obtained from Eq. (14) by calculating ΔW for a particular non-stationary initial state. We here focus our discussion on one of the most probable initial errors in general accelerators, i.e., a mismatch in the transverse and longitudinal beam sizes at injection. The corresponding free-energy formula can be given as a function of known parameters, which we employ to derive a relation of a_f/a_0 and b_f/b_0. Although we still need one more condition to determine these ratios, it seems difficult to deduce another useful relation from a simple physical hypothesis. In the latter part of this section, therefore, we try to introduce an empirical formula on the basis of information from self-consistent numerical simulations.

3.1. *Free-energy formula for a spatially mismatched bunch*

Let us consider a bunch that initially has semi-axes of a_i (transverse) and b_i (longitudinal). Ideally, a_i and b_i must be adjusted precisely to the matched values a_0 and b_0, but, in reality, we can only achieve an approximate matching where $a_i = \xi_\perp a_0$ and $b_i = \xi_\parallel b_0$ with positive constants $\xi_\perp$ and $\xi_\parallel$ called *mismatch factors*. The total energy W_i of a mismatched bunch can be calculated in the same way as described in the last section:

$$W_i = \frac{(k_\perp a_0)^2}{10}\left[\xi_\perp^2 + 2\left(\frac{\eta_\perp}{\xi_\perp}\right)^2 + \xi_\perp^2 f_\perp\left(\xi_\perp a_0, \xi_\parallel b_0\right)\right] + \frac{(k_\parallel b_0)^2}{20}\left[\xi_\parallel^2 + 2\left(\frac{\eta_\parallel}{\xi_\parallel}\right)^2 + \xi_\parallel^2 f_\parallel\left(\xi_\perp a_0, \xi_\parallel b_0\right)\right] + \frac{3K_\mathrm{p}}{16}\int_0^\infty \frac{d\sigma}{\left(\xi_\perp^2 a_0^2 + \sigma\right)\left(\xi_\parallel^2 b_0^2 + \sigma\right)^{1/2}}, \tag{17}$$

where we have assumed that the mismatched beam initially has the same rms emittance as the matched beam. Provided that the mismatch is not too large, the free energy can be written as

$$\begin{aligned}\frac{\Delta W}{(k_\perp a_0)^2} &= \frac{W_i - W_0}{(k_\perp a_0)^2} \\ &\approx \frac{\xi_\perp^2 - 1}{20}\left[\left(\frac{\eta_\perp}{\xi_\perp}\right)^2\left(7\xi_\perp^2 - 4\right) - 3 + 4Q_0\xi_\perp^2 I_1(R_0) + Q_0\xi_\parallel^2 I_2(R_0)\right] \\ &\quad + \frac{\xi_\parallel^2 - 1}{40}\left[\left(\frac{\eta_\perp}{\xi_\parallel}\right)^2\left(7\xi_\parallel^2 - 4\right) - 3\left(\frac{\eta_\perp}{\eta_\parallel}\right)^2 + 2Q_0\xi_\perp^2 I_2(R_0) + 3Q_0\xi_\parallel^2 I_3(R_0)\right].\end{aligned} \tag{18}$$

Given the design tune depressions $\eta_\perp$ and $\eta_\parallel$, we can readily evaluate $\Delta W/(k_\perp a_0)^2$ from Eq. (18) for a non-stationary bunch that has specific mismatch factors at injection. We then substitute the obtained value of $\Delta W/(k_\perp a_0)^2$ into the left-hand side of Eq. (14), which leads to a simple algebraic equation of a_f/a_0 and b_f/b_0.

3.2. *Temperature anisotropy after relaxation*

It may be rational to think that an initially mismatched bunch will relax into an equipartitioned state. If that is the case, the temperature ratio $T_f \equiv {k_\perp}^2 {a_f}^2 f_\perp(a_f, b_f)/{k_\parallel}^2 {b_f}^2 f_\parallel\left(a_f, b_f\right)$ should be close to unity after a final quasi-equilibrium is reached. We can then use the equation $T_f \approx 1$ as the second condition to determine a_f/a_0 and b_f/b_0. We have, however, found through numerical simulations that the final state is often quite anisotropic. Only when $R_0 \approx 1$ (a spherical bunch), the bunch stays near an equipartitioned state unless the mismatch is too large. In order to judge whether a mismatched beam has reached a quasi-equilibrium state, we paid attention to the time evolution of the transverse and longitudinal rms emittances. Figure 1 shows the typical emittance evolution calculated with the particle-in-cell code "Warp" [14]. When the mismatch is large, the rms emittances rapidly grow at the beginning in both the transverse and longitudinal directions and then come to a plateau. Since weak emittance oscillations do not completely vanish within a reasonable CPU time, we take an average over the last few tens of betatron periods to estimate the equilibrium emittance and temperature after relaxation[1]. The temperature ratio T_f in the final state is plotted in Fig. 2 at several different bunch densities and aspect ratios as a function of the transverse mismatch factor $\xi_\perp$. The longitudinal mismatch factor $\xi_\parallel$ is varied in the range $0.8 \leq \xi_\parallel \leq 1.2$. The initial distribution of macro-particles is uniform in real space and Maxwellian in velocity space[2]. The figure suggests that the temperature anisotropy in the final state is enhanced as we increase the mismatch and/or bunch density. The observed dependence of the anisotropy on free parameters needs to be incorporated properly into our model. Among a number of possible choices, we here try the following function:

$$T_f\left(\xi_\perp, \xi_\parallel; \eta_\perp, R_0\right) \approx 1 + \frac{R_0 - 1}{R_0}\left[\left(A_1 e^{-A_2 R_0} + A_3\right)\frac{\left(\xi_\perp^{\mathrm{sgn}(\xi_\perp - 1)} - 1\right)^2}{\eta_\perp} + \left(B_1 e^{-B_2 R_0} + B_3\right)\frac{\left(\xi_\parallel^{\mathrm{sgn}(\xi_\parallel - 1)} - 1\right)^2}{\eta_\perp^3}\right], \tag{19}$$

where the fitting constants are given by $A_1 = 1.67$, $A_2 = 0.27$, $A_3 = 1.46$, $B_1 = -1.49$, $B_2 = 0.43$, and $B_3 = -1.71$. As demonstrated in Fig. 2 (solid curves), this function fits the numerical results (colored dots) over a sufficiently wide range of parameters. Naturally, the temperature anisotropy in the final state is not symmetric about the matched line $\xi_\perp = 1$ because the bunch initially becomes denser with $\xi_\perp < 1$ and thinner with $\xi_\perp > 1$. From the equation $T_f = {k_\perp}^2 {a_f}^2 f_\perp\left(a_f, b_f\right)/{k_\parallel}^2 {b_f}^2 f_\parallel\left(a_f, b_f\right)$, we have

$$T_f\left(\xi_\perp, \xi_\parallel; \eta_\perp, R_0\right) \cdot \left(\frac{b_f}{b_0}\right)^2 \left\{1 + \frac{Q_0 I_2(R_0)}{\eta_\perp^2}\left[\left(\frac{a_f}{a_0}\right)^2 - 1\right] + \frac{3 Q_0 I_3(R_0)}{2\eta_\perp^2}\left[\left(\frac{b_f}{b_0}\right)^2 - 1\right]\right\}$$
$$\approx \left(\frac{a_f}{a_0}\right)^2 \left\{1 + \frac{2 Q_0 I_1(R_0)}{\eta_\perp^2}\left[\left(\frac{a_f}{a_0}\right)^2 - 1\right] + \frac{Q_0 I_2(R_0)}{2\eta_\perp^2}\left[\left(\frac{b_f}{b_0}\right)^2 - 1\right]\right\}, \tag{20}$$

[1] The number of numerical integration steps required for a good estimate of the equilibrium temperature tends to be larger for a longer bunch. We have so far followed the emittance evolution over at most a few thousand betatron oscillation periods in each Warp simulation.

[2] We have confirmed that the bunch is stationary (no emittance growth) without the mismatch, i.e., under the condition $\xi_\perp = \xi_\parallel = 1$.

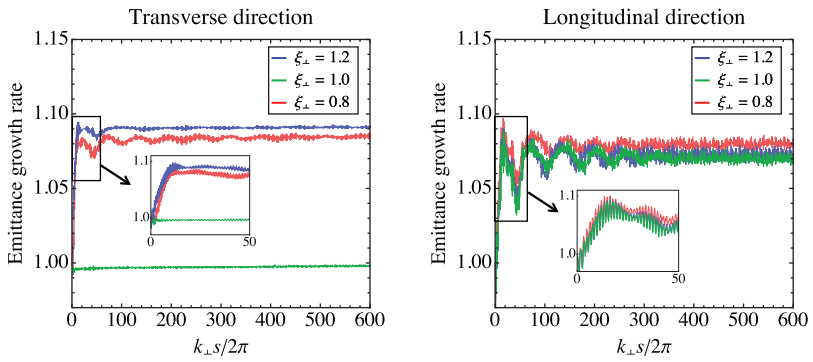

Fig. 1. Time evolution of the transverse and longitudinal rms emittances obtained from Warp simulations. Several different sizes of initial mismatches are applied to a bunch that has the aspect ratio $R_0 = 3$ and the transverse tune depression $\eta_\perp = 0.8$. The transverse mismatch is chosen as either $\xi_\perp = 0.8$, 1.0, or 1.2 while the longitudinal mismatch is fixed at $\xi_\parallel = 1.2$.

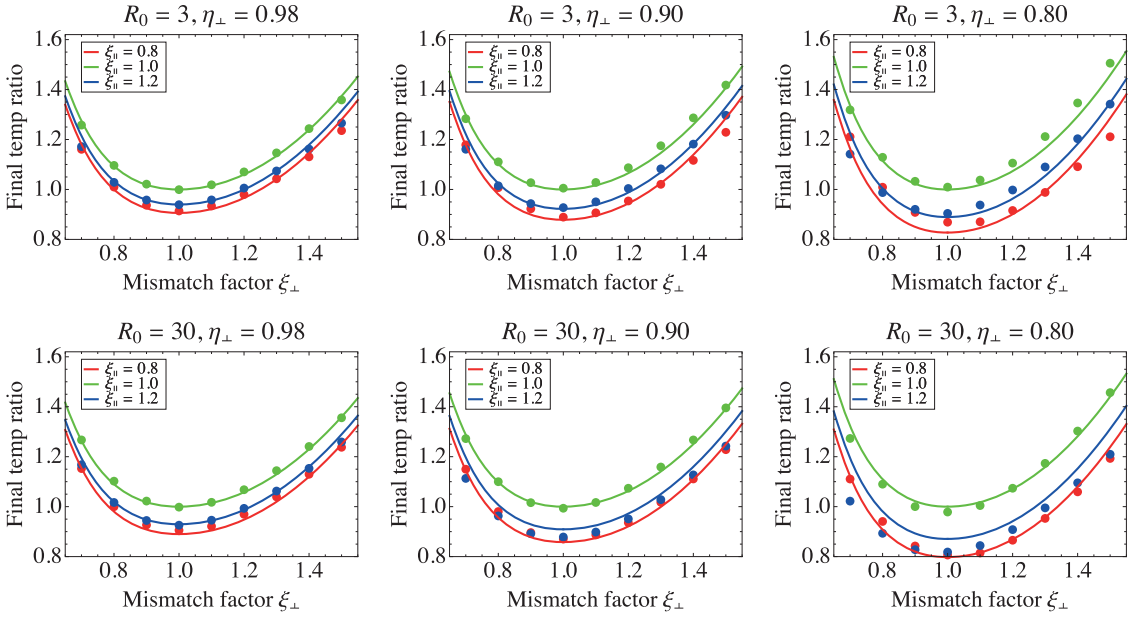

Fig. 2. Examples of Warp simulation results on the temperature anisotropy in the final quasi-equilibrium state. The transverse-to-longitudinal temperature ratio T_f is plotted as a function of $\xi_\perp$. Three different values, i.e. 0.8, 1.0, and 1.2, are chosen for the longitudinal mismatch factor $\xi_\parallel$ in each panel. The aspect ratio is fixed at $R_0 = 3$ (short bunch) in the upper three panels while, in the lower three, $R_0 = 30$ (long bunch). The transverse tune depression $\eta_\perp$ is set at 0.98 (left), 0.90 (middle), and 0.80 (right). Colored dots represent multi-particle simulation data obtained with corresponding parameters. Solid lines are the fitting result based on Eq. (19).

which gives another explicit relation of a_f/a_0 and b_f/b_0 once the initial tune depressions and mismatch factors are chosen. Together with the free-energy equation, i.e. Eq. (14) equated to Eq. (18), we now have sufficient conditions to determine a_f/a_0 and b_f/b_0, the values of which are inserted into Eqs. (15) and (16) for emittance-growth evaluation.

4. Comparison with multi-particle simulations

Systematic Warp simulations were performed to verify how accurately the present theoretical model predicts the rms emittance growth of an initially mismatched bunch. We considered the fundamental parameters listed in Table 1. As explained above, we only need two given independent parameters

Table 1. Simulation parameters.

Aspect ratio R_0	1, 2, 3, 6, 10, 30
Transverse tune depression $\eta_\perp$	0.98, 0.90, 0.80
Transverse mismatch factor $\xi_\perp$	0.7–1.5
Longitudinal mismatch factor $\xi_\parallel$	0.8–1.2

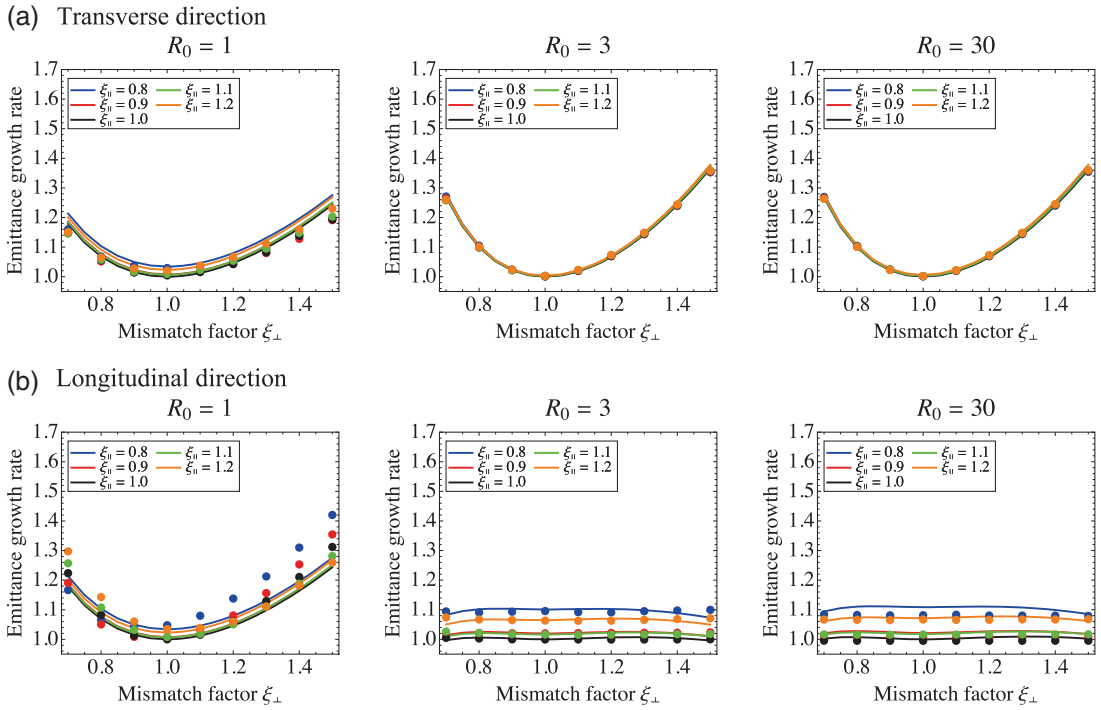

Fig. 3. Rms emittance growth at $\eta_\perp = 0.98$. The growth rates in the transverse direction (upper panels) and longitudinal direction (lower panels) are plotted as a function of transverse mismatch factor $\xi_\perp$. Colored dots represent Warp simulation results based on the fundamental parameters in Table 1. Different colors stand for different longitudinal mismatch factors: $\xi_\parallel = 0.8$ (blue), 0.9 (red), 1.0 (black), 1.1 (green), and 1.2 (orange). Solid lines are the predictions from the free-energy model. The results obtained with other aspect ratios ($R_0 = 2$, 6, and 10) are similar to those of $R_0 = 3$ and 30.

to construct an equipartitioned matched state; namely, we can uniquely define the matched state by fixing two of the four parameters ($\eta_\perp$, $\eta_\parallel$, R_0, and Q_0). In the numerical examples here, we take the aspect ratio R_0 and the transverse tune depression $\eta_\perp$ under the equipartitioning condition in Eq. (7), and then apply a spatial bunch deformation corresponding to given mismatch factors $\xi_\perp$ and $\xi_\parallel$.

Let us first look at a relatively low-density case, setting $\eta_\perp = 0.98$. The longitudinal tune depression $\eta_\parallel$ ranges from 0.98 to 0.89 corresponding to the change of the aspect ratio R_0 from 1 to 30. Figure 3(a) shows the transverse rms emittance growth rate plotted as a function of $\xi_\perp$. Five different values of $\xi_\parallel$ are considered in each panel where the aspect ratio is fixed at either 1, 3, or 30. The five colored curves are theoretical predictions based on the emittance-growth formula in Eq. (15). Following the prescription described in previous sections, we first insert the given numbers of $\eta_\perp$ and R_0 into the free-energy formula (Eq. (14) together with Eq. (18)) and the temperature anisotropy formula (Eq. (20) together with Eq. (19)). These two conditions are then solved with specific mismatch factors to find the ratios a_f/a_0 and b_f/b_0 that are substituted in Eq. (15) to predict the emittance growth rate. Colored dots in each panel represent Warp simulation results. We see that the free-energy model can

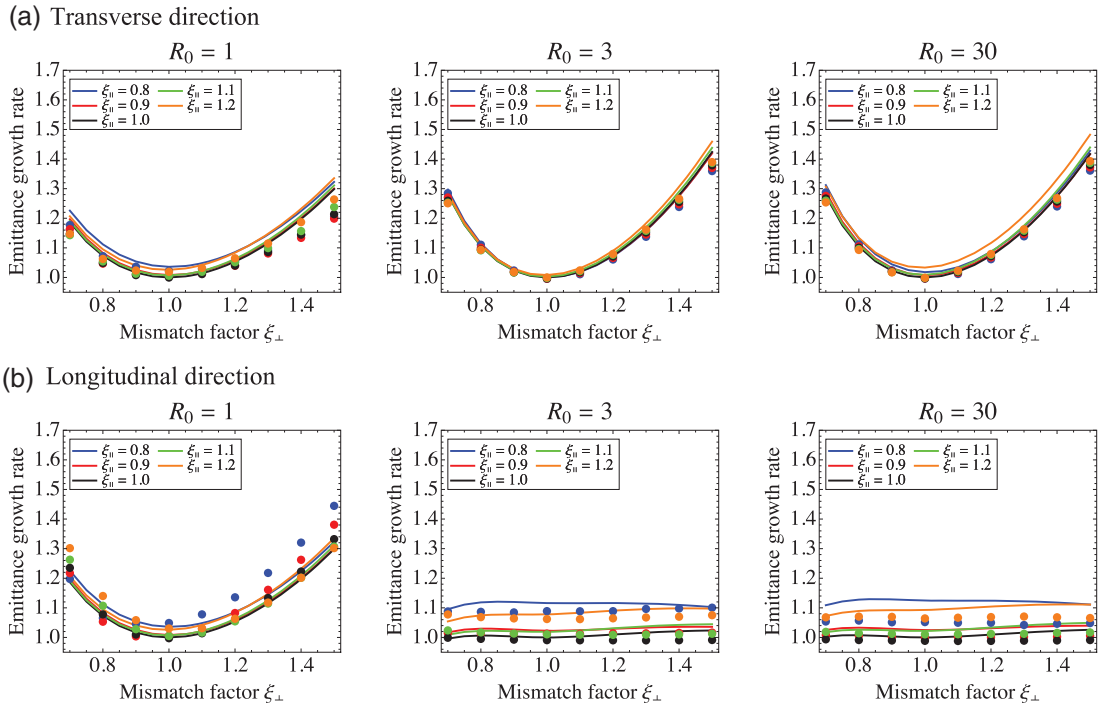

Fig. 4. Rms emittance growth at $\eta_\perp = 0.9$. Theoretical predictions from the free-energy model are compared with Warp simulation results. Fundamental parameters considered here are the same as those in Fig. 3 except for the bunch density. The longitudinal tune depression $\eta_\parallel$ ranges from 0.9 to 0.64 corresponding to the change of R_0 from 1 to 30.

explain the Warp data very well. Note that, at this tune depression, the transverse emittance growth rate is insensitive to the longitudinal mismatch factor $\xi_\parallel$. Similar results have been obtained for other aspect ratios, i.e. $R_0 = 2$, 6, and 10. Reasonable agreement between the theory and self-consistent simulations is also confirmed for the longitudinal degree of freedom, as demonstrated in Fig. 3(b). Interestingly, the longitudinal growth rate appears to be almost independent of $\xi_\perp$ and R_0, except for the spherical bunch ($R_0 = 1$).

We now increase the bunch density from $\eta_\perp = 0.98$ to higher levels where $\eta_\perp$ is set equal to 0.9 or 0.8 initially. Theoretical and simulation results in the case of $\eta_\perp = 0.9$ are summarized in Fig. 4. We again only show the data obtained with $R_0 = 1$, 3, and 30. The dependence of rms emittance growth on the mismatch factors is more or less similar to what we found in Fig. 3. In any case, the theoretical estimate from the free-energy model is in good agreement with the corresponding Warp results over the whole parameter ranges considered here. Figure 5 shows the results of $\eta_\perp = 0.8$. The transverse emittance growth is slightly enhanced compared to the lower-density cases in Figs. 3 and 4 while, in the longitudinal direction, no significant change is observed. We recognize that the accuracy of the theoretical prediction is somewhat worsened, especially in the longitudinal emittance-growth estimate. A possible reason for this is the deterioration of the fitting accuracy by Eq. (19). Another reason could be a deviation of the final bunch profile from the uniform distribution assumed in our model. In fact, a noticeable beam halo is inevitably formed around the core as we increase the bunch density and the degree of initial mismatches. Typical phase-space distributions of mismatched bunches after relaxation are shown in Fig. 6 for reference. Despite these limitations, it is evident from Figs. 3–5 that the present formulas are useful in estimating the rate of potential emittance growth.

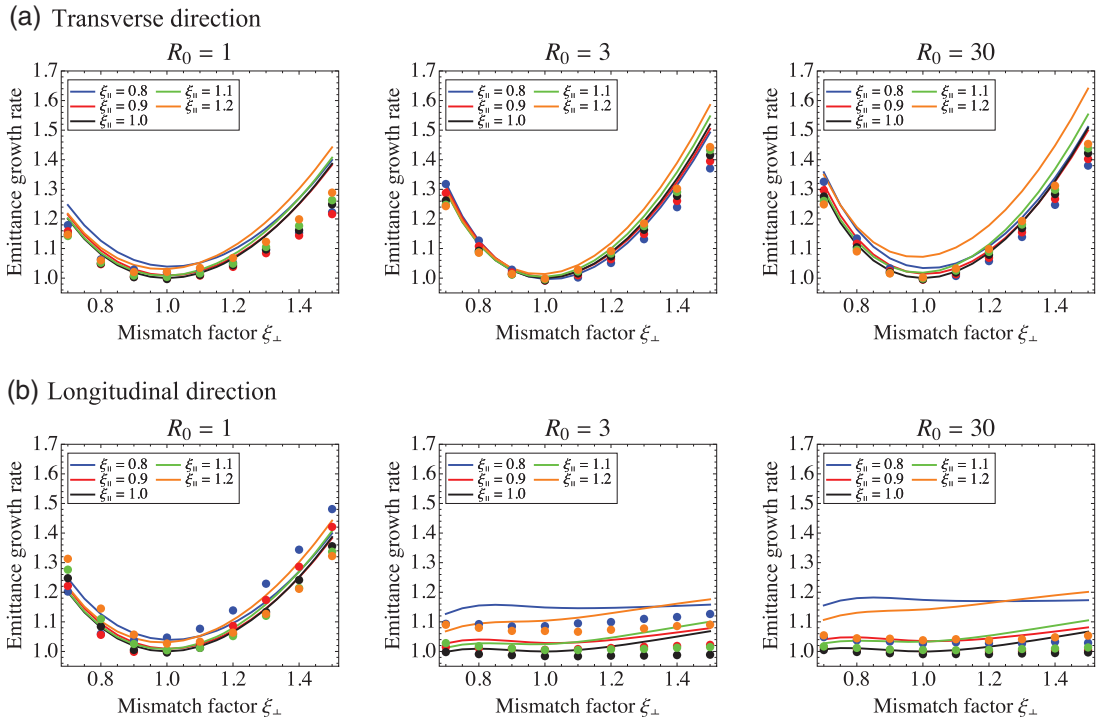

Fig. 5. Rms emittance growth at $\eta_\perp = 0.8$. Theoretical predictions from the free-energy model are compared with Warp simulation results. Fundamental parameters considered here are the same as those in Fig. 3 except for the bunch density. The longitudinal tune depression $\eta_\parallel$ ranges from 0.8 to 0.47 corresponding to the change of R_0 from 1 to 30.

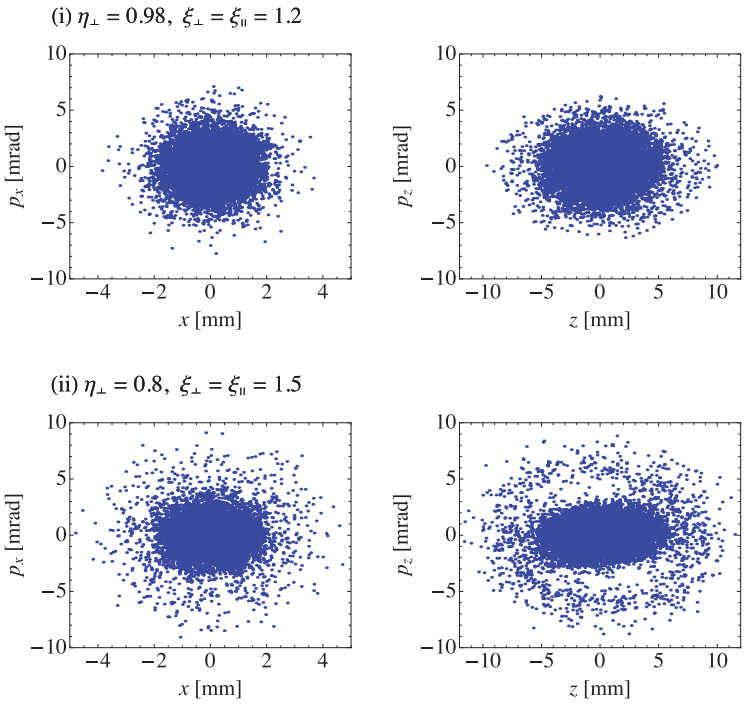

Fig. 6. Warp simulation results of initially mismatched bunches with $R_0 = 3$. Typical particle distributions after relaxation are plotted in the transverse and longitudinal phase spaces. The upper panels correspond to the case where $\eta_\perp = 0.98$ and $\xi_\perp = \xi_\parallel = 1.2$. The bunch density and initial mismatch are increased in the lower panel where $\eta_\perp = 0.8$ and $\xi_\perp = \xi_\parallel = 1.5$.

5. Summary

We have developed a simple analytic theory to estimate the rms emittance growth of an intense beam when its spatial extent disagrees with the ideal matched value at injection. Reiser's free-energy model for a coasting beam is generalized to treat an ellipsoidal bunch focused three-dimensionally by a linear external potential. Given the initial beam density, or, more correctly, two of the four free parameters ($\eta_\perp$, $\eta_\parallel$, R_0, Q_0), the stationary matched state is uniquely defined. The transverse and longitudinal emittance growth rates can then be calculated from Eqs. (15) and (16) for a certain degree of initial bunch deformation characterized by the mismatch factors $\xi_\perp$ and $\xi_\parallel$. To find the ratios a_f/a_0 and b_f/b_0 in these equations, we employ the free-energy formula in Eq. (14) and the temperature-anisotropy formula in Eq. (20). The left-hand side of Eq. (14), i.e. the excess free energy of an initially mismatched bunch, is evaluated from Eq. (18) for specific mismatch factors, which yields an explicit relation of a_f/a_0 and b_f/b_0. Similarly, Eq. (20) gives another relation of a_f/a_0 and b_f/b_0 if the temperature anisotropy T_f is known as a function of the mismatch factors. In the present study, we carried out systematic numerical simulations to clarify the parameter dependence of T_f. Equation (19) is a possible choice that fits the numerical data over a wide range of parameters at reasonable accuracy. Equation (14) with Eq. (18) and Eq. (20) with Eq. (19) make it possible to determine a_f/a_0 and b_f/b_0, which are substituted into Eqs. (15) and (16) to obtain the emittance growth rates. We compared theoretical predictions with time-consuming multi-particle simulations, confirming that the present model can explain the self-consistent numerical results fairly well. The simple algebraic equations derived in this paper thus enable us to estimate the degree of mismatch-induced emittance growth in an intense bunch easily and quickly.

References

[1] A. W. Chao and M. Tigner (eds.), *Handbook of Accelerator Physics and Engineering* (World Scientific, Singapore, 1999) and references therein.
[2] M. Reiser, in *Proceedings of the 1991 Particle Accelerator Conference*, eds. L. Lizama et al. (IEEE, San Francisco, CA, 1991), p. 2497.
[3] A. Cucchetti, M. Reiser, and T. Wangler, in *Proceedings of the 1991 Particle Accelerator Conference*, eds. L. Lizama et al. (IEEE, San Francisco, CA, 1991), p. 251.
[4] J. S. O'Connell, T. P. Wangler, R. S. Mills, and K. R. Crandall, in *Proceedings of the 1993 Particle Accelerator Conference*, ed. S. T. Corneliussen (IEEE, Washington, DC, 1993), p. 3657.
[5] R. L. Gluckstern, Phys. Rev. Lett. **73**, 1247 (1994).
[6] J. M. Lagniel, Nucl. Instrum. Meth. A **345**, 46 (1994).
[7] J. M. Lagniel, Nucl. Instrum. Meth. A **345**, 405 (1994).
[8] A. Riabko, M. Ellison, X. Kang, S. Y. Lee, D. Li, J. Y. Liu, X. Pei, and L. Wang, Phys. Rev. E **51**, 3529 (1995).
[9] H. Okamoto and M. Ikegami, Phys. Rev. E **55**, 4694 (1997).
[10] M. Reiser, J. Appl. Phys. **70**, 1919 (1991).
[11] M. Reiser, *Theory and Design of Charged Particle Beams* (Wiley, New York, 2008) and references therein.
[12] F. J. Sacherer, IEEE Trans. Nucl. Sci. **18**, 1105 (1971).
[13] R. A. Jameson, IEEE Trans. Nucl. Sci. **28**, 2408 (1981).
[14] D. P. Grote, A. Friedman, G. D. Craig, I. Haber, and W. M. Sharp, Nucl. Instrum. Meth. A **464**, 563 (2001).

PTEP

Prog. Theor. Exp. Phys. **2014**, 053G01 (16 pages)
DOI: 10.1093/ptep/ptu059

Parameter optimization for Doppler laser cooling of a low-energy heavy ion beam at the storage ring S-LSR

Kazuya Osaki[1] and Hiromi Okamoto[1,*]

[1]*Graduate School of Advanced Sciences of Matter, Hiroshima University, 1-3-1 Kagamiyama, Higashi-Hiroshima 739-8530, Japan*
*E-mail: okamoto@sci.hiroshima-u.ac.jp

Received February 05, 2014; Revised April 02, 2014; Accepted April 14, 2014; Published May 14, 2014

S-LSR is a compact ion storage ring constructed at Kyoto University several years ago. The ring is equipped with a Doppler laser cooling system aimed at beam crystallization. Bearing in mind hardware limitations in S-LSR, we try to find an optimum set of primary experimental parameters for the production of an ultracold heavy ion beam. Systematic molecular dynamics simulations are carried out for this purpose. It is concluded that the detuning and spot size of the cooling laser should be chosen around -42 MHz and 1.5 mm, respectively, for the most efficient cooling of 40 keV $^{24}Mg^{+}$ beams in S-LSR. Under the optimum conditions, the use of the *resonant coupling method* followed by *radio-frequency field ramping* enables us to reach an extremely low beam temperature on the order of 0.1 K in the transverse degrees of freedom. The longitudinal degree of freedom can be cooled to close to the Doppler limit; i.e., to the mK range. We also numerically demonstrate that it is possible to establish a stable, long one-dimensionally ordered state of ions.

Subject Index G02, G10, G16

1. Introduction

Generating an ultralow temperature beam is one of the most challenging goals in accelerator physics. The temperature of a charged-particle beam is directly linked to the concept of *emittance*, i.e., the phase-space volume occupied by the beam [1]. At absolute zero temperature, the emittance also converges to zero. This correlation allows us to say that the process of improving the beam quality (emittance) is simply *cooling*. It is, however, very difficult to compress the beam in phase space due to Liouville's theorem, which essentially says that conservative forces preserve phase-space volume. Since electromagnetic components in a regular accelerator, such as radio-frequency (rf) cavities, quadrupole focusing, and dipole bending magnets, only provide conservative forces, some dissipative interaction must be developed to reduce the beam emittance or, equivalently, the beam temperature [2].

Doppler laser cooling, the most powerful among several beam-cooling methods, is technically well established now [3,4]. Although this method is only usable for specific ion species, we can in principle reach a temperature range very close to absolute zero, where the beam would be Coulomb crystallized [5–7]. About twenty years ago, two European groups independently tried to produce an ultracold beam of low-energy heavy ions by employing the Doppler cooling technique [8,9]. While they succeeded in strongly damping the longitudinal ion oscillations, the transverse degrees of freedom turned

out to still be hot even after cooling due to some fundamental reasons [10,11]. A primary reason is that the Doppler cooling force operates only in the longitudinal direction of beam motion. Since the cooling laser has to be introduced along a straight section of a storage ring so as to ensure a sufficient overlap between the beam and the laser photons, no direct dissipative force is available in the direction perpendicular to the beam propagation. It is also theoretically pointed out that the lattice designs of the two European cooler rings, i.e. TSR and ASTRID, were not suitable for ultracold beam generation.

Ten years after the European challenge toward ultimate beam cooling, another challenging experiment began at Kyoto University where a compact ion storage ring, S-LSR, was constructed [12]. S-LSR is equipped with a Doppler cooling system for $^{24}Mg^{+}$ ions and has a highly symmetric lattice, which lightens transverse collective beam heating. The ring is also designed to allow the application of the *resonant coupling method* (RCM), which dramatically enhances the transverse laser-cooling efficiency [13,14]. On the other hand, a few practical issues exist in the S-LSR cooling system. First, only a single laser is available for cooling. As the S-LSR lattice has six-fold symmetry, a $^{24}Mg^{+}$ beam is exposed to the dissipative force only over, at most, one sixth of the ring circumference every turn. Secondly, the laser power is limited to about 10 mW. Since any ion beams are initially hot and thus transversely expanded in size, the laser spot should be as large as possible, with the result that the photon density is lowered, which worsens the cooling efficiency. The purpose of this paper is to determine the optimum condition of laser cooling at S-LSR in consideration of these practical constraints. In Sect. 2, we outline the cooling system and also briefly describe the recent experimental result obtained with the RCM. Section 3 is devoted to a summary of systematic molecular dynamics (MD) simulations that lead us to the optimum set of cooling parameters. An rf ramping scheme is studied in Sect. 4 to mitigate the heating from intrabeam scattering (IBS). The scheme is very simple but effective in reducing the equilibrium beam temperature. MD results show that a long "string" configuration of ultracold ions could be formed in S-LSR if the beam line density is initially set low. Concluding remarks are given in Sect 5.

2. Transverse cooling scheme at S-LSR

The RCM was proposed two decades ago to extend a one-dimensional (1D) dissipative effect to the other two degrees of freedom [13,14]. The idea is quite simple; we first introduce an artificial linear coupling potential to correlate two independent degrees of freedom, and then just move the operating point of the ring onto a proper difference resonance. In the case of laser cooling, only the longitudinal beam motion is directly affected, as explained above. We therefore provide a linear potential that couples the longitudinal motion with the horizontal. In the present S-LSR experiment, an ordinary rf cavity is adopted as the coupling source. As is well known, a linear synchro-betatron coupling between these two degrees of freedom can be developed if the cavity is placed at any position with finite momentum dispersion [14]. A compact, double-gap drift tube cavity was designed for this purpose and set in one of the six straight sections [15]. In order to further extend the cooling force to the vertical direction, another coupling source is necessary. The solenoid magnet originally installed for electron cooling experiments can be utilized in S-LSR [16]. A solenoidal field linearly couples the two transverse degrees of freedom, which enables us to transfer the longitudinal laser-induced dissipation to the vertical direction via the horizontal direction. The indirect transverse cooling effect is most enhanced through the coupling potentials when the lattice fulfills the following resonance conditions:

$$\nu_x - \nu_z = \text{integer}, \quad \nu_x - \nu_y = \text{integer}, \tag{1}$$

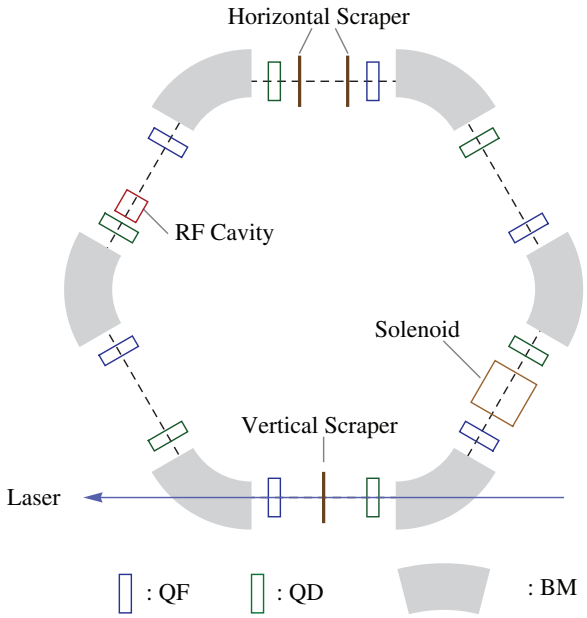

Fig. 1. The lattice layout of S-LSR. QF, QD, and BM stand, respectively, for quadrupole focusing, quadrupole defocusing, and dipole bending magnets. There are several beam scrapers installed to remove the tail of a stored beam.

where (ν_x, ν_y) are the horizontal and vertical betatron tunes, and ν_z is the longitudinal synchrotron tune. The condition (1) requires ν_z to be non-zero to avoid a transverse integer-resonance instability. The beam is thus inevitably bunched in the operating mode of multi-dimensional cooling by the RCM. The resultant synchrotron motion of $^{24}Mg^+$ ions in the longitudinal phase space makes it possible to cool the beam without sweeping the laser frequency [17]. We usually set ν_z at around 0.07 to put the S-LSR operating point sufficiently away from the transverse resonance. A low beam energy (typically 40 keV) and a high rf harmonic number (typically 100) are taken for the laser cooling mode, so that we can easily increase ν_z with a small rf amplitude (below a few tens of volts for the required synchro-betatron resonance).

A schematic drawing of the S-LSR lattice is given in Fig. 1. The ring consists of six superperiods, each of which includes a single doublet cell. The circumference is 22.557 m. The rf cavity for longitudinal–horizontal coupling and the solenoid magnet for horizontal–vertical coupling sit in different straight sections. The cooling laser is introduced in the direction co-propagating with the $^{24}Mg^+$ beam. The frequency of the cooling transition of $^{24}Mg^+$ ions from the ground state $3s^2S_{1/2}$ to the excited level $3p^2P_{3/2}$ is about 1 PHz, corresponding to a wavelength of 280 nm. The Doppler limit is about 1 mK. So far, the laser frequency is fixed at a certain value slightly below the natural transition frequency. The distance from the transition frequency is referred to as *laser detuning*, one of the important parameters which should be optimized carefully.

The effectiveness of the RCM for indirect transverse laser cooling was recently demonstrated at S-LSR [15,18]. In the first attempt [15], the simpler two-dimensional (2D) cooling scheme was studied by switching off the solenoid magnet. The bare betatron tunes were fixed at $(\nu_x, \nu_y) = (2.068, 1.105)$. Fluorescence signals from laser-cooled Mg ions indicated a strong reduction of the horizontal beam size when the synchrotron tune ν_z was close to the resonant value 0.068. The horizontal beam temperature after cooling was estimated to be 200 K, roughly 30 times lower than the initial value ($\sim$6000 K). Because the reachable temperature as well as the cooling time was most likely limited by

IBS, in the second attempt the beam tail was initially scraped to reduce the intensity [18]. As a result, the horizontal temperature was further decreased to 20 K. Despite the fact that the solenoid coupling was still off, the vertical degree of freedom was also cooled to 29 K through Coulomb collisions [19]. The sympathetic cooling is generally not very effective at such a low intensity, but we assume that the artificially enhanced horizontal cooling strongly compressed the beam and the resultant increase of the beam density made the collision rate higher. Although the final beam temperature experimentally achieved at S-LSR is already far below the temperature of any regular beams, it is still too high to establish a crystalline order of ions.

3. Molecular dynamics simulations

The MD simulation code CRYSTAL [20] is employed to identify the best set of primary cooling parameters for ultralow-temperature beam generation at S-LSR. It is possible in CRYSTAL simulations to take the actual lattice structure of the storage ring into account. The dissipative force induced by laser photons is evaluated from the well-known formula

$$\mathbf{F} = \frac{1}{2}\hbar\mathbf{k}\Gamma\frac{S}{1+S+(2\Delta/\Gamma)^2}, \tag{2}$$

where $\hbar\mathbf{k}$ is the momentum vector of a laser photon, Γ is a natural line width of the cooling transition, S is the saturation parameter, and Δ is the detuning of the laser frequency. We assume a round Gaussian laser with a saturation parameter of the form $S = S_0\exp[-2(x^2+y^2)/\sigma^2]$, where S_0 stands for the peak value on the beam line, (x, y) are the transverse spatial coordinates, and σ is the laser spot size, which varies along the cooling section. In this paper, the size of the laser waist, in other words the minimum value of σ at the center of the cooling section, is simply called "spot size" unless noted otherwise.

In most recent cooling experiments at S-LSR, the initial beam intensity is taken as low as possible to minimize IBS. The total number of $^{24}Mg^+$ ions is reduced to the order of 10^4 by the scrapers right after every beam injection into the ring. Since the rf frequency of the cavity is always set at 2.51 MHz corresponding to the harmonic number of 100 for a beam of 40 keV $^{24}Mg^+$ ions, a single bunch contains roughly 100 ions. We thus start each MD simulation with 300 particles per bunch that have Gaussian distributions with respect to all six canonical coordinates. The initial momentum spread ($\sim 7 \times 10^{-4}$) and initial transverse root-mean-squared (rms) emittance ($\sim 1 \times 10^{-9}$ m, normalized) are determined in consideration of past measurement data. These numbers correspond to the beam temperature of over a few 100 K, five orders of magnitudes higher than the Doppler limit ($\sim$1 mK).

We optimize the coupling strengths among the degrees of freedom, the laser spot size, and the detuning. We also pay attention to the *particle capture rate* (PCR), defined as the number of laser-cooled ions divided by the total number of stored ions (3×10^4) in the ring. For reference, examples of typical beam profiles before and after multi-dimensional laser cooling is shown in Fig. 2. Owing to the limited laser power at S-LSR as well as strong IBS, a considerable number of ions remain uncooled after a few seconds of cooling. It is possible to remove these hot ions with the scrapers if necessary because they have relatively large transverse oscillation amplitudes. In the following, therefore, we calculate the beam temperature only from the cold laser-cooled portion, disregarding the hot tail particles.

In order to separate laser-cooled ions from the other hot ions in MD simulations, we set a tiny closed boundary in each of the horizontal, vertical, and longitudinal phase planes. The area (i.e., emittance) inside each boundary is typically chosen a few times larger than the expected final emittance of

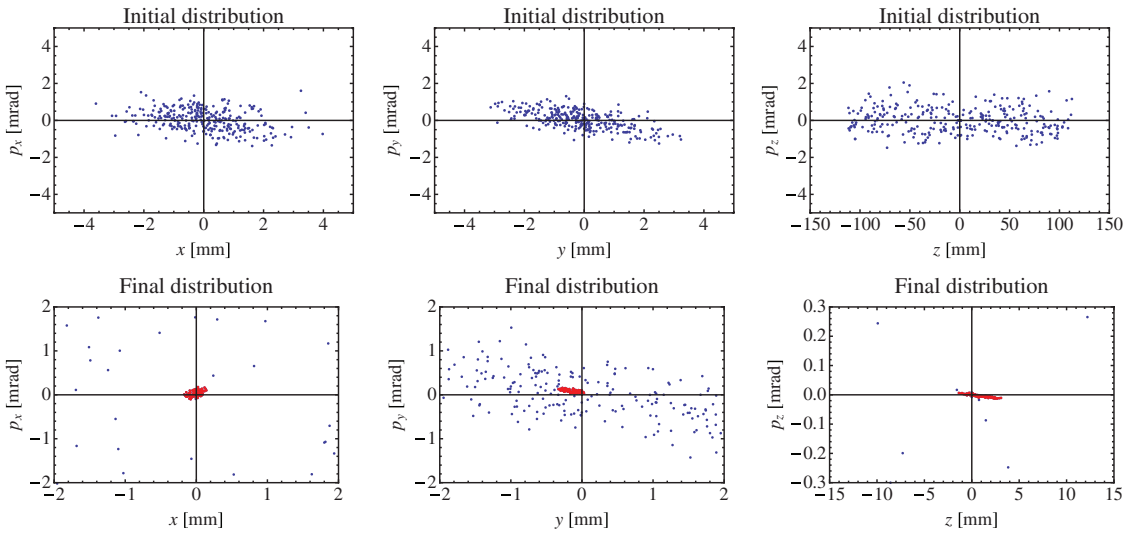

Fig. 2. Typical phase-space distributions of $^{24}Mg^{+}$ ions before and after laser cooling at S-LSR. p_x and p_y represent the transverse kinetic momenta scaled by the design axial momentum, while p_z corresponds to the momentum spread of the beam. The initial distributions in the upper panels are changed to the lower ones within a few seconds after multi-dimensional laser cooling. Note that in the lower panels, only the vicinity of the central beam orbit is shown; there are many uncooled ions out of the ranges of the coordinates. We can easily separate the laser-cooled ions that are concentrated near the origin (see text).

the laser-cooled portion. An ion is defined as "laser-cooled" if it is inside the boundaries in all three phase planes simultaneously. We have confirmed that this definition works well because the ultracold portion of the beam is generally stable with the cooling laser on and has very small emittances in all directions (see Fig. 2).

3.1. Two-dimensional cooling

The experiments reported in Refs. [15] and [18] are based on the 2D cooling scheme where the solenoid magnet is off. The vertical direction is independent of the other two directions unless imperfection fields and/or inter-particle Coulomb interactions play a noticeable role. Table 1 summarizes typical S-LSR parameters in the 2D cooling mode. The artificial coupling strength between the longitudinal and horizontal degrees of freedom is determined by the magnitude of momentum dispersion at the rf cavity. According to the linear theory [13,14], there is a threshold value of dispersion above which the horizontal cooling efficiency is roughly maintained at the same high level as the longitudinal direct cooling efficiency. A simple theoretical estimate using transfer matrices suggests that the threshold dispersion is only about 0.1 m under the lattice conditions in Table 1. The actual dispersion is 1.016 m, well above the theoretically demanded minimum value.

Expanding Eq. (2) about the design beam velocity, we find that the coefficient of the linear frictional term is maximized at the detuning $|\Delta| = (\Gamma/2)\sqrt{(1+S)/3}$. In the case of S-LSR where laser photons are co-propagating with the beam, Δ must be negative. Assuming $S \approx 1$ on axis, we have $\Delta \approx -\Gamma/2$, which gives -21 MHz for $^{24}Mg^{+}$ ions. While this value of detuning guarantees the highest cooling efficiency for particles near the axis, PCR could probably be improved with a larger detuning. PCR also depends on the laser spot size in practice. We therefore focus our discussion here on four particular choices of detuning; namely, -21 MHz, -42 MHz, -63 MHz, and -84 MHz, which are integer multiples of $-\Gamma/2$. Note that in the recent cooling experiment at S-LSR [18], the

Table 1. S-LSR parameters in the 2D cooling mode.

Ion species	$^{24}Mg^{+}$
Kinetic beam energy	40 keV
Betatron tunes (ν_x, ν_y)	(2.075, 1.120)
Synchrotron tune ν_z	0.075
Rf harmonic number	100
Rf voltage	41.8 V
Phase slip factor	–0.6758
Dispersion at the rf cavity	1.016 m
Solenoid field	OFF
Total laser power	10 mW

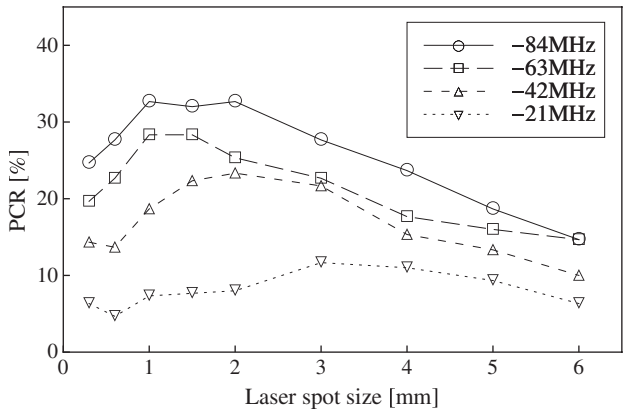

Fig. 3. Particle capture rate (PCR) after 5 s of 2D laser cooling at S-LSR vs. laser spot size σ at the center of the cooling straight section. We have considered four different values of laser detuning, i.e. -21 MHz, -42 MHz, -63 MHz, and -84 MHz, which correspond, respectively, to $-\Gamma/2$, $-\Gamma$, $-3\Gamma/2$, and -2Γ. The lattice parameters assumed here are listed in Table 1.

detuning had been set, typically, at -200 MHz to improve the PCR. The cooling laser was focused to $\sigma < 0.5$ mm, much smaller than the initial beam extent. For comparison, we did MD simulations assuming these actual parameters and obtained the possible final temperature of around 10 K in the transverse directions and around 0.3 K in the longitudinal direction. These numbers are in reasonable agreement with the experimental observation in Ref. [18].

PCR evaluated at 5 s after the start of each cooling procedure is plotted in Fig. 3 as a function of the laser spot size. As expected, the ion capture efficiency becomes better with a larger detuning. This MD result recommends choosing the spot size σ in the range, say, 1.5–2 mm, which is somewhat smaller than the initial beam extent (see Fig. 2). Ideally, the spot size should be sufficiently greater than the transverse extent of an initial hot beam to cover all ions for cooling. Provided that the transverse beam extent is initially about 3 mm in radius, as in the example of Fig. 2, the laser spot has to cover an area of 9π mm^2 within which the photon density should preferably be over the saturation level. We then need a total laser power well beyond 70 mW to cool all hot ions efficiently because the saturation intensity for $^{24}Mg^{+}$ is 2.54 mW mm^{-2}. The total laser power available in S-LSR is, however, only 10 mW, which means that too much expansion of the laser spot results in a considerable reduction of the photon density and thus seriously affects the cooling rate. This is why we have an optimum range of σ for the best cooling performance. Thanks to the betatron oscillations, even

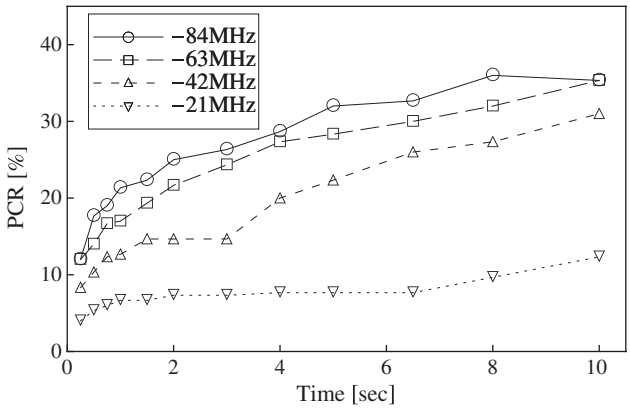

Fig. 4. Time evolution of PCR in the 2D cooling mode. The laser spot size σ is fixed at 1.5 mm in all simulations here.

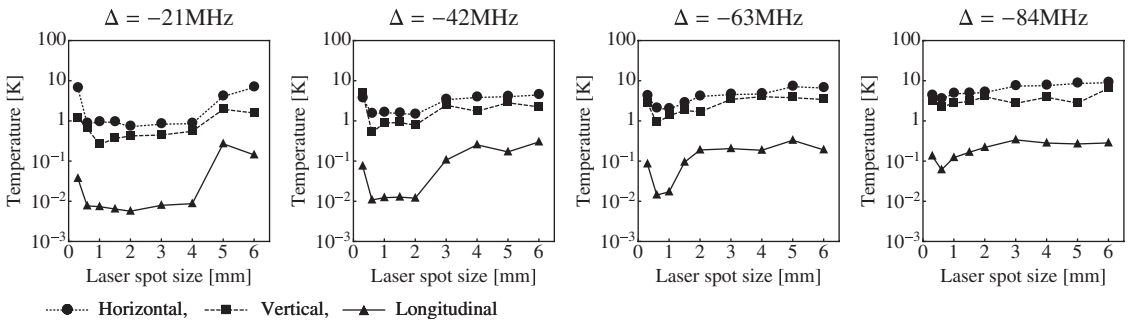

Fig. 5. Beam temperature reached in 5 s after injection by the use of the 2D resonant coupling scheme. These values of temperature are evaluated from laser-cooled ions concentrating near the design beam orbit. We have ignored the existence of many hot uncooled ions as observed in Fig. 2. If we extend the cooling period from 5 s, the gradual increase of cold ions pointed out in Fig. 4 gives rise to slight temperature growth, especially in the transverse directions, but the growth rate is low.

tail ions experience finite energy dissipation in the longitudinal direction every few turns. The resonant coupling mechanism then creates a weak but finite cooling effect on the horizontal ion motion, leading to a gradual shrinkage of the beam size and consequently to a better overlap with the laser. The improved overlap between the beam and laser enhances PCR. Figure 4 shows how PCR grows in time when we keep applying the cooling laser to the beam. The laser spot is fixed at 1.5 mm in these simulations. We observe that PCR has not come to a plateau even after 10 s of cooling, and is especially low with $\Delta = -21$ MHz.

The most important question is how much we can compress the beam in phase space. Figure 5 shows the temperature of an ion bunch after 5 s of laser cooling. To save computing time, we often limit the cooing period to 5 s, corresponding to 1.25×10^5 turns around the ring. Five seconds is generally long enough to make a good estimate of the possible lowest beam temperature (even though PCR is still rising slowly).[1] Figure 5 points out that the vertical degree of freedom can be cooled sympathetically via IBS, which is consistent with the experimental observation in Ref. [18]. It is evident from this picture that the reachable minimum temperature tends to grow as the detuning becomes larger. We also recognize that there is a narrow range of the spot size with which the beam

[1] Theoretically, the application of the RCM makes the necessary cooling time much shorter than 5 s.

Table 2. S-LSR parameters in the 3D cooling mode.

Ion species	$^{24}Mg^{+}$
Kinetic beam energy	40 keV
Betatron tunes (ν_x, ν_y)	(2.070, 1.070)
Synchrotron tune ν_z	0.070
Rf harmonic number	100
Rf voltage	36.2 V
Phase slip factor	–0.6762
Dispersion at the rf cavity	1.025 m
Solenoid field	65.0 Gauss
Total laser power	10 mW

becomes particularly cold. The sharp drop of the equilibrium beam temperature in Fig. 5 is a signature of the so-called *longitudinal beam ordering*.[2] Once this happens, the synchrotron oscillations of individual ions are almost frozen out while the transverse betatron oscillations are still active. The acceptable range for ordering becomes wider for a smaller $|\Delta|$. Contrarily, as already found in Fig. 3, PCR is worsened as $|\Delta|$ decreases. Considering these facts, we conclude that from a practical point of view, $|\Delta|$ should be set around Γ or slightly higher in the 2D cooling mode at S-LSR. The detuning of -42 MHz and the spot size of around 1.5 mm appear to be the best combination to attain a reasonably high PCR as well as an ultralow beam temperature. A final temperature near 1 K or less is then achievable in both transverse dimensions. The longitudinal temperature can be reduced to about 0.01 K, slightly above the Doppler limit. These temperatures are one order of magnitude lower than the recent experimental result at S-LSR [18].

3.2. Three-dimensional cooling

We now switch on the solenoid magnet to provide a linear coupling between the horizontal and vertical directions. To maximize the indirect laser-cooling rate in the vertical degree of freedom, we need both resonance conditions in Eq. (1) to be simultaneously satisfied. The lattice parameters assumed for three-dimensional (3D) cooling simulations are listed in Table 2. The fractional parts of the three tunes have been equalized to excite full 3D coupling resonances. The momentum dispersion at the rf cavity, indispensable for transverse cooling, is 1.025 m. Corresponding to this number, there is the optimum narrow range of the solenoid field strength for most efficient 3D cooling. Transfer-matrix theory [14] was again employed to obtain the cooling-rate diagram in Fig. 6. We see that the vertical cooling rate increases at the expense of the cooling rates of the other two directions as the solenoid field is strengthened. The cooling efficiency of the three directions can be made approximately equal when the field strength is about 65 Gauss. The dependence of PCR on the laser spot size is depicted in Fig. 7. We confirm the spot-size dependence similar to that in the 2D cooling case; PCR is maximized with the spot size around 1.5 mm. Compared to the result in Fig. 3, PCR has become slightly

[2] The longitudinal ordering here is essentially different from the ordering phenomenon experimentally observed in electron-cooled coasting ion beams at extremely low intensity [16]. In the latter ordering effect independently reported from several institutes, the inter-particle distance is typically on the order of cm, which means that the Coulomb coupling among individual particles is very weak. Each ion oscillates back and forth in the longitudinal direction, unlike the present case where the synchrotron motion is almost completely suppressed due to the balance between the axial beam confinement force and inter-particle Coulomb repulsion. For detailed information of the 1D ordering effect at ultralow line density, see Refs [21–24].

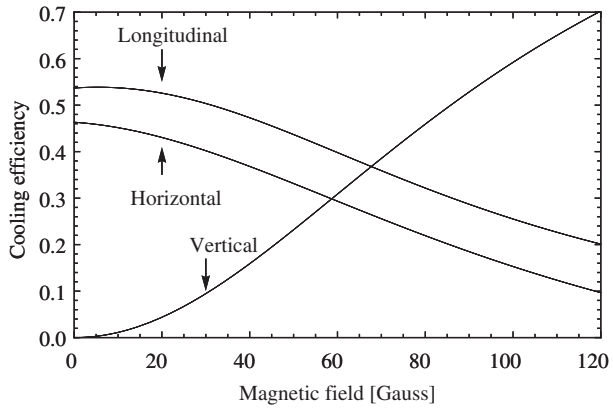

Fig. 6. Cooling rates of the three directions estimated from transfer-matrix calculations. The lattice parameters in Table 2 have been assumed, except for the solenoid field. The maximum longitudinal cooling rate without coupling, i.e. the longitudinal direct cooling efficiency by the laser, is normalized to unity. The sum of the three cooling rates at a certain solenoid field is equal to unity.

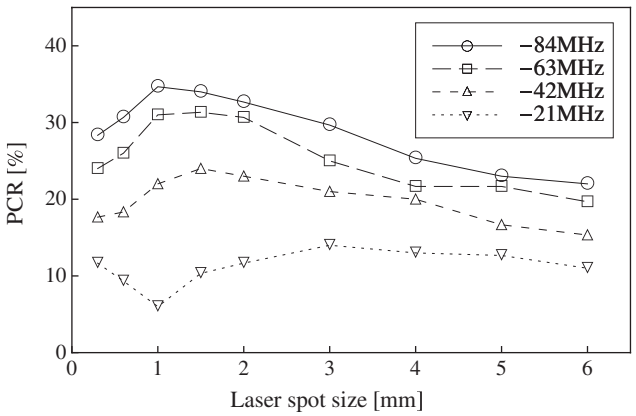

Fig. 7. PCR after 5 s of 3D laser cooling at S-LSR vs. laser spot size σ at the center of the cooling straight section. Similarly to the 2D cooling simulations in Fig. 3, we have taken four different values of laser detuning into consideration. The lattice parameters assumed here are listed in Table 2.

better in the 3D cooling operation. A preferable effect from the indirect vertical cooling is also visible in Fig. 8, which shows the beam temperature reached 5 s after the start of laser cooling. The spot-size range where we can expect the occurrence of the longitudinal beam ordering has clearly been widened. The results in Fig. 8 together with those in Fig. 7 suggest that the detuning should be chosen between $-3\Gamma/2$ and $-\Gamma$. A larger value of $|\Delta|$ guarantees more efficient capture of ions but makes the tolerable range of the laser spot size narrower. We thus come to the same conclusion as made for the 2D cooling mode; namely, σ and $|\Delta|$ should be set to $\sim$1.5 mm and $\sim$42 MHz (or somewhat higher) to generate the coldest beam in S-LSR. The possible transverse and longitudinal temperatures we can reach with these parameters are roughly 1 K and 0.01 K, respectively.

4. Radio-frequency field ramping

MD results in the last section have revealed that with proper choices of experimental parameters, we can produce in S-LSR an extremely high-quality beam that is much colder than any existing beams. It is even possible to reach a sort of spatially ordered state, strongly suppressing the longitudinal synchrotron motions of individual particles. In this section, we make one more step forward to a

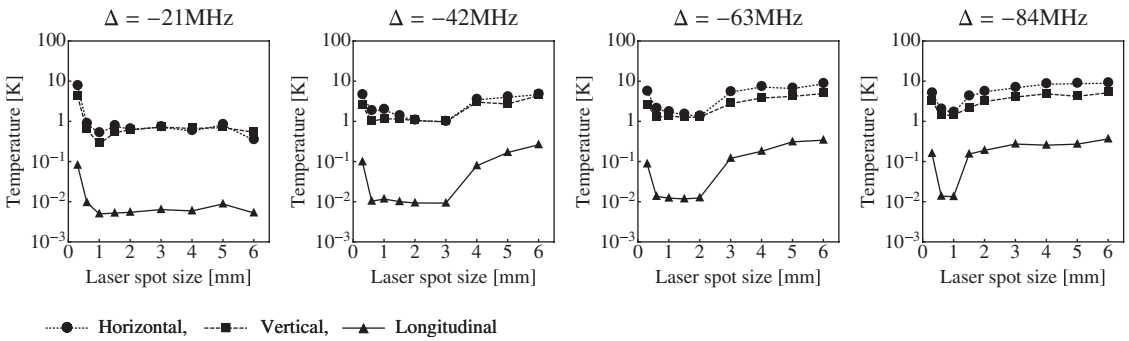

Fig. 8. Beam temperature reached in 5 s after injection by the use of the 3D resonant coupling scheme. Similarly to the result in Fig. 5, only laser-cooled ions are picked out to evaluate the temperature.

Coulomb crystalline state. According to a previous MD study assuming two counter-propagating powerful lasers [20], a string-crystal-like structure could be formed in the S-LSR lattice by means of the RCM if the number of ions per bunch is limited to less than 10. Here we considerably increase the ion number and yet show that a long string beam could be attained even with a single low-power laser.

In order to generate a crystalline beam with finite transverse spatial extent, the longitudinal cooling force has to be properly *tapered* to compensate for the shear force induced by bending magnets [10, 25]. It is also crucial to maintain strict lattice symmetry to prevent transverse coherent instability [11]. Since these requirements are very difficult to meet in practice, the only realistic target we can aim at in S-LSR is the formation of a 1D string crystal. There is the critical line density at which the structural transition from a certain crystalline configuration to another takes place [6]. Needless to say, the threshold line density of the string-to-zigzag transition is the lowest. We thus have to keep the beam line density below a certain level so that the corresponding crystalline configuration, if formed, is a string. The Hasse–Schiffer theory for *coasting* crystalline beams predicts that the string-to-zigzag transition occurs at a line density of the order of 10^4 m^{-1} under the lattice conditions in Table 2 [6]. The transition density in the present case must be much lower than this theoretical estimate because the beam is not coasting but bunched by a rather strong rf field. In fact, the bunched string shown in Ref. [20] converts into a zigzag-like configuration if we add only a few more particles. Even if we keep the ion number in a bunch below 10, it is possible to transform the string configuration into a zigzag just by raising the synchrotron tune (or, in other words, by more strongly compressing the beam in the axial direction). In Appendix A, a numerical estimation is made of the number of stored ions with which the formation of an ideal bunched crystalline state is expected in S-LSR.

The simplest way to establish a long string formation with many ions is weakening the rf field in the cavity. The synchrotron tune then decreases (with the harmonic number fixed), which gives rise to the breakdown of the coupling resonance condition and to the lack of the indirect transverse cooling force. We could, however, rely on the sympathetic effect from Coulomb interactions once the beam is cooled down to an ultralow temperature range. As verified in Fig. 5, the sympathetic cooling mechanism can be effective even at low line density if the beam is already cold. We therefore first employ the RCM to strongly cool a low-current beam in S-LSR and, after that, gradually reduce the amplitude of the rf bunching field with the cooling laser on. This process achieves the required bunch lengthening and the maintenance of a three-dimensionally cold state simultaneously. In the following MD simulations, we start from the cold beam that has already been laser-cooled for 5 s in S-LSR under the lattice conditions in Table 2. The initial ion distribution is more or less like the

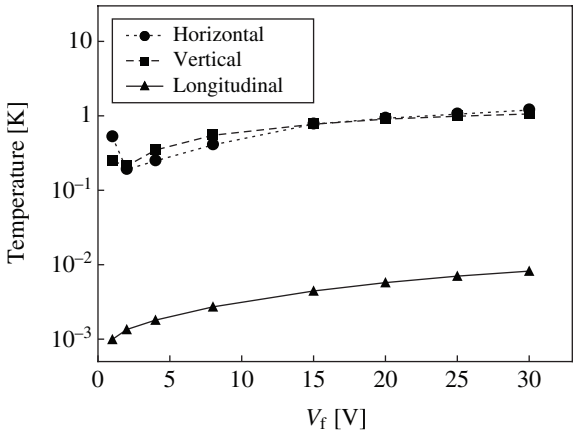

Fig. 9. Final beam temperature after the rf ramping procedure. The detuning and spot size of the cooling laser are fixed, respectively, at −42 MHz and 1.5 mm. The total number of laser-cooled particles in the ring is around 7.5×10^3 in each simulation.

one shown in the lower three panels of Fig. 2. Recalling the conclusion in the last section, we set the laser detuning and spot size, respectively, at −42 MHz and 1.5 mm. Since the PCR after 5 s cooling is 24% with these parameters (see Fig. 7), there are 72 cold ions and 228 hot ions in a bunch at the beginning. The number of the initial cold ions can readily be controlled by changing the original beam intensity at injection.

The amplitude of the rf voltage, whose initial value is 36.2 V for the synchrotron tune of 0.07, is linearly ramped to a specific final value V_f within the 12500 turns that corresponds to 0.5 s. We then maintain the rf voltage at V_f for the next 0.5 s, keeping the cooling laser on. In the rf ramping process, the hot tail ions oscillating about the design orbit may affect the motions of the cold laser-cooled ions, especially when V_f is low. Such an unfavorable source of heating can be removed effectively with the scrapers installed in S-LSR (see Fig. 1). Those scrapers have actually been used to reduce the beam intensity at injection and also to measure the transverse beam profiles.[3] We here move both horizontal and vertical scrapers toward the central beam orbit in the first 12500 turns. At the beginning, the scrapers' edges are located 5 mm away from the beam line, which eventually comes to 0.5 mm in 0.5 s.

The final beam temperature after the rf ramping procedure is plotted in Fig. 9 as a function of V_f. Each bunch contains 72 cold ions initially (but a few hot ions are eventually cooled before being scraped and join the ultracold beam core). As expected, the beam temperature can be reduced further by carefully expanding the bunch. The final temperatures reachable with the rf ramping are near 0.1 K in the transverse directions and 0.001 K in the longitudinal direction. These numbers correspond to the normalized rms emttances around the order of 10^{-12} m and below 10^{-13} m, respectively. After a sort of equilibrium state is reached within 1 s, we ramp the laser power toward zero in 0.2 s, and then wait for another 0.4 s (10000 turns) to check if the beam is stable without the cooling force. Two examples are given in Fig. 10, which shows the spatial configurations of ultracold beams 0.4 s after the cooling laser is switched off. In the upper example, there are 37 ions forming the string configuration while in the lower example, the ion number is increased to 78. In both cases, V_f is set

[3] H. Souda, private communication.

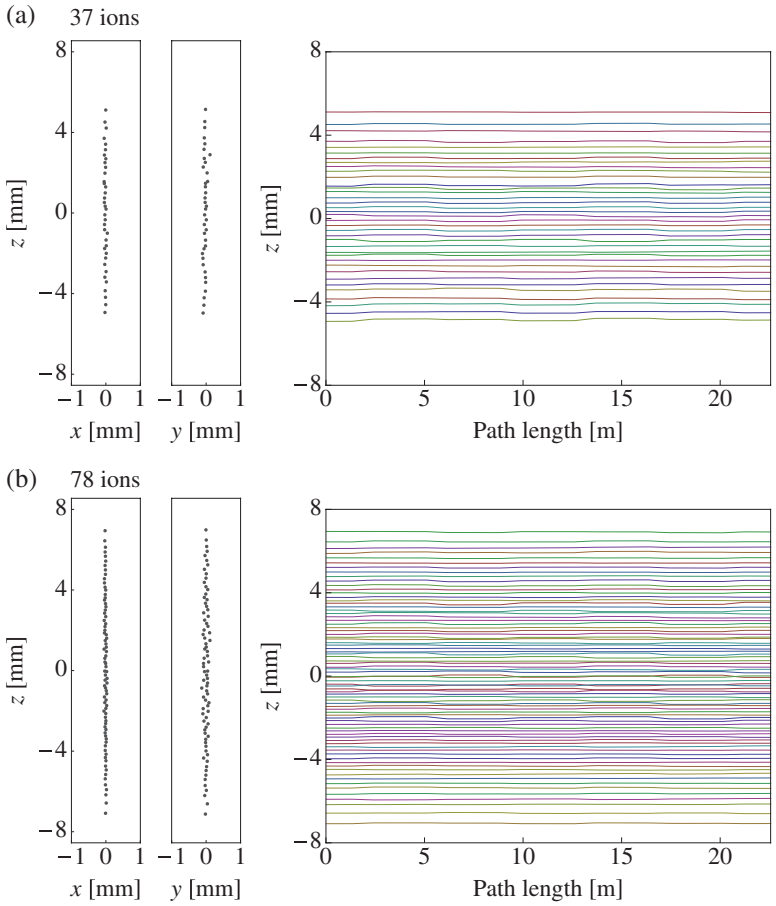

Fig. 10. Spatial configurations of laser-cooled beams after the rf ramping and the subsequent laser-power ramping procedures are completed. The two panels on the left side show the top and side views of an ultracold beam consisting of (a) 37 ions or (b) 78 ions, after 10000 turns around S-LSR without the laser cooling force. The axial position of each individual ion within the last turn is plotted on the right panel as a function of the path length along the design orbit. The final voltage V_f after the rf ramping is 2 V in both examples. We see that the synchrotron motion is almost completely suppressed in both cases.

at 2 V. We confirm that the string order of ions is well maintained for many turns around the ring even without the cooling force.

5. Concluding remarks

We have performed systematic MD simulations assuming the actual hardware conditions for Doppler laser cooling of a 40 keV $^{24}Mg^{+}$ ion beam in S-LSR. Each simulation typically starts with 300 ions per bunch. This corresponds to 3×10^4 stored ions in the ring, which is of the same order as the total ion number in recent cooling experiments [18]. The numerical data have been used to figure out the optimum cooling parameters with which the ultralow-temperature state of ions can be reached in this particular storage ring. In the past experiments done at S-LSR [15,18], the laser detuning had been chosen mostly near -200 MHz to ensure a high PCR. The present MD study has pointed out that such parameter choices are inappropriate for utilizing the full potential of the current Doppler cooling system. The simulation results in Sect. 3 indicate that the detuning and spot size of the cooling laser should be chosen, respectively, around -42 MHz and 1.5 mm. Then, the use of the RCM makes it possible for us to reach beam-temperature ranges of about 1 K in both transverse

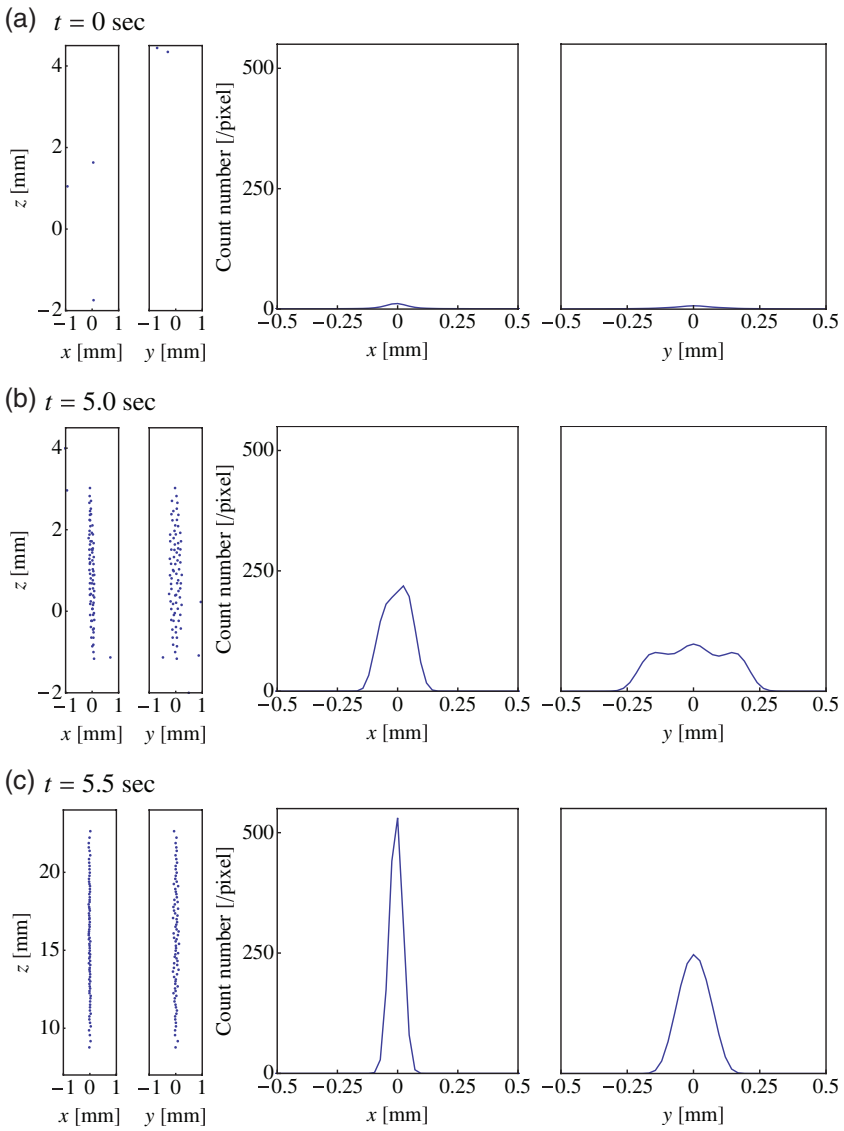

Fig. 11. Expected transverse fluorescence images of a linearly ordered, ultracold ion beam. The CRYSTAL code is used for this estimation, assuming the actual optical system and specifications of the CCD camera installed in S-LSR. As an example, we have considered the case of Fig. 10(b) where the string beam is formed with 78 ions. The upper, middle, and lower panels show the expected images (a) at the beam injection into the ring, (b) after the laser cooling for 5 s, and (c) after the completion of the rf ramping procedure. The exposure time of the camera is set at 0.1 s. Note that the centroid of the laser-cooled beam is axially shifted from the longitudinal origin (the center of the rf bucket) due to the radiation pressure by the co-propagation laser light. By gradually reducing the laser power to zero, the centroid position finally comes to the bucket center, as shown in Fig. 10.

dimensions and of the order of 0.01 K in the longitudinal dimension (see Fig. 8). These numbers are one order of magnitude lower than the recent experimental achievement reported in Ref. [18]. We have also demonstrated that a linearly ordered state of ultracold ions, the so-called string state, can be established at low line density by gradually ramping the longitudinal rf field after 3D laser cooling. It is possible to form a long, bunched string beam consisting of nearly 80 ions if the rf voltage is lowered to around 2 V (corresponding to the synchrotron tune of 0.016 for a 40 keV $^{24}Mg^{+}$ ion). During the rf ramping, both transverse and longitudinal equilibrium temperatures are even more reduced to near

0.1 K and the Doppler limit, respectively (Fig. 9). The string state is stable and lasts for more than 10000 turns with no serious heating.

Finally, it is interesting to ask whether we can conclude the formation of the string state in S-LSR from actual experimental data. According to Eq. (2), each $^{24}Mg^{+}$ ion traveling in the cooling straight section at a kinetic energy of 40 keV scatters a photon every few centimeters along the beam line provided $S \approx 1$ and $|\Delta| \approx \Gamma$. At the center of the cooling section, there is a small window located 14 cm away from the beam line [15]. Fluorescence photons passing through the window are eventually focused onto a CCD image sensor whose diameter is 2.54 cm. Considering that a hundred bunches are stored in S-LSR at the revolution frequency of 25 kHz, the sensor will receive over 10^5 photons per second from the ordered beam in Fig. 10. Since these photons come only from the vicinity of the design beam line, we expect a clear fluorescence image of the beam to be caught by the camera. Figure 11 shows an example of possible transverse beam images estimated from MD simulation data. The exposure time of the CCD camera has been assumed to be 0.1 s. Right after the beam injection ($t = 0$ s), the fluorescence signal looks so weak that it will probably be hidden behind background noise. In fact, no clear signals have been detected in past cooling experiments when the initial number of stored ions is below the order of 10^4.[4] After 3D laser cooling ($t = 5$ s) under the optimum conditions, the beam signal is enhanced by an order of magnitude. The signal becomes even sharper in both transverse directions after the rf ramping is completed. The peak level of the signal is much higher than the possible noise level in S-LSR.[4] This numerical result suggests the following: after the initial beam scraping to $\sim 3 \times 10^4$ stored ions, we lose the fluorescence signal or only have a very faint beam image. The signal will, however, be recovered during the most efficient 3D laser cooling. We will observe a sharp fluorescence peak suddenly rising on the beam line if the predicted, linearly ordered configuration is successfully formed.

Acknowledgements

The authors would like to express their sincere thanks to Drs. A. Noda, H. Souda, and M. Nakao for valuable information on the cooling experiment at the storage ring S-LSR. They are also indebted to Drs. Z. He, Y. Yuri, and A. M. Sessler for useful discussion on the present MD study.

Appendix A. Ion number threshold of bunched beam crystallization in S-LSR

We employ a linear friction model to figure out the threshold ion number below which ideal crystalline beams are obtained in S-LSR. Instead of the realistic laser cooling force, the simplest linear dissipative forces are applied to stored ions in all three degrees of freedom until the beam comes to an equilibrium state. The betatron tunes are fixed at the same values as given in Table 2 while the solenoid magnet is switched off here (because we need no coupling potentials for multi-dimensional cooling). The Coulomb coupling constant, i.e. the ratio of the average Coulomb potential energy to the average kinetic energy of stored ions [1], is calculated after cooling and color-coded in Fig. A1. In an ideal crystalline state, the coupling constant is supposed to exceed about 170. We find a clear boundary below which stable crystalline beams can be attained. The crystalline structures finally established in the parameter range with red dots are the linear string, except for a very narrow range near the boundary where the zigzag state is sometimes reached. It is possible to slightly expand the region of zigzag formation by strengthening the linear friction, but these zigzag crystals are mostly unstable. No stable shell structures can be formed even with the perfect 3D cooling force, as expected.

[4] H. Souda, private communication.

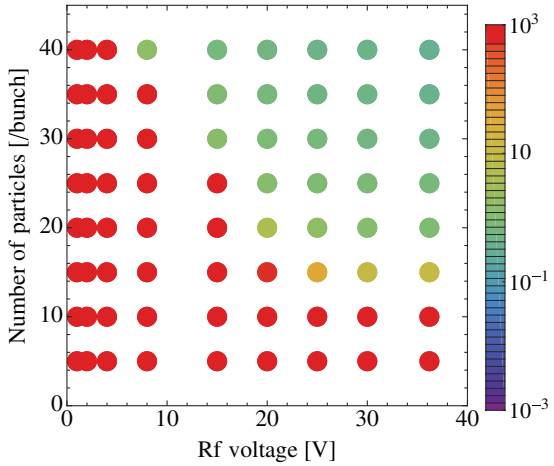

Fig. A1. Coulomb coupling constant of bunched $^{24}Mg^{+}$ beams cooled with the 3D linear frictional force. The abscissa represents the amplitude of the longitudinal rf field provided by the double-gap drift tube cavity. The betatron tunes are fixed at $(\nu_x, \nu_y) = (2.070, 1.070)$ in each MD simulation.

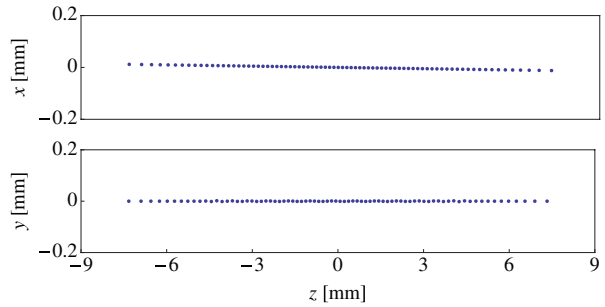

Fig. A2. Example of an ideal string crystalline configuration consisting of 78 ions. The lattice condition assumed here is identical to that in Fig. 10 (except for the cooling force applied to the beam).

Naturally, the threshold ion number per bunch is lowered as the amplitude of the rf voltage increases. This MD result suggests that, in order to generate a long string-like beam in S-LSR, the rf voltage should be well below 10 V. The spatial profile of a perfect string crystalline beam consisting of 78 ions (the same as in the case of Fig. 10) is shown in Fig. A2 for reference.

References

[1] H. Okamoto, H. Sugimoto, and Y. Yuri, J. Plasma Fusion Res. Ser. **8**, 950 (2009).
[2] A. W. Chao and M. Tigner (eds.), *Handbook of Accelerator Physics and Engineering* (World Scientific, Singapore, 1999).
[3] D. J. Wineland and H. Dehmelt, Bull. Am. Phys. Soc. **20**, 637 (1975).
[4] T. Hänsch and A. Shawlow, Opt. Commun. **13**, 68 (1975).
[5] A. Rahman and J. P. Schiffer, Phys. Rev. Lett. **57**, 1133 (1986).
[6] R. W. Hasse and J. P. Schiffer, Ann. Phys. (NY), **203**, 419 (1990).
[7] J. Wei, X.-P. Li, and A. M. Sessler, Phys. Rev. Lett. **73**, 3089 (1994).
[8] S. Schröder et al., Phys. Rev. Lett. **64**, 2901 (1990).
[9] J. S. Hangst et al., Phys. Rev. Lett. **67**, 1238 (1991).
[10] J. Wei, H. Okamoto, and A. M. Sessler, Phys. Rev. Lett. **80**, 2606 (1998).
[11] Y. Yuri and H. Okamoto, Phys. Rev. ST Accel. Beams **8**, 114201 (2005).
[12] A. Noda, Nucl. Instrum. Methods Phys. Res. Sect. A **532**, 150 (2004).
[13] H. Okamoto, A. M. Sessler, and D. Möhl, Phys. Rev. Lett. **72**, 3977 (1994).

[14] H. Okamoto, Phys. Rev. E **50**, 4982 (1994).
[15] M. Nakao et al., Phys. Rev. ST Accel. Beams **15**, 110102 (2012).
[16] T. Shirai et al., Phys. Rev. Lett. **98**, 204801 (2007).
[17] J. S. Hangst et al., Phys. Rev. Lett. **74**, 4432 (1995).
[18] H. Souda et al., Jpn. J. Appl. Phys. **52**, 030202 (2013).
[19] H.-J. Miesner et al., Phys. Rev. Lett. **77**, 623 (1996).
[20] Y. Yuri and H. Okamoto, Phys. Rev. Lett. **93**, 204801 (2004).
[21] M. Steck et al., Phys. Rev. Lett. **77**, 3803 (1996).
[22] H. Danared et al., Phys. Rev. Lett. **88**, 174801 (2002).
[23] R. W. Hasse, Phys. Rev. Lett. **83**, 3430 (1999).
[24] H. Okamoto et al., Phys. Rev. E **69**, 066504 (2004).
[25] H. Okamoto and J. Wei, Phys. Rev. E **58**, 3817 (1998).

参考論文

(1) Efficiency Enhancement of Indirect Transverse Laser Cooling with Synchro-Betatron Resonant Coupling by Suppression of Beam Intensity
Hikaru Souda, Masao Nakao, Hiromu Tongu, Kouichi Jimbo, Kazuya Osaki, Hiromi Okamoto,Yousuke Yuri, He Zhengqi, Manfread Grieser and Akira
Japanese Journal of Applied Physics. 52, 030202, (2013). (4 pages)

(2) Beam dynamics studies with non-neutral plasma traps
H. Okamoto, K. Fukushima, H. Higaki, D. Ishikawa, K. Ito, T. Iwai, K. Moriya, T. Okano, K. Osaki, and M. Yamaguchi
Proceedings of 5th International Particle Accelerator Conference, pp. 4052 – 4056 (2014).

(3) Ultralow emittance beam production based on Doppler laser cooling and coupling resonance
A. Noda, M. Nakao, H. Okamoto, K. Osaki, Y. Yuri, H. Souda, H. Tonguu, K. Jimbo, M. Grieser, Z. He, and A. Smirnov
Proceedings of 5th International Particle Accelerator Conference, pp. 28 – 33 (2014).

(4) Parameter optimization for multi-dimensional laser cooling of an ion beam in the storage ring S-LSR
Z. He, J. Wei, K. Osaki, H. Okamoto, A. Noda, M. Nakao, H. Souda, Y. Yuri, and K. Jimbo
Proceedings of Particle Accelerator Conference, pp. 1298 – 1300 (2013).

(5) Latest results of experimental approach to ultra-cold beam at S-LSR
A. Noda, M. Nakao, H. Souda, H. Tongu, H. Okamoto, K. Osaki, Y. Yuri, K. Jimbo, and M. Grieser
Proceedings of International Workshop on Beam Cooling and Related Topics, (COOL 13), pp. 157 – 161 (2013).

(6) Simulation study on transverse laser cooling and crystallization of heavy-ion beams at the cooler storage ring S-LSR
Y. Yuri, K. Osaki, H. Okamoto, Z. He, H. Souda, A. Noda, M. Nakao, H. Tongu, and K. Jimbo
Proceedings of International Workshop on Beam Cooling and Related Topics (COOL 13), pp. 162 – 165 (2013).

(7) Approach to the low temperature state oriented for crystalline beam
A. Noda, M. Nakao, H. Souda, H. Tongu, K. Jimbo, H. Okamoto, K. Osaki, Y. Yuri, I. N. Meshkov, A. V. Smirnov, M. Grieser, K. Noda, T. Shirai, and Z. He
Proceedings of XXIII Russian Particle Accelerator Conference, (RuPAC2012), pp. 48 – 52 (2012).

(8) Challenge for more efficient transverse laser cooling for beam crystallization
A. Noda, M. Nakao, H. Souda, H. Tongu, K. Ito, H. Okamoto, K. Osaki, Y. Yuri, K. Jimbo, M. Grieser, and Z. He

Proceedings of 3rd International Particle Accelerator Conference, pp. 394 – 396 (2012).
(9) Controlled beam scraping oriented for efficient indirect transverse laser cooling
A. Noda, M. Nakao, H. Souda, H. Tongu, K. Jimbo, H. Okamoto, K. Osaki, Y. Yuri, M. Grieser, and Z. He
Proceedings of 9th Meeting of Particle Accelerator Society of Japan, pp. 72 – 74 (2012).
(10) Measurement of transverse laser cooling effect using scrapers
H. Souda, M. Nakao, H. Tongu, A. Noda, K. Jimbo, K. Osaki, H. Okamoto, Y. Yuri, M. Grieser, and Z. He
Proceedings of 9th Meeting of Particle Accelerator Society of Japan, pp. 388 – 390 (2012).
(11) Present status of ion accumulation and cooler ring S-LSR
A. Noda, H. Souda, H. Tongu, M. Nakao, Y. Nasu, K. Jimbo, H. Okamoto, K. Osaki, K. Noda, S. Shibuya, T. Fujimoto, S. Iwata, M. Grieser, and H. Zhengqi
Proceedings of 8th Meeting of Particle Accelerator Society of Japan, pp. 261 – 263 (2011).